國立臺灣大學理學院海洋研究所

博士論文

Institute of Oceanography

College of Science

National Taiwan University

Doctoral Dissertation

東亞氣膠金屬對海洋的貢獻：來源、轉變以及沉降通量
The Contribution of East Asian Aerosol Metals in the Ocean: Sources, Transformation Processes and Deposition Fluxes

謝志強
Chih-Chiang Hsieh

指導教授：何東垣 教授
Advisor: Tung-Yuan Ho, Ph.D.

中華民國 112 年 7 月
July, 2023

doi:10.6342/NTU202302200

國立臺灣大學博士學位論文
口試委員會審定書

東亞氣膠金屬對海洋的貢獻：來源、轉變以及沉降通量
The contribution of East Asian aerosol metals in the ocean: sources, transformation processes and deposition fluxes

本論文係謝志強君（D06241002）在國立臺灣大學海洋研究所完成之博士學位論文，於民國 112 年 7 月 18 日承下列考試委員審查通過及口試及格，特此證明

口試委員：

何東垣（簽名）

（指導教授）

白書禎　　游鎮峰

陳怡均　　謝玉德

系主任、所長　謝志豪（簽名）

（是否須簽章依各院系所規定）

ii

doi:10.6342/NTU202302200

Acknowledgements

I am deeply grateful to my advisor, Tung-Yuan Ho, for his invaluable guidance and support throughout my Ph.D. program and the Prof. Su-Cheng Pai, Chen-Feng You, Yu-Te Alan Hsieh, and Yi-Chun Chen for serving on my thesis committee and providing helpful feedback and suggestions.

I would also like to thank my wife Tina, my son Kainoa, and other family members (A-Hai, A-O, Will, Dennis, and Chris) for their love and support during this process. Without their encouragement, this journey would not have been possible. When I was under pressure during my Ph.D. life, it can help me release pressure while watching my son’s soccer game or playing badminton with friends. Thanks to all the kids, coaches, parents from the Fatih Football Club, and badminton friends from RCEC or other institutes.

Although most of my work was done by myself, during the cruises, I had a lot of fun playing board games with lab members (Vivian, David, Jenny, Riza, Emily, Ian, Stepth, and Hsin-Ting….) or playing basketball after work or during the break time.

Finally, I would like to thank all of the participants in my study for their time and willingness to help collect samples (Prof. Hung-Yu Chen, Hajime Obata, Wen-Hsuan Liao) or share their experiences. This work would not have been completed without their contribution.

doi:10.6342/NTU202302200

Abstract

Aerosol dissolvable metals are considered to be readily bioaccessible so that their input would influence the growth and composition of marine phytoplankton and thus material cycling globally. However, it is highly challenging to measure or estimate reliable deposition fluxes of aerosol dissolvable metals in the ocean due to the impacts of complicated processes involved in pre- and post-deposition of aerosols. In this study, we applied the elemental and isotopic composition of size-fractionated aerosol metals collected in the East China Sea (ECS) and the suspended particulate matter (SPM) in the surface water of the subarctic North Pacific Ocean (SNPO) to quantify the contribution of East Asian anthropogenic and lithogenic aerosols in the oceans and also to understand their transformation processes during the transport processes.

To investigate the impacts of the aeolian transport processes on the solubilities and fluxes of aerosol metals in the ocean, we first collected lithogenic dust from major Chinese deserts and size-fractionated aerosols from the ECS to determine the variations of their dissolvable metals by using three operationally defined leaching protocols (pure water, buffer, and Berger leaches). Referred by the solubility differences between the desert dusts and the ECS largest size aerosols, atmospheric transport processes tremendously enhance all of the three solubilities for most elements in the ECS aerosols. Overall, the metal fluxes of each aerosol treatment increased with increasing particle sizes, indicating coarse aerosol is the primary metal supplier into the surface ocean. Due to the high metal enrichment factor, Cd, Zn, and Pb elements in coarse aerosols could come from anthropogenic aerosol aggregation. In addition, we found highly divergent variations for lithogenic type elements with all aerosol sizes among the three leaching treatments. Without knowing aerosol size-fractionated information, the deposition fluxes of lithogenic type elements would be significantly overestimated. The mass distribution or impacts of the transport processes could be region specific so that similar field studies are essential in other regions to obtain reliable aerosol dissolvable metal data for global modeling.

Specifically, we have applied Fe isotopic composition to investigate the contribution of East Asian aerosol Fe to the surface water of the adjacent oceanic regions and the SNPO. We observed that the isotopic value of lithogenic and anthropogenic aerosols ranged from 0.2 to

doi:10.6342/NTU202302200

-4.5 ‰. Assuming the value of anthropogenic aerosol Fe to be -4.5 ‰, the contribution of anthropogenic aerosols were 30% and 8.7% of the fluxes of dissolved Fe and buffer Fe in the ECS, respectively; the contribution to the SPM collected in the SNPO and WPS were both less than 10%. In brief, lithogenic aerosol is still the major sources of aeolian Fe for dissolvable aerosol Fe in the ECS, the WPS, and the SNPO.

Keywords: trace metal, size-fractionated aerosol, solubility, deposition flux, Fe isotopes

doi:10.6342/NTU202302200

摘要

生物可利用的溶解氣膠金屬沉降會影響海洋浮游生物的生長與組成，以及海洋中物質的循環。由於氣膠沉降前後經過了複雜的過程，因此要精準估算溶解氣膠金屬的通量是極具挑戰的！本研究我們於東海採集了5種不同粒徑的氣膠和亞北極太平洋採集了表水的懸浮顆粒，並利用元素間比值和鐵同位素來量化天然性和人為性氣膠對於西北太平洋的貢獻，與了解大氣傳播過程對氣膠的影響。

為了調查大氣傳輸對氣膠溶解度和通量的影響，我們沿用了國際常用的氣膠溶出方法來比較氣膠和中國沙漠的沙子中可溶出金屬的差異，其中包含了超純水(Ultrapure water)、醋酸銨緩衝溶液(acetate buffer)和柏格(Berger)等溶出方法。結果顯示東海氣膠的金屬經過大氣傳輸後其溶解度都有顯著的提升。整體而言，氣膠金屬的沉降通量隨著粒徑越大而越高，意旨氣膠中的粗顆粒是氣膠金屬對於海洋的主要貢獻者。從鎘、鋅和鉛的高富集因子得知，就算是粗粒徑的氣膠某些金屬(鎘、鋅、鉛)的主要來源還是有可能來自人為氣膠。此外，我們還發現岩石性元素(如:鋁、鐵和鈦)於不同溶出方法所得到的濃度或溶解度都有較大的差異，因此，若沒有事先研究金屬濃度於不同粒徑氣膠上的分布來得到較精準的平均氣膠沉降速率，岩石性的金屬通量會導致嚴重高估的現象。至於金屬濃度隨粒徑的分布或大氣傳輸的影響可能有地區性的差異，為了更精準估算全球氣膠金屬的通量，在其他大洋區域的類似研究是有必要至少調查一次的！

我們還特別使用鐵同位素組成來精準調查氣膠溶解鐵來源對鄰近海洋及亞北極太平洋表水層水的貢獻，其結果觀察到岩石性氣膠和人為性氣膠的鐵同位素值分別為0.2和-4.5‰。假設人為性氣膠鐵同位素的端點為-4.5‰，那麼其對東海的超純水及醋酸銨緩衝溶液溶出的鐵通量的貢獻分別為30%和8.7%，至於亞北極太平洋收集到的懸浮顆粒的貢獻也是低於10%。簡言而之，雖然東亞陸地傳輸大量高溶解的人為氣膠鐵至西北太平洋，但岩石性氣膠仍然是東海、西北太平洋和亞北極太平洋溶解性氣膠鐵的主要來源。

關鍵詞：微量金屬、氣膠粒徑分級、溶解度、沉降通量及鐵同位素

Table of Contents

doi:10.6342/NTU202302200

List of Figures

doi:10.6342/NTU202302200

List of Tables

doi:10.6342/NTU202302200

Chapter 1

Introduction

By
Chih-Chiang Hsieh[a,b]

[a] Institute of Oceanography, National Taiwan University, Taipei, Taiwan
[b] Research Center for Environmental Changes, Academia Sinica, Taipei, Taiwan

1.1 Introduction

The supply of biologically essential trace metals (e.g., Fe, Co, Cu, Zn, Ni) in the euphotic zone affects the growth and composition of different phytoplankton groups (Chen et al., 2022; Ho et al., 2003; Paytan et al., 2009) and thus influences material cycling in the ocean (Mackey et al., 2015; Martin and Fitzwater, 1988; Morel et al., 2020). Atmospheric deposition is a major process supplying external trace metals to the euphotic zone of the ocean (Jickells et al., 2016). Dissolvable aerosol metals are generally considered to be bioavailable to marine phytoplankton (Raiswell and Canfield, 2012). However, the quantification of aerosol dissolvable metals in the surface ocean is a highly challenging task operationally, attributed to the extremely complicated atmospheric and aquatic physicochemical and transformation processes before and after deposition, such as acidification, photoreduction, and inorganic and organic complexation (Meskhidze et al., 2019; Shi et al., 2012; Wang and Ho, 2020), which would transform aerosol chemical composition and then influence aerosol metal solubilities (Longo et al., 2016; Takahashi et al., 2011).

The lack of a standard methodology for assessing aerosol dissolvable metals is a major challenge, recent studies have suggested to standardize several typical leaching protocols for data compilation and flux estimate of the bioaccessible aerosol metals from different studies (Meskhidze et al., 2019; Perron et al., 2020b). Bioaccessible or bioavailable aerosol metals can be separated into dissolved and labile fractions (Meskhidze et al., 2019). The dissolved fraction is obtained by passing ultrapure water through 0.2 or 0.45 μm aerosol filters (hereafter ultrapure water leach) (Buck et al., 2006; Morton et al., 2013) to mimic the instantaneously dissolved aerosol metals in the surface ocean or dissolution in the rainwater (Buck et al., 2013). In terms of the labile fraction, acetate buffer (hereafter buffer leach) and Berger leaches are two of the most commonly used protocols. To access buffer leach, ammonia acetate buffer solution at pH 4.7 is generally used to mimic the impacts of rainwater dissolution (Baker and Jickells, 2006; Sarthou et al., 2003) or short period organic ligand complexation in seawater (Perron et al., 2020b). The Berger leach uses much stronger agents to release soluble metals, leached with acetic acid plus hydroxylamine hydrochloride for a fixed period of time, e.g., 1 day (Berger et al., 2008), which may represent the aeolian metals through the acidification and reduction in zooplankton's gut, complexation by strong ligands (e.g., siderophores), and reduction in the microenvironment (Berger et al., 2008; Meskhidze et al., 2019). The solubility obtained by Berger leach is considered the upper limit of aerosol metals solubility in marine environments (Meskhidze et al., 2019; Shelley et al., 2018).

In addition to accessing aerosol metal solubilities by using different leaching protocols, the other major challenge is to quantify the deposition fluxes of aerosol dissolvable metals to the surface ocean (Baker et al., 2016; Jickells et al., 2005; Mahowald et al., 2005). Although aerosol size strongly influences their deposition velocities and also reflects their sources, limited studies reported size-fractionated information in marine aerosol field observations (Baker et al., 2020; Buck et al., 2010; Gao et al., 2020; Kurisu et al., 2016b; Sakata et al., 2018; Yang et al., 2020), most likely due to limited sampling time to collect sufficient aerosol masses in scientific cruises. Many previous aerosol flux studies have only collected total suspended aerosol samples in the remote ocean. The deposition velocities used to estimate aerosol Fe fluxes may be oversimplified and may introduce large uncertainties (Duce et al., 1991). To access more accurate deposition fluxes estimates of bioaccessible aerosol metals, Foret et al. (2006) suggested to obtain the elemental mass distribution patterns in size-fractionated aerosols by using different leaching protocols at major oceanic regions.

Among biologically essential trace metals, iron (Fe) has attracted the greatest attention, attributed to its role as a major limiting factor for phytoplankton growth in the large area of the global ocean, such as the high-nutrient low-chlorophyll (HNLC) regions (Martin et al., 1994; Martin and Fitzwater, 1988; Moore et al., 2013). The Western Subarctic Gyre (Northwestern Pacific Ocean) is one of the HNLC regions in the global ocean but receives large amounts of fine anthropogenic and coarse lithogenic aerosols from East Asia. Recent studies reported that anthropogenic aerosol with high concentrations of Fe and high Fe solubility from East Asia is another important Fe source to the region (Ito et al., 2021; Kurisu et al., 2016b; Pinedo-Gonzalez et al., 2020). To quantify anthropogenic aerosol contribution, we plan to take size-fractionated aerosol samples and then determine the elemental composition of trace metals and Fe isotopic composition in the aerosols.

Fe isotopic composition is a potentially powerful parameter to distinguish the relative contribution of various Fe sources in the ocean. It has been reported that Fe from different sources possess specific isotopic features. A major atmospheric deposition, natural aerosol dust and loess, possesses relatively positive characteristics, with an average δ^{56}Fe value to be +0.1 ± 0.1 ‰ (Beard et al., 2003; Conway et al., 2019; Mead et al., 2013; Waeles et al., 2007).

doi:10.6342/NTU202302200

However, fractionated by high temperature combustion processes, the δ^{56}Fe of anthropogenic aerosols are significantly different from the value of natural dust. The reported value in anthropogenic aerosols range from -3.9 to -4.7 ‰ (Kurisu et al., 2019; Hsieh et al. 2023 this thesis). The biomass burning aerosol Fe has no significant fractionation signals, which may be due to the relatively low combustion temperature (approximately 300-500 ^{o}C), which does not cause significant Fe fractionation (Kurisu and Takahashi, 2019). In the deep ocean, δ^{56}Fe in hydrothermal fluids ranges from -0.69 to -0.12 ‰ (Fitzsimmons and Conway, 2023). The precipitated Fe oxyhydroxides during vent fluids transport are isotopically heavy compared to the initial isotopic ratio (Fitzsimmons and Conway, 2023). The δ^{56}Fe of reductive dissolved Fe in pore water is relatively light, ranging from -0.3 to -3.6 ‰ (Conway and John, 2014; Fitzsimmons and Conway, 2023; Fitzsimmons et al., 2016). However, the δ^{56}Fe of dissolved Fe in oxygenated sediment pore water is relatively heavy, +0.2±0.2 ‰ (Homoky et al., 2011; Radic et al., 2011).

In this study, we have collected both size-fractioned aerosols in the East China Sea (ESC) and lithogenic dusts directly from major Chinese deserts, including Taklimakan and Gobi Deserts, to investigate the potential effects of transport processes and aerosol sizes on aerosol metal solubilities and deposition fluxes. We also have systematically determined the solubilities of ultrapure water, buffer, and Berger leached metals and their corresponding deposition velocities among five different size-fractionated aerosols collected at Pengjiayu (PJ), a small islet located in the East China Sea (ECS), for one year. We plan to evaluate the discrepancy of the deposition velocities for different elements among the leaching treatments and the bias of flux estimates from a single velocity obtained by total suspended particle data. The findings of this study shall provide useful information for how to obtain a more representative estimate of the deposition fluxes of dissolvable aerosol metals regionally and globally. With the same aerosol samples, we also applied both δ^{56}Fe and elemental ratios to estimate the contribution of different aerosol sources for total aerosol Fe and dissolvable Fe in mass and fluxes.

In addition, we had the opportunity to join the GEOTRACES GP-02 subarctic Pacific Ocean transect study in 2017 to collect suspended particulate material in the water column to investigate the impacts of aerosol Fe on the spatial distribution of particulate Fe concentration and isotopic composition in the HNLC region. The west-east sampling stations are overlapped with the elevated AOD belt, where aerosols are transported from East Asia. This study would provide us the opportunity to investigate the importance of aerosols and other potential sources (e.g., lateral transport of resuspended sediments and pore water Fe) as the major sources of particulate Fe in the water column. Applying the elemental and isotopic composition of particulate Fe and examining the spatial distribution, this study shall provide valuable data to understand and evaluate Fe sources and cycling in the subarctic Pacific Ocean.

1.2 References

Baker, A.R. and Jickells, T.D., 2006. Mineral particle size as a control on aerosol iron solubility. Geophysical Research Letters, 33(17) DOI: 10.1029/2006gl026557.

Baker, A.R. et al., 2016. Trace element and isotope deposition across the air-sea interface: progress and research needs. Philos Trans A Math Phys Eng Sci, 374(2081) DOI: 10.1098/rsta.2016.0190.

Baker, A.R., Li, M. and Chance, R., 2020. Trace Metal Fractional Solubility in Size-Segregated Aerosols From the Tropical Eastern Atlantic Ocean. Global Biogeochemical Cycles, 34(6) DOI: 10.1029/2019gb006510.

Beard, B.L., Johnson, C.M., Von Damm, K.L. and Poulson, R.L., 2003. Iron isotope constraints on Fe cycling and mass balance in oxygenated Earth oceans. Geology, 31(7) DOI: 10.1130/0091-7613(2003)031<0629:Iicofc>2.0.Co;2.

Berger, C.J.M., Lippiatt, S.M., Lawrence, M.G. and Bruland, K.W., 2008. Application of a chemical leach technique for estimating labile particulate aluminum, iron, and manganese in the Columbia River plume and coastal waters off Oregon and Washington. Journal of Geophysical Research, 113 DOI: 10.1029/2007jc004703.

Buck, C.S., Landing, W.M. and Resing, J., 2013. Pacific Ocean aerosols: Deposition and solubility of iron, aluminum, and other trace elements. Marine Chemistry, 157: 117-130 DOI: 10.1016/j.marchem.2013.09.005.

Buck, C.S., Landing, W.M. and Resing, J.A., 2010. Particle size and aerosol iron solubility: A high-resolution analysis of Atlantic aerosols. Marine Chemistry, 120(1-4): 14-24 DOI: 10.1016/j.marchem.2008.11.002.

Buck, C.S., Landing, W.M., Resing, J.A. and Lebon, G.T., 2006. Aerosol iron and aluminum solubility in the northwest Pacific Ocean: Results from the 2002 IOC cruise. Geochemistry, Geophysics, Geosystems, 7(4) DOI: 10.1029/2005gc000977.

Chen, C.C. et al., 2022. Nickel superoxide dismutase protects nitrogen fixation in Trichodesmium. Limnology and Oceanography Letters, 7(4): 363-371 DOI: 10.1002/lol2.10263.

Conway, T.M. et al., 2019. Tracing and constraining anthropogenic aerosol iron fluxes to the North Atlantic Ocean using iron isotopes. Nat Commun, 10(1): 2628 DOI: 10.1038/s41467-019-10457-w.

Conway, T.M. and John, S.G., 2014. Quantification of dissolved iron sources to the North Atlantic Ocean. Nature, 511(7508): 212-5 DOI: 10.1038/nature13482.

Duce, R.A. et al., 1991. The atmospheric input of trace species to the world ocean. Global Biogeochemical Cycles, 5(3): 193-259 DOI: 10.1029/91gb01778.

Fitzsimmons, J.N. and Conway, T.M., 2023. Novel Insights into Marine Iron Biogeochemistry from Iron Isotopes. Ann Rev Mar Sci, 15: 383-406 DOI:

doi:10.6342/NTU202302200

10.1146/annurev-marine-032822-103431.

Fitzsimmons, J.N. et al., 2016. Dissolved iron and iron isotopes in the southeastern Pacific Ocean. Global Biogeochemical Cycles, 30(10): 1372-1395 DOI: 10.1002/2015gb005357.

Foret, G., Bergametti, G., Dulac, F. and Menut, L., 2006. An optimized particle size bin scheme for modeling mineral dust aerosol. Journal of Geophysical Research, 111(D17) DOI: 10.1029/2005jd006797.

Gao, Y. et al., 2020. Particle-Size Distributions and Solubility of Aerosol Iron Over the Antarctic Peninsula During Austral Summer. Journal of Geophysical Research: Atmospheres, 125(11) DOI: 10.1029/2019jd032082.

Ho, T.Y. et al., 2003. The elemental composition of some marine phytoplankton. Journal of Phycology, 39(6): 1145-1159 DOI: DOI 10.1111/j.0022-3646.2003.03-090.x.

Homoky, W.B. et al., 2011. Iron and manganese diagenesis in deep sea volcanogenic sediments and the origins of pore water colloids. Geochimica et Cosmochimica Acta, 75(17): 5032-5048 DOI: 10.1016/j.gca.2011.06.019.

Ito, A., Ye, Y., Baldo, C. and Shi, Z., 2021. Ocean fertilization by pyrogenic aerosol iron. npj Climate and Atmospheric Science, 4(1) DOI: 10.1038/s41612-021-00185-8.

Jickells, T.D. et al., 2005. Global iron connections between desert dust, ocean biogeochemistry, and climate. Science, 308(5718): 67-71 DOI: 10.1126/science.1105959.

Jickells, T.D., Baker, A.R. and Chance, R., 2016. Atmospheric transport of trace elements and nutrients to the oceans. Philos Trans A Math Phys Eng Sci, 374(2081) DOI: 10.1098/rsta.2015.0286.

Kurisu, M. and Takahashi, Y., 2019. Testing Iron Stable Isotope Ratios as a Signature of Biomass Burning. Atmosphere, 10(2) DOI: 10.3390/atmos10020076.

Kurisu, M., Takahashi, Y., Iizuka, T. and Uematsu, M., 2016. Very low isotope ratio of iron in fine aerosols related to its contribution to the surface ocean. Journal of Geophysical Research: Atmospheres, 121(18): 11,119-11,136 DOI: 10.1002/2016jd024957.

Longo, A.F. et al., 2016. Influence of Atmospheric Processes on the Solubility and Composition of Iron in Saharan Dust. Environ Sci Technol, 50(13): 6912-20 DOI: 10.1021/acs.est.6b02605.

Mackey, K.R., Chien, C.T., Post, A.F., Saito, M.A. and Paytan, A., 2015. Rapid and gradual modes of aerosol trace metal dissolution in seawater. Front Microbiol, 5: 794 DOI: 10.3389/fmicb.2014.00794.

Mahowald, N.M. et al., 2005. Atmospheric global dust cycle and iron inputs to the ocean. Global Biogeochemical Cycles, 19(4): n/a-n/a DOI: 10.1029/2004gb002402.

Martin, J.H. et al., 1994. Testing the iron hypothesis in ecosystems of the equatorial Pacific

Ocean. Nature, 371(6493): 123-129 DOI: 10.1038/371123a0.

Martin, J.H. and Fitzwater, S.E., 1988. Iron deficiency limits phytoplankton growth in the north-east Pacific subarctic. Nature, 331(6154): 341-343 DOI: 10.1038/331341a0.

Mead, C., Herckes, P., Majestic, B.J. and Anbar, A.D., 2013. Source apportionment of aerosol iron in the marine environment using iron isotope analysis. Geophysical Research Letters, 40(21): 5722-5727 DOI: 10.1002/2013gl057713.

Meskhidze, N. et al., 2019. Perspective on identifying and characterizing the processes controlling iron speciation and residence time at the atmosphere-ocean interface. Marine Chemistry, 217 DOI: 10.1016/j.marchem.2019.103704.

Moore, C.M. et al., 2013. Processes and patterns of oceanic nutrient limitation. Nature Geoscience, 6(9): 701-710 DOI: 10.1038/ngeo1765.

Morel, F.M.M., Lam, P.J. and Saito, M.A., 2020. Trace Metal Substitution in Marine Phytoplankton. Annual Review of Earth and Planetary Sciences, 48(1): 491-517 DOI: 10.1146/annurev-earth-053018-060108.

Morton, P.L. et al., 2013. Methods for the sampling and analysis of marine aerosols: results from the 2008 GEOTRACES aerosol intercalibration experiment. Limnology and Oceanography: Methods, 11(2): 62-78 DOI: 10.4319/lom.2013.11.62.

Paytan, A. et al., 2009. Toxicity of atmospheric aerosols on marine phytoplankton. Proceedings of the National Academy of Sciences of the United States of America, 106(12): 4601-4605 DOI: 10.1073/pnas.0811486106.

Perron, M.M.G. et al., 2020. Assessment of leaching protocols to determine the solubility of trace metals in aerosols. Talanta, 208: 120377 DOI: 10.1016/j.talanta.2019.120377.

Pinedo-Gonzalez, P. et al., 2020. Anthropogenic Asian aerosols provide Fe to the North Pacific Ocean. Proc Natl Acad Sci U S A, 117(45): 27862-27868 DOI: 10.1073/pnas.2010315117.

Radic, A., Lacan, F. and Murray, J.W., 2011. Iron isotopes in the seawater of the equatorial Pacific Ocean: New constraints for the oceanic iron cycle. Earth and Planetary Science Letters, 306(1-2): 1-10 DOI: 10.1016/j.epsl.2011.03.015.

Raiswell, R. and Canfield, D.E., 2012. The Iron Biogeochemical Cycle Past and Present. Geochemical Perspectives, 1(1): 1-220 DOI: 10.7185/geochempersp.1.1.

Sakata, K. et al., 2018. Custom-made PTFE filters for ultra-clean size-fractionated aerosol sampling for trace metals. Marine Chemistry, 206: 100-108 DOI: 10.1016/j.marchem.2018.09.009.

Sarthou, G. et al., 2003. Atmospheric iron deposition and sea-surface dissolved iron concentrations in the eastern Atlantic Ocean. Deep Sea Research Part I: Oceanographic Research Papers, 50(10-11): 1339-1352 DOI: 10.1016/s0967-0637(03)00126-2.

Shelley, R.U., Landing, W.M., Ussher, S.J., Planquette, H. and Sarthou, G., 2018. Regional trends in the fractional solubility of Fe and other metals from North Atlantic aerosols (GEOTRACES cruises GA01 and GA03) following a two-stage leach. Biogeosciences, 15(7): 2271-2288 DOI: 10.5194/bg-15-2271-2018.

Shi, Z.B. et al., 2012. Impacts on iron solubility in the mineral dust by processes in the source region and the atmosphere: A review. Aeolian Research, 5: 21-42 DOI: 10.1016/j.aeolia.2012.03.001.

Takahashi, Y., Higashi, M., Furukawa, T. and Mitsunobu, S., 2011. Change of iron species and iron solubility in Asian dust during the long-range transport from western China to Japan. Atmospheric Chemistry and Physics, 11(21): 11237-11252 DOI: 10.5194/acp-11-11237-2011.

Waeles, M., Baker, A.R., Jickells, T. and Hoogewerff, J., 2007. Global dust teleconnections: aerosol iron solubility and stable isotope composition. Environmental Chemistry, 4(4) DOI: 10.1071/en07013.

Wang, B.-S. and Ho, T.-Y., 2020. Aerosol Fe cycling in the surface water of the Northwestern Pacific ocean. Progress in Oceanography, 183 DOI: 10.1016/j.pocean.2020.102291.

Yang, T. et al., 2020. Solubilities and deposition fluxes of atmospheric Fe and Cu over the Northwest Pacific and its marginal seas. Atmospheric Environment, 239 DOI: 10.1016/j.atmosenv.2020.117763.

Chapter 2

The solubility and deposition flux of East Asian aerosol metals in the East China Sea: the effects of aeolian transport processes

By

Chih-Chiang Hsieh[a,b], Chen-Feng You[c], and Tung-Yuan Ho[*a,b]

[a] Research Center for Environmental Changes, Academia Sinica, Taipei, Taiwan

[b] Institute of Oceanography, National Taiwan University, Taipei, Taiwan

[c] Department of Earth Sciences, National Cheng Kung University, Tainan, Taiwan

[*]corresponding author: tyho@gate.sinica.edu.tw

Published in *Marine Chemistry*.

Paper Citation:

Chih-Chiang Hsieh, Chen-Feng You, Tung-Yuan Ho, The solubility and deposition flux of East Asian aerosol metals in the East China Sea: The effects of aeolian transport processes, *Marine Chemistry*, 2023, 104268, ISSN 0304-4203, ttps://doi.org/10.1016/j.marchem.2023.104268.

2.0 Abstract

Aerosol dissolvable metals are considered to be readily bioaccessible so that their input would influence the growth and composition of marine phytoplankton and affect elemental cycling globally. However, it is highly challenging to measure or estimate reliable deposition fluxes of aerosol dissolvable metals in the ocean partially due to the impacts of complicated processes involved in pre- and post-deposition of aerosols. We have collected lithogenic dust from major Chinese deserts and size-fractionated aerosols from the East China Sea (ECS) to study the variations of their dissolvable metals by using three operationally defined leaching protocols (ultrapure water, buffer, and Berger leaches). We have systematically investigated the changes of the distribution patterns of the metals to evaluate the potential impacts of the transport processes on the flux estimates of different elements. In addition to the extremely high solubilities observed for anthropogenic type elements, we found variations for solubilities of lithogenic type elements (Ti, Al, Fe) increase with increasing sizes by the three leaching treatments. Without knowing the size specific information (mass and solubility), our observations indicate that the deposition fluxes of lithogenic type elements would be significantly overestimated. Compared with the solubility of the desert dust, we found that all solubilities for lithogenic type elements in the largest aerosols were significantly enhanced. For example, the Fe solubilities increased up to 68, 6, and 3 folds for ultrapure water, buffer, and Berger treatments, respectively. Attributed to the difference of the impacts of the transport processes in different regions, the extent of the enhancement would be region specific. Comparing some other recent laboratory studies, we argue that the solubilities obtained by buffer and Berger leaches are more realistic to represent aerosol solubility in the ocean than ultrapure water leach. It would be essential to carry out similar field studies in other regions as this study to obtain region specific parameters of dissolvable aerosol metals to achieve better global modeling estimates on the fluxes of dissolvable aerosol metals in the ocean.

doi:10.6342/NTU202302200

2.1 Introduction

The availability of the whole suite of biologically essential dissolved trace metals (e.g., Fe, Co, Cu, Zn, Ni) is a major factor deciding the growth and composition of different phytoplankton groups in marine euphotic zone (Chen et al., 2022; Ho et al., 2003; Paytan et al., 2009) and thus influencing material cycling in the ocean (Mackey et al., 2015; Martin and Fitzwater, 1988; Morel et al., 2020). Aerosols are a major source of dissolved trace metals in the euphotic zone of the ocean (Jickells et al., 2016). Before and after depositing in the euphotic zone, aerosols go through complicated atmospheric and aquatic physicochemical and transformation processes, such as acidification, photoreduction, and organic complexation (Meskhidze et al., 2019; Shi et al., 2012; Wang and Ho, 2020). Although the complicated processes would transform aerosol properties and influence aerosol metal solubilities (Longo et al., 2016; Takahashi et al., 2011), their impacts on the solubilities largely remain unclear (Meskhidze et al., 2019).

To mimic the impacts of the complicated physicochemical and transformation processes on aerosol metal solubilities, recent studies have suggested to standardize several typical leaching protocols for data compilation and flux estimate of the bioaccessible aerosol metals from different studies (Meskhidze et al., 2019; Perron et al., 2020). Bioaccessible aerosol metals are commonly and operationally defined as dissolved and labile fractions (Meskhidze et al., 2019). Reflecting instantaneously dissolved aerosol metals in the surface ocean, the dissolved fraction is obtained by passing ultrapure water through 0.2 or 0.45 μm aerosol filters (hereafter ultrapure water leach) (Buck et al., 2006; Morton et al., 2013) and considered to be fully bioavailable to phytoplankton (Raiswell and Canfield, 2012). To assess the labile fraction, acetate buffer (hereafter buffer leach) and Berger leaches are two of the most commonly used protocols. Buffer leach generally uses ammonia acetate buffer solution at pH 4.7 to mimic aerosol metals dissolution processes through atmospheric transport processes, such as the impacts of rainwater (Baker and Jickells, 2006; Sarthou et al., 2003) or short period ligand complexation in seawater (Perron et al., 2020). The Berger leach uses much stronger agents to release soluble metals, leached with acetic acid plus hydroxylamine hydrochloride for a fixed period of time, e.g., 1 day (Berger et al., 2008). The solubility obtained by Berger leach is thus considered as the upper limit of aerosol metals solubility in marine environment (Meskhidze et al., 2019; Shelley et al., 2018). It has been proposed that the solubility of Berger leach may represent the dissolvable fraction in aeolian metals through the acidification and reduction in zooplankton’s gut, complexation by strong ligands (e.g., siderophores), and reduction in the microenvironment (Berger et al., 2008; Meskhidze et al., 2019).

In addition to accessing aerosol metal solubilities during transport processes by using different leaching protocols, the other major challenge is to quantify the deposition fluxes of aerosol dissolvable metals to the surface ocean (Baker et al., 2016; Jickells et al., 2005; Mahowald et al., 2005). As aerosol sizes strongly influence their deposition velocities and also reflect their sources, aerosol sizes are highly associated with the deposition fluxes of dissolvable aerosol metals. Moreover, the impacts of aeolian transport processes on aerosol metal solubility are also associated with surface area to volume ratios in aerosols (Baker and Jickells, 2006). However, most likely due to limited sampling time to collect sufficient aerosol masses in scientific cruises, many previous aerosol flux studies have only collected total suspended aerosol samples in the remote ocean. Attributed to the spatial deviation fo aerosol size distribution and their composition and transport processes, the deposition fluxes of aerosol metals are likely to be element specific and also location specific. For example, the study of Hsieh et al. (2022) observed that the Fe solubilities of size-fractionated aerosols either for ultrapure water or buffer leaches showed difference up to two orders of magnitude between the finest and coarsest aerosols. Without using size-fractionated aerosols and their size-specific solubilities and deposition velocities, dissolvable Fe flux would be greatly overestimated (Hsieh et al., 2022). To obtain the reliable deposition fluxes of dissolvable aerosol metals and to reduce the uncertainties of the estimated fluxes by models, it is essential to obtain the distribution patterns of elemental concentrations in different size aerosol fractions by using different leaching protocols at major oceanic regions (Foret et al., 2006).

The East China Sea (ECS) is located at the downwind side of mainland China, a major aerosol source to the global ocean. The ECS receives a large amount of aerosols mixed with relatively fine anthropogenic aerosols and coarse lithogenic dust, originating from the populous Eastern China (Cheng et al., 2012) and Western China with major desserts, respectively (Fig. 2.1). During the northeastern monsoon and the Westerly prevailing periods, generally ranging from October to early May, the mixed aerosols accompanying with other pollutants (e.g., inorganic acids) are transported to the ECS, the adjacent marginal seas, and

doi:10.6342/NTU202302200

the Northwestern and subarctic Pacific Oceans. Contrarily, during the southwestern (SW) monsoon season from June to September, the ECS mainly receives aerosols originating from the South China Sea and Southeastern Asia. The ECS thus provides an excellent platform to study how aerosol metal solubility is affected by the natural transport process and the interaction with anthropogenic pollutants.

In this study, we have collected both lithogenic dusts directly from major Chinese deserts, including Taklimakan and Gobi Deserts, and the size-fractionated aerosols from the ECS to investigate the potential effects of transport processes and aerosol sizes on aerosol metal solubilities and deposition fluxes. We have systematically determined the solubilities of ultrapure water, buffer, and Berger leached metals and their corresponding deposition velocities among five different size-fractionated aerosols collected at Pengjiayu (PJ), a small islet located in the ECS, for one year. We have evaluated the discrepancy of the deposition velocities for different elements among the leaching treatments and the bias of flux estimates from a single velocity obtained by total suspended particle data. The findings of this study shall provide useful information for how to obtain a more representative estimate of the deposition fluxes of dissolvable aerosol metals regionally and globally.

2.2 Method

2.2.1 Sampling sites and method

For desert dust, the samples were directly collected from the land surface of three major Chinese deserts, Tengger Desert (TG, part of Gobi Desert, at 39°00’N, 103°34’E), Taklimakan Desert (TK1, at 36°48’N, 82°16’E; TK2, at 41°04’N, 83°29’E), and Qaidam Desert (QD, at 37°20’N, 97°09’E) (Fig. 2.1). The desert samples serve as the original lithogenic dust without being impacted by aeolian transport processes. The ECS aerosol sampling site, Pengjiayu (PJ, 25.63°N, 122.08°E), is located at 66 km from the northernmost point of Taiwan (Fig. 2.1). Except for limited governmental staff from Central Weather Bureau and Coastal Guard Administration, there are no other general residents or any other anthropogenic activities on the islet. The top of the volcanic islet, with area of 1.1 km^2, is mainly covered with grasses. PJ thus serves as an ideal aerosol time series sampling site for the East China Sea. Set up right next to the weather station of Central Weather Bureau on PJ, the high volume aerosol sampler (TISCH Environmental Inc., US, MODEL-TE-5170) was coupled with a cascade impactor

(TISCH Environmental Inc., US, Series 235) to collect size-fractionated aerosol samples with average flow rate to be 1.0 ± 0.1 m^{-3} min^{-1}. The cascade impactor sorted aerosols into five size fractions, including stage 1 (>7.3 μm), stage 2 (3.1-7.3 μm), stage 3 (1.6-3.1 μm), stage 4 (1.0-1.6 μm), and stage 5 (0.57-1.0 μm) (Table 2.1). Size-fractionated aerosol samples were collected by polytetrafluoroethylene filters (TE-230-PTFE, Tisch Environmental Inc., US). Fine and coarse aerosols mentioned in this study refer to $PM \leq 3$ (stage 3-5) and $PM>3$ (stage 1 and 2), respectively. Since aerosol samples were not evenly distributed into 10 strips on each slotted filter in the impactor, we used the software ImageJ to measure the grayscale intensity value of each strip and summed up all strips in the whole filter. We then carried out total digestion or other leaching treatments by using one of the strips to calculate the concentrations of each strip and the whole filter by using the ratios of the intensities. To collect sufficient masses for the measurement of elemental and isotopic composition for different treatments, aerosols were continuously collected for 7-8 days on one filter every month from September 2019 to August 2020. As the sampler was under maintenance in October and November in 2019, data are not available for the two months. Aerosol samples were stored in a -20°C freezer before further chemical processes. Right before the chemical processes, each filter was freeze-dried and weighed.

2.2.2 Leaching procedures and quantification and aerosol metals

We have followed the procedures suggested in the GEOTRACES Cookbook to process aerosol samples and to clean vials used for sample storage and digestion (Cutter et al., 2017). All acids and bases used for sampling pretreatment were ultra-high purity grade, including nitric acid (HNO_3), hydrochloric acid (HCl), hydrofluoric acid (HF), acetic acid (CH_3COOH), ammonium hydroxide (NH_4OH)(J. T. Baker), except hydroxylamine hydrochloride ($NH_2OH.HCl$), which was high purity grade (>99%, Merck). Aerosol filters were sub-sampled with a trace metal clean ceramic scissor for different leaching treatments. All of the laboratory procedures were carried out in a positive pressurized class 5 cleanroom by wearing powder-free polyvinyl chloride (PVC) gloves while handling sample pretreatment procedures.

In addition to total digestion, we conducted three different leaching protocols, including instantaneous ultrapure water, acetate buffer (buffer), and Berger treatments. The ultrapure water leach was obtained by immersing aerosol samples in 5 mL of ultrapure water (> 18.2 MΩ.cm) with gentle shaking for 10 seconds. The leaching solution was then filtered into a pre-acid washed 15 mL

doi:10.6342/NTU202302200

polypropylene vial through a 13 mm pre-acid washed 0.2 μm hydrophilic PTFE syringe filter (Advantec) (Sarthou et al., 2003). Samples for buffer leach were soaked in 8 mL of ammonium acetate (1.4 M, pH 4.7) at room temperature for 1 h (Baker and Jickells, 2006). Samples for Berger leach were heated at 90°C (heater temperature) for 10 min with 5 mL leaching solution containing 25% acetic acid and 0.02 M hydroxylamine hydrochloride in PFA vials (Savillex)(Berger et al., 2008). The leaching treatment was maintained at room temperature for 24 h before further processes. Samples for total digestion were heated for 4 h at 120°C (heater temperature) in 2ml of a freshly prepared mixed solution containing 4M HF, 4M HCl, and 4M HNO_3 (Eggimann and Betzer, 1976). For buffer leach, Berger leach, and total digestion, after removing the filters, the leaching or digested solution were centrifuged to remove insoluble particles (Baker et al., 2006; Sarthou et al., 2003). The supernatant was dried up with open caps then the dried samples were redissolved in 10 ml 0.5 M HNO3 solution at 120°C (heater temperature) with closed caps for 1 h for further concentration quantification. The solubilities of the four leach fractions were calculated by dividing the leached concentrations to the total concentrations for individual elements. The filter blanks of each treatment were obtained by using new filters treated with exactly the same leaching procedures as samples. The concentrations of more than 90 % of the samples were two orders of magnitude higher than the blank and all samples were one order of magnitude higher than the blank (Table S2.1).

All of the leached or digested samples were added with 1 ppb (final concentration) of indium and rhodium as internal standards and were diluted with 0.5 M HNO_3 solution accordingly, then were analyzed by a sector field high resolution ICPMS (Element XR, Thermo Fisher Scientific). The isotopes of ^{103}Rh, 111Cd, 115In, 207Pb and 208Pb were determined at low resolution (M/ΔM~ 300), and ^{27}Al, ^{47}Ti, ^{49}Ti , ^{51}V, ^{55}Mn, ^{54}Fe, ^{56}Fe, ^{59}Co, ^{60}Ni, ^{64}Zn, ^{66}Zn, ^{103}Rh, and ^{115}In were analyzed at medium resolution (M/ΔM ~4000). In this study, we used two types of reference material for accuracy validation, including Arizona Test Dust (ATD, < 3 μm, Powder Technologies Inc.) to be lithogenic type CRM and NIES CRM No. 28, an urban aerosols collected in Beijing (BJ, National Institute for Environmental Studies), as anthropogenic type CRM. The ratios of our measured concentrations to the certified or reported value for ATD were 92% (Al), 100% (Ti), 102% (V), 92% (Mn), and 97% (Fe) (Shelley et al., 2015); for BJ, 92% (Al), 93% (Ti), 101% (V), 95% (Mn), 97% (Fe), 125% (Co), 114% (Ni), 102% (Zn), 98% (Cd), and 99% (Pb) (Table S2.2).

2.3 Result

2.3.1 The variations of concentration and solubility

Figure 2.2 shows the variations in concentrations and solubility of the metals obtained by three different leaching and digestion protocols for the size-fractionated aerosols. The monthly data of elemental concentrations (pmol m^{-3}) for the same size of particles by using relative standard deviations are compiled in Table S2.3-S2.7. We present the elements from upper left to bottom right with low to high deviation sequences, which are Cd, Zn, Pb, Mn, Co, Ni, V, Al, Fe, and Ti (Fig. 2.2). Showing decreasing concentrations with increasing sizes, Cd and Zn exhibit the highest solubilities and smallest deviations among different protocols (Table S2.3). The average solubilities of ultrapure water, buffer, and Berger phases were 87, 86, and 80 % and 72, 77, and 79 % for Cd and Zn, respectively.

The concentration deviations of the elements, Pb, Mn, Co, and Ni, ranged between 39 % and 72 %, with the smallest deviation in the smallest size (0.57 μm) and increasing with sizes (Table S2.3). For the largest size aerosol, the difference of the concentrations was up to one order of magnitude among different leaching protocols. In terms of solubility, the average solubilities ranged from 17 to 81 % and decreased with increasing sizes in all leaching fractions. For example, the average solubilities of Co for the ultrapure water, buffer, and Berger leaches were 73, 26, 27, 28, 19 % and 64, 39, 39, 29, 24 % and 58, 37, 32, 31, 37 % for the aerosol fractions from small to large ones, respectively.

The third group of elements, including V, Al, Fe, and Ti, exhibit more than 90 % of concentration deviations among the protocols (Table S2.3). The deviations were still relatively small for size 0.57 μm but were significantly deviated for large size aerosols, with deviations up to 3 orders of magnitude for 7.3 μm aerosols. In terms of solubility, the average solubilities of ultrapure water, buffer, and Berger leaches for the largest aerosols were 2.2, 6.1, 22 % and 0.37, 5.1, 23 % and 0.19, 2.4, 12 % and 0.07, 0.70, and 2.3 % for V, Al, Fe, and Ti, respectively.

To highlight the deviation patterns of the elemental solubilities among protocols and aerosol sizes, we present the deviations of the solubility of ultrapure water, buffer, and Berger treatments for the smallest and largest size aerosols (0.57 and 7.3 μm) with the sequence of deviation from low to high (Fig. 2.3). The average solubilities of 0.57 μm aerosol were all similarly high and more than 50% for most of the elements, with the values (average±S.D.) to be 88±13, 91±12, 77±18, 80±12, 65±18, 68±14, 85±13, 42±17, 48±19, and 9.3±4.5 % for Cd, Zn, Pb, Mn, Co, Ni, V, Al, Fe, and Ti, respectively (Fig. 2.3). For 7.3 μm aerosols, the

doi:10.6342/NTU202302200

deviation patterns of the solubilities were comparable to the deviation patterns of the concentrations among the three groups of elements mentioned above.

2.3.2 Enrichment Factor

Since aerosols are composed of multiple sources, the elemental ratios of metals can be significantly different from the composition in lithogenic dust. The enrichment factor (EF) of metals in aerosol samples may be useful to evaluate the relative contribution of the non-crustal sources. The enrichment factor (EF) is generally expressed as follows:

$$EF = (Metals/Ti)_{aerosol} / (Metals/Ti)_{UCC}$$

The term, $(Metals/Ti)_{UCC}$, stands for the reference value of the upper continental crust, which is cited from Hu and Gao (2008) in this study.

The EF of size-fractionated aerosol metals are shown in Figure 2.4 and Table S2.8. Overall, the averaged EF of all sampling periods decrease with increasing sizes for all elements. In terms of the deviation of the EF in each size, Cd, Zn, Pb, Ni show relatively high variations, spanning up to one order of magnitude for most sizes. For example, the ranges for Cd were 199-3754, 67-1290, 12-317, 5.7-108, and 3.1-77 from the smallest to largest sizes, respectively. These high EF values indicate high anthropogenic aerosol contribution to the elements for all sizes. Even in coarse fractions, the average EF of Cd, Zn, Pb were significantly higher than 1, which are 32, 14, and 7.1, respectively. The coarse aerosol with high anthropogenic aerosol contribution might be attributed to coarse anthropogenic aerosols or the aggregation of fine anthropogenic aerosols on the coarse samples (Li et al., 2017). Seasonally, the average EF of Cd, Pb, and V were significantly higher ($p < 0.05$) during the NE monsoon period than the SW monsoon period (Fig. S2.1). Using Cd as an example, the EF value (average±S.D.) with increasing sizes were 2025±1024, 645±451, 167±112, 46±28, 29±20 and 364±233, 110±61, 28±23, 11±7.3, 6.7±5.1 for the NE and SW monsoon seasons, respectively. All elements (except Zn) show significant seasonality in size 0.57 μm ($p < 0.05$).

For Al and Fe, the average EF values for the fine aerosols are 1.3±1.2 and 1.8±0.4, respectively. Even for the smallest size, the averaged EF are only 2.2 and 2.1 for Al and Fe,

doi:10.6342/NTU202302200

respectively. However, the ultrapure water solubilities of fine aerosols for Al and Fe were extremely high, 38 and 50 % (Fig. 2.4), indicating relatively high anthropogenic aerosol fractions in fine aerosols. The comparable EF between anthropogenic and lithogenic aerosols for Al and Fe indicates that EF is not a useful indicator to distinguish the relative contribution of crustal and non-crustal sources for Al and Fe.

2.4 Discussion

2.4.1 EF and leaching solubility

We found that the coupling of EF and solubilities may provide additional information to evaluate the sources of aerosols (Fig. 2.4). Using Al as an example, the EF of Al for the two extreme size aerosols (0.57 and 7.3 μm) are statistically indistinguishable, 2.2± 1.9 and 0.84±0.55, but their averaged ultrapure water solubilities show dramatic difference up to two orders of magnitude, 38±15 and 0.37±0.52 %, respectively. Normalized to the surface area of these two size aerosols, the Al solubility of 0.57 μm aerosols is still one order of magnitude higher than 7.3 μm aerosols. Thus, the extremely high ultrapure water solubility observed in the finest aerosols, whose EF is relatively close to 1, suggests that the soluble Al in the fine aerosols mainly originated from anthropogenic aerosols. Sakata et al. (2022) also observed Al-sulfate and organic complexes in PM1.3 of the Western Pacific Ocean aerosol, strongly supported our suggestion. Similarly, the EF of Fe for the two sizes of aerosols are 2.1±0.6 and 1.4±0.1, but the ultrapure water solubilities were 50±22 and 0.19±0.27 %, respectively. We did observe correspondingly high solubilities in the fine aerosols with slightly higher EF for Fe, indicating that anthropogenic aerosols were also the major source of ultrapure water Fe in fine particles. For Cd, Zn, and Pb, their EF in almost all coarse aerosol samples were significantly higher than 1, and the solubilities were all relatively high. For Mn (and Co), the EF were mostly under 10. Although the EF values in fine and coarse particles were slightly different, 4.4±4.0 and 1.3±0.4, their ultrapure water solubilities were statistically insignificant, 65±20 and 44±21 %, respectively. In brief, the Ti-normalized EF of Al, Fe, Mn, and Co in fine aerosols are either insignificantly different or just slightly higher than the EF in coarse aerosols in the samples. For Mn, Co, Ni, and V with EF smaller than 2, we observed high deviations of ultrapure water solubilities, ranging from 15-95, 4.2-59, 4.5-17, and 0.2-14 %, respectively, indicating that the information of EF alone is impractical to be a useful proxy to evaluate the solubilities and the relative contribution of non-crustal source. For Cd, Zn, Pb, Ni, V, Mn and Co, the EF were up to 100 or even 1000, and their ultrapure water solubilities were all relatively high, with average solubilities for data with EF higher than 10 to be 86±15, 77±19, 45±16, 59±25, 90±14, 92±12, and 74±23 %, respectively. Overall, the coupling information of EF and solubilities serves as a much more reliable and useful indicator than EF itself to reflect the relative contribution of crustal and non-crustal sources on the ultrapure water metals in size-fractionated aerosols.

The comparison of the solubility obtained by the three leaching treatments for the size-fractionated aerosols exhibits elemental dissolution characteristics among aerosol sources. The results show that most metals in fine aerosols are released into water instantaneously (Fig. 2.2-2.4). Previous studies reported that anthropogenic type metals exist in highly soluble salts, mainly nitrate and sulfate, or complexed with organic ligands in aerosols (Sakata et al., 2014), which explains the high metal solubilities observed in fine aerosols. However, the ultrapure water fraction of Pb are significantly lower than other fractions, which may be attributed to the contribution of relatively insoluble forms, $2PbCO_3 \cdot Pb(OH)_2$ and $PbSO_4$, in both fine and coarse aerosols (Sakata et al., 2017). In terms of lithogenic type elements (e.g., Al, Fe, and Ti) in the coarsest aerosol, their ultrapure water solubilities were extremely low, which are attributed to their relatively stable crystalline lattice structure in lithogenic aerosols (Nicholls, 1963). However, their buffer and Berger solubilities increased significantly in comparison to ultrapure water solubilities in the coarsest fraction (Fig. 2.3). Using ultrapure water and buffer leaches in aerosol samples collected in a Chinese city, Li et al. (2023) also reported that the solubility ratios of buffer and ultrapure water leaches were significantly higher for Al and Fe than other metals with high ultrapure solubilities.

2.4.2 Reflecting the impacts of the transport processes on solubilities

We compile the solubility data between the desert dust (hereafter the dust in section 4.2) and the largest size aerosols (size cut-off 7.3 μm, hereafter the aerosols in 4.2) to evaluate the potential impacts of aeolian transport processes on the three different solubilities of the largest aerosols collected (Fig. 2.4, Table S2.9). Overall, except Cd, Zn, and Pb in the aerosols, the enrichment factors of the dust and the aerosols are both close to 1 for most of the elements measured (Fig. 2.4). The averaged EF of Cd, Zn, and Pb in the aerosols were up to

doi:10.6342/NTU202302200

25, 12, and 5.9; and their averaged ultrapure water solubilities were 80, 47, and 14 %, respectively. However, the ultrapure water solubilities of Cd, Zn, and Pb were extremely low in the dust, which were down to 0.14, 0.02, and 0.01 %, respectively. The high EF and contrasting solubilities between the aerosols and the dust indicate that the largest aerosols are still mixed with a significant amount of Cd, Zn, and Pb originating from anthropogenic aerosols. For buffer and Berger leaches, the solubilities of Cd and Pb in the dust were significantly enhanced to 77 and 24 % for buffer leach, and 81 and 39 % for Berger leach, respectively, which are relatively close to the value observed in the aerosols. These significant solubility enhancements in the dust can be attributed to their relatively soluble composition in the dust. Using Cd as an example, the enhancement of solubility is likely caused by the most commonly found primary speciation in the dust, Cd oxides and sulfide (ATSDR, 1999), in which the solubilities are much higher in weak acid than in ultrapure water. Since buffer leach has been generally proposed to represent the effect of rainwater and organic ligand complexation fractions in seawater (Baker et al., 2006; Perron et al., 2020; Sarthou et al., 2003), these enhanced high solubilities observed in the dust indicate that the solubilities of Cd and Pb for lithogenic aerosols would be relatively high in rainwater or seawater. However, the averaged solubilities of the buffer and Berger leaches of the dust for Zn were 2.8 and 12 %, respectively, which were significantly lower than the levels of Cd and Pb, most likely attributed to the relatively rigid mineral composition of Zn in the dust, such as willemite (zinc silicate) (Gunchin et al., 2021). Similar patterns for Mn, Co, Ni, and V are observed as Zn. Specifically, the effects of the three leaching treatments on Mn were close to the patterns of Cd and Pb. The buffer and Berger solubilities of Co, Ni, and V in the dust were significantly lower than the value observed in the aerosols. For Al and Fe, the instant solubilities for both the dust and the aerosols were both extremely low and relatively close to each other; the buffer and Berger solubilities were significantly higher in the aerosols than the value observed in the dust.

We further present the solubility ratios between the aerosols to the dust ($S_{7.3\mu m}/S_{desert}$) from the three leaches together to illustrate the deviation patterns among all of the metals measured (Fig. 2.5). We found a converging trend of the ratios of the three leach treatments from anthropogenic to lithogenic type metals, which is defined as litho-tendency here for the elements measured. The ratios of ultrapure water leach decrease with litho-tendency with the value ranging from 3,017 to 68. As pointed out previously, except Cd, Zn, and Pb, the low solubilities and EF (close to 1) in the aerosols indicate that the other metals are mostly lithogenic origin. The elevated ratios thus suggest that aeolian transport processes enhance ultrapure water solubilities of most elements significantly in the largest aerosols collected. Previous studies have reported that highly soluble metal salts are formed during transport processes with inorganic acids, such as sulfuric and nitric acid, from SO2 and NOx emissions, respectively. (Baker et al., 2021; Seinfeld and Pandis, 2016). By chemical reactions with the acids via in-cloud processes, the newly formed salts may include metal nitrate, sulfate, chloride, and organic complexes for Pb, Zn, and Mn (Ohta et al., 2006; Sakata et al., 2014; Takahashi et al., 2011), possibly for some other metals in the dust too. For ultrapure water treatment, the solubility ratios for Mn, Co, and Ni between the dust and the aerosol are significantly higher than V, Al, Fe, and Ti, suggesting the differentiated effects of transport processes on forming the readily soluble metal compounds in the dust.

On the other hand, the ratios of buffer and Berger leaches exhibit an increasing trend with elemental sequence from Cd to Ti, increasing with the litho-tendency and varying from around 1 to 35. The relatively low ratios observed in the Cd, Zn, and Mn were mainly attributed to highly enhanced solubilities caused by the buffer and Berger leaches for both the aerosols and the dust. For Co, Ni, V, Al, Fe, and Ti, the ratios of buffer and Berger leaches generally increase with the tendency. The deviations of the three ratios for Ti, the element with the highest litho-tendency, were down to be the same order of magnitude, which were 86, 17, and 33 for ultrapure water, buffer, and Berger treatments, respectively. In brief, the convergent patterns of the three ratios with the tendency reflect the coupling effects of the transport processes on the aerosols of a specific element under the leaching protocol (numerator) and the soluble behavior of any specific element in the dust under the leaching protocol (denominator). The converging tendencies and highly elevated ratios indicate that the transport processes enhance the solubilities of all elements under all leaching protocols and the enhancement extent is litho-tendency associated. In the other words, the transport impacts on the aerosols are element specific, which are partially attributed to the contribution of anthropogenic aerosol metals in the aerosols and partially attributed to the readiness of the metal composition in the aerosols to be solubilized during atmospheric transport processes.

2.4.3 Element specific deposition velocity and flux

Since both the solubilities and mass fractions are significantly different among different elements in size-fractionated aerosols (Fig. 2.2), the authentic deposition velocity of dissolvable aerosol metals shall be element specific. The accurate estimate of deposition flux for the dissolvable metals would thus require the information of the soluble mass among different sizes and their corresponding deposition velocities. For example, the deposition velocities of Fe for 5 size cut-offs vary up to 2 orders of magnitude, which are 0.008, 0.018, 0.063, 0.39, and 0.94 cm s^{-1} in the East China Sea, respectively (Hsieh et al., 2022). In addition to the importance of aerosol sizes, deposition velocity is also closely associated with aerosol density and atmospheric conditions, which are mainly decided by wind speed, relative humidity, and sea surface temperature (Slinn and Slinn, 1980).

Considering the velocities of each size fraction, we have calculated the deposition velocities of individual element for each size with ultrapure water, buffer, Berger, and total digestion treatments (Table 2.1). We have also calculated the deposition velocities for fine, coarse, and size-fractionated (5-size) aerosols based on the solubility and mass fraction data obtained in this study (Table 2.1). Using Cd as an example in anthropogenic type elements (Cd, Zn, Pb), due to its comparable mass fractions and high solubilities in all size fractions, the deposition velocities of Cd for same size aerosols are highly comparable among the four leaching or digestion treatments, which are 0.16, 0.16, 0.16, and 0.19 cm s^{-1}, respectively. Similarly, the velocities are 0.21, 0.27, 0.28, and 0.33 cm s^{-1} for Zn, and 0.10, 0.18, 0.20, and 0.25 cm s^{-1} for Pb, respectively. The relatively low velocity of the ultrapure water treatment (0.10 cm s^{-1}) for Pb is attributed to its low percentage of coarse fraction (9.5 %). On the other hand, the solubilities of lithogenic type elements vary dramatically among different size aerosols, particularly in coarse particles. Using Fe as an example, the relative mass fractions were 59, 21, 10, 7.4, 2.8 %; 32, 17, 13, 18, 20 %; 11, 14, 17, 27, 31 %; and 3.6, 6.8, 13, 33, 44 % for the four protocols, respectively. The mass fractions result in the deposition velocities to be 0.10, 0.38, 0.57, and 0.76 cm s^{-1} for the 4 treatments, respectively (Table 2.1). Similarly, the velocities are 0.10, 0.33, 0.59, and 0.69 cm s-1 for Al and 0.16, 0.49, 0.63, and 0.80 cm s^{-1} for Ti, respectively. The deviation of the 4 velocities for V is the highest among all elements, which are 0.04, 0.08, 0.21, and 0.49 cm s^{-1}, respectively, mainly attributed to its low percentage in coarse fraction for the ultrapure water and buffer treatments. Attributed to the high deviations among elements and the treatments, it is thus essential to obtain the soluble mass fraction information of size-fractionated aerosols for the accurate estimate of deposition velocities for individual element. The four velocities for both Mn and Co range

doi:10.6342/NTU202302200

from 0.42 to 0.63 cm s^{-1}, which are generally between the value of anthropogenic and lithogenic type elements (Table 2.1). Due to the comparable mass fractions among the four treatments, the deviations of the velocities are relatively small among the treatments, which are 0.42, 0.46, 0.50, and 0.58 cm s^{-1} for Mn and 0.43, 0.48, 0.60, and 0.63 cm s^{-1} for Co, respectively. The velocities for Ni are 0.15, 0.21, 0.29, and 0.43 cm s^{-1}, respectively. The relative contribution between anthropogenic and lithogenic aerosols in each size may differ spatially and result in region specific velocities for each element. Comparable studies in the adjacent regions of this study are needed to validate whether the deposition velocities reported in this study may represent the Northwestern Pacific Ocean. We suggest that more studies as what we have carried out in the ECS are also needed to obtain the spatially specific deposition velocities in other major oceanic regions.

Thus, without knowing the mass fraction information by different leaching treatments, the metal flux estimates from total suspended aerosols would overestimate the fluxes for all elements, except Cd. We have evaluated the bias of the deposition fluxes of dissolvable aerosol metals among three different size categories, 5 sizes, two sizes (fine and coarse), and 1 size (total) by using the following calculation.

$$F_{dry} = \sum_{i=1}^{5} C_i \times V_{d\_i} \quad (\text{or } C_F \times V_F + C_C \times V_C \text{ or } C_{TSP} \times V_{TSP})$$

The term, C_i, C_F, C_C, and C_{TSP} refer to the metal concentration of each leaching treatment in each size fraction. And V_{d_i}, V_F, V_C, and V_{TSP} represent the dry deposition velocities of each size range. Figure 2.6 exhibits the variations and the deviations of the dry deposition fluxes by five different leaching and digestion protocols for the size-fractionated aerosols (Table S2.10-2.13). The extremely high deposition velocity in coarse aerosols is the major factor deciding the distribution patterns of the fluxes in size-fractionated aerosols. Overall, the fluxes of all elements increased with aerosol sizes even for the elements (e.g., Cd, Zn, and Pb) with relatively high concentrations in fine aerosols (Fig. 2.2). Using Cd as an example, the percentages of total Cd mass decreased with sizes, from 41 to 8.8 % for the finest to coarsest aerosols but the total fluxes increased from 2.1 to 61 %, respectively. The contribution of coarse aerosols to the total fluxes for all other elements are even higher. For V, Al, Fe, and Ti, the coarsest aerosol accounts for 63, 82, 82, and 89 % in instant ultrapure water fluxes; 83, 95, 96, and 97 % in buffer fluxes; 93, 98, 97, and 98 % for Berger fluxes 97, 98, 99, and 99 % in total fluxes, respectively (Table S2.10-2.13).

Previous oceanic studies on estimating the deposition fluxes of aerosol soluble metals are mainly based on total aerosol mass information. However, as shown in Table 2.1, the dissolvable fractions of different sizes vary significantly under different leaching protocols. We have estimated the offset or bias of the deposition fluxes between using the velocities obtained from one-size (total) or two-sizes (fine and coarse) and the velocities obtained from 5-size in this study (Table 2.1; Fig. 2.7). The percentage of bias of ultrapure water metal fluxes are 54, 40, 48, 174, 180, 1266, 581, 682, 408 % for Zn, Mn, Co, Pb, Ni, V, Al, Fe, and Ti, respectively (Fig. 2.7). The metals Pb, Ni, V, Al, Fe, and Ti have higher offsets for buffer metal fluxes estimates with bias to be 42, 100, 485, 111, 102, and 65 %, respectively. The mass fraction of Berger leach is similar to the total treatment so only Ni and V have high offsets for flux estimates, with bias to be 39 and 123%, respectively. After the correction by multiple size aerosol collection mentioned above, two aerosol size sampling may significantly reduce the bias, with bias all within 50 % for all leaching treatments and almost all elements with offset under 10 % for buffer and Berger treatments (Fig. 2.7).

Although we did not collect wet deposition samples, it should be noted that wet deposition is important in our studied region. We have carried out a preliminary estimate on the wet deposition fluxes by using the proposed equation (Duce et al., 1991). The results are shown in Figure S2.2.

2.4.4 The implication to aerosol Fe flux estimate by models in the global ocean

The model accuracy for estimating global aerosol dissolvable metal fluxes to the ocean relies on the applicability of aerosol metal solubilities chosen in models. Although most of the global models, i.e., CAM4, GEOS-Chem, IMPACT, TM4-ECPL, have already considered the differences of the deposition velocities of multiple aerosol sizes (2-4 size bins) (Myriokefalitakis et al., 2018), the solubilities applied in those models did not clearly distinguish or consider the implications of the different solubilities obtained by the leaching treatments as shown in this study. The solubilities of aerosol metals can vary significantly and the variations are specific in aerosol sizes, leaching methods, and elements, especially for lithogenic type elements. For example, the ratios of dissolvable Fe concentrations (or solubility) by normalizing to ultrapure water leach for the three leaching treatment in bulk aerosols are 1: 1.6: 5.8, showing limited solubility difference between ultrapure water and buffer treatments (Table S2.5-S2.7). However, the ratios in aerosol size 7.3 μm increased dramatically, with the ratios to be 1: 12: 64. Using long term seawater leaching or adding sufficient organic ligand approaches to lithogenic dusts, some recent laboratory studies also reported relatively high aerosol metal solubilities (Fig. 2.8). The solubilities of Fe and Al in many of these studies were comparable to the solubility levels observed by buffer and Berger leaches in this study (Fig. 2.8). For the model estimates of global aerosol dissolvable Fe fluxes, we argue that the solubilities obtained by buffer and Berger leaches are more realistic to represent aerosol Fe solubility in the ocean than the value obtained by ultrapure water leach.

2.5 Conclusion

This study demonstrates that solubilities obtained by different leaching treatments are highly varied for different metals in coarse aerosols. Thus, the impacts of transport processes on aerosol metal solubility and deposition velocities are element-specific. As shown in Figure 2.5, the transport processes enhance the solubilities of all elements under all leaching protocols and the enhancement extent increases with litho-tendency. Based on the data of size specific solubilities and masses obtained in this study (Table 2.1, last column), the average deposition velocities varied significantly among different elements, ranging from a few folds to one order of magnitude, which are 0.04-0.43, 0.08-0.49, 0.20-0.63, and 0.19-0.80 cm s^{-1} for ultrapure water, buffer, Berger, and total leaching treatments, respectively (Table 2.1). However, while separating the size-fractionated aerosols to two fractions (fine and coarse), the velocities are relatively constrained either for fine or coarse size aerosols (Table 2.1), in which the velocities are 0.013-0.030, 0.015-0.033, 0.018-0.037, and 0.022-0.047 among the elements for fine fraction; and 0.73-0.90, 0.84-0.98, 0.90-1.0, and 0.92-1.0 cm s^{-1} for coarse fraction, respectively. Due to extremely low deposition velocities of fine aerosol, the effects of the deviation of the fine aerosol velocities for total flux estimate would be further reduced. In brief, two-size aerosol sampling provides a much more reliable flux estimate for aerosol metal deposition than total suspended particle sampling. Without knowing the metal mass fraction in multiple size-fractionated aerosols, one may use two-size deposition velocities to obtain more accurate estimates for aerosol metal fluxes. Since it is highly challenging to obtain sufficient multiple size aerosols onboard due to cruise time limitation and low aerosol mass over the open ocean, for related studies in other major oceanic regions, we suggest to carry out multiple size-fractionated aerosol sampling on an islet as this study first to obtain

doi:10.6342/NTU202302200

the value of region specific deposition velocities for flux estimates. In terms of solubility applied to global model flux estimates, we think that ultrapure water leach underestimates the aerosol solubility of V, Al, Fe, and Ti in the surface water of the ECS. The buffer and Berger leaches are more realistic to represent the metal solubility in the ocean.

doi:10.6342/NTU202302200

2.6 References

ATSDR, 1999. Toxicological profile for cadmium. U.S. Department of Health and Human Services. Public Health Service. Agency for Toxic Substances and Disease Registry.

Baker, A.R. and Jickells, T.D., 2006. Mineral particle size as a control on aerosol iron solubility. Geophysical Research Letters, 33(17) DOI: 10.1029/2006gl026557.

Baker, A.R., Jickells, T.D., Witt, M. and Linge, K.L., 2006. Trends in the solubility of iron, aluminium, manganese and phosphorus in aerosol collected over the Atlantic Ocean. Marine Chemistry, 98(1): 43-58 DOI: 10.1016/j.marchem.2005.06.004.

Baker, A.R. et al., 2021. Changing atmospheric acidity as a modulator of nutrient deposition and ocean biogeochemistry. Sci Adv, 7(28) DOI: 10.1126/sciadv.abd8800.

Baker, A.R. et al., 2016. Trace element and isotope deposition across the air-sea interface: progress and research needs. Philos Trans A Math Phys Eng Sci, 374(2081) DOI: 10.1098/rsta.2016.0190.

Berger, C.J.M., Lippiatt, S.M., Lawrence, M.G. and Bruland, K.W., 2008. Application of a chemical leach technique for estimating labile particulate aluminum, iron, and manganese in the Columbia River plume and coastal waters off Oregon and Washington. Journal of Geophysical Research, 113 DOI: 10.1029/2007jc004703.

Bonnet, S. and Guieu, C., 2004. Dissolution of atmospheric iron in seawater. Geophysical Research Letters, 31(3) DOI: 10.1029/2003gl018423.

Buck, C.S., Landing, W.M., Resing, J.A. and Lebon, G.T., 2006. Aerosol iron and aluminum solubility in the northwest Pacific Ocean: Results from the 2002 IOC cruise. Geochemistry, Geophysics, Geosystems, 7(4) DOI: 10.1029/2005gc000977.

Chen, C.C. et al., 2022. Nickel superoxide dismutase protects nitrogen fixation in

Trichodesmium. Limnology and Oceanography Letters, 7(4): 363-371 DOI: 10.1002/lol2.10263.

Cheng, M.-C., You, C.-F., Cao, J. and Jin, Z., 2012. Spatial and seasonal variability of water-soluble ions in PM2.5 aerosols in 14 major cities in China. Atmospheric Environment, 60: 182-192 DOI: 10.1016/j.atmosenv.2012.06.037.

Clough, R., Lohan, M.C., Ussher, S.J., Nimmo, M. and Worsfold, P.J., 2019. Uncertainty associated with the leaching of aerosol filters for the determination of metals in aerosol particulate matter using collision/reaction cell ICP-MS detection. Talanta, 199: 425-430 DOI: 10.1016/j.talanta.2019.02.067.

Cutter, G. et al., 2017. Sampling and Sample-handling Protocols for GEOTRACES Cruises. 3 DOI: 10.25607/OBP-2.

Duce, R.A. et al., 1991. The atmospheric input of trace species to the world ocean. Global

Biogeochemical Cycles, 5(3): 193-259 DOI: 10.1029/91gb01778.

Eggimann, D.W. and Betzer, P.R., 1976. Decomposition and Analysis of Refractory Oceanic Suspended Materials. Analytical Chemistry, 48(6): 886-890 DOI: DOI 10.1021/ac60370a005.

Félix-Bermúdez, A., Delgadillo-Hinojosa, F., Torres-Delgado, E.V. and Muñoz-Barbosa, A., 2020. Does Sea Surface Temperature Affect Solubility of Iron in Mineral Dust? The Gulf of California as a Case Study. Journal of Geophysical Research: Oceans, 125(9) DOI: 10.1029/2019jc015999.

Fishwick, M.P. et al., 2014. The impact of changing surface ocean conditions on the dissolution of aerosol iron. Global Biogeochemical Cycles, 28(11): 1235-1250 DOI: 10.1002/2014gb004921.

Fishwick, M.P. et al., 2018. Impact of surface ocean conditions and aerosol provenance on the dissolution of aerosol manganese, cobalt, nickel and lead in seawater. Marine Chemistry, 198: 28-43 DOI: 10.1016/j.marchem.2017.11.003.

Foret, G., Bergametti, G., Dulac, F. and Menut, L., 2006. An optimized particle size bin scheme for modeling mineral dust aerosol. Journal of Geophysical Research, 111(D17) DOI: 10.1029/2005jd006797.

Gunchin, G., Osan, J., Migliori, A., Shagjjamba, D. and Streli, C., 2021. Chromium and Zinc Speciation in Airborne Particulate Matter Collected in Ulaanbaatar, Mongolia, by X-Ray Absorption Near-edge Structure Spectroscopy. Aerosol and Air Quality Research, 21(8) DOI: 10.4209/aaqr.210018.

Ho, T.Y. et al., 2003. The elemental composition of some marine phytoplankton. Journal of Phycology, 39(6): 1145-1159 DOI: DOI 10.1111/j.0022-3646.2003.03-090.x.

Hsieh, C.-C., Chen, H.-Y. and Ho, T.-Y., 2022. The effect of aerosol size on Fe solubility and deposition flux: A case study in the East China Sea. Marine Chemistry, 241 DOI: 10.1016/j.marchem.2022.104106.

Hu, Z.C. and Gao, S., 2008. Upper crustal abundances of trace elements: A revision and update. Chemical Geology, 253(3-4): 205-221 DOI: 10.1016/j.chemgeo.2008.05.010.

Jickells, T.D. et al., 2005. Global iron connections between desert dust, ocean biogeochemistry, and climate. Science, 308(5718): 67-71 DOI: 10.1126/science.1105959.

Jickells, T.D., Baker, A.R. and Chance, R., 2016. Atmospheric transport of trace elements and nutrients to the oceans. Philos Trans A Math Phys Eng Sci, 374(2081) DOI: 10.1098/rsta.2015.0286.

Kessler, N., Kraemer, S.M., Shaked, Y. and Schenkeveld, W.D.C., 2020. Investigation of Siderophore-Promoted and Reductive Dissolution of Dust in Marine Microenvironments Such as Trichodesmium Colonies. Frontiers in Marine Science, 7 DOI: 10.3389/fmars.2020.00045.

Li, R. et al., 2023. Evaluating the effects of contact time and leaching solution on measured solubilities of aerosol trace metals. Applied Geochemistry, 148 DOI: 10.1016/j.apgeochem.2022.105551.

Li, W. et al., 2017. Air pollution-aerosol interactions produce more bioavailable iron for ocean ecosystems. Sci Adv, 3(3): e1601749 DOI: 10.1126/sciadv.1601749.

Longo, A.F. et al., 2016. Influence of Atmospheric Processes on the Solubility and Composition of Iron in Saharan Dust. Environ Sci Technol, 50(13): 6912-20 DOI: 10.1021/acs.est.6b02605.

Mackey, K.R., Chien, C.T., Post, A.F., Saito, M.A. and Paytan, A., 2015. Rapid and gradual modes of aerosol trace metal dissolution in seawater. Front Microbiol, 5: 794 DOI: 10.3389/fmicb.2014.00794.

Mahowald, N.M. et al., 2005. Atmospheric global dust cycle and iron inputs to the ocean. Global Biogeochemical Cycles, 19(4): n/a-n/a DOI: 10.1029/2004gb002402.

Martin, J.H. and Fitzwater, S.E., 1988. Iron deficiency limits phytoplankton growth in the north-east Pacific subarctic. Nature, 331(6154): 341-343 DOI: 10.1038/331341a0.

Meskhidze, N. et al., 2019. Perspective on identifying and characterizing the processes controlling iron speciation and residence time at the atmosphere-ocean interface. Marine Chemistry, 217 DOI: 10.1016/j.marchem.2019.103704.

Morel, F.M.M., Lam, P.J. and Saito, M.A., 2020. Trace Metal Substitution in Marine Phytoplankton. Annual Review of Earth and Planetary Sciences, 48(1): 491-517 DOI: 10.1146/annurev-earth-053018-060108.

Morton, P.L. et al., 2013. Methods for the sampling and analysis of marine aerosols: results from the 2008 GEOTRACES aerosol intercalibration experiment. Limnology and Oceanography: Methods, 11(2): 62-78 DOI: 10.4319/lom.2013.11.62.

Myriokefalitakis, S. et al., 2018. Reviews and syntheses: the GESAMP atmospheric iron deposition model intercomparison study. Biogeosciences, 15(21): 6659-6684 DOI: 10.5194/bg-15-6659-2018.

Nicholls, G.D., 1963. Environmental Studies in Sedimentary Geochemistry. Science Progress, 51(201): 12-31

Ohta, A. et al., 2006. Chemical compositions and XANES speciations of Fe, Mn and Zn from aerosols collected in China and Japan during dust events. Geochemical Journal, 40(4): 363-376 DOI: 10.2343/geochemj.40.363.

Paytan, A. et al., 2009. Toxicity of atmospheric aerosols on marine phytoplankton. Proceedings of the National Academy of Sciences of the United States of America, 106(12): 4601-4605 DOI: 10.1073/pnas.0811486106.

Perron, M.M.G. et al., 2020. Assessment of leaching protocols to determine the solubility of trace metals in aerosols. Talanta, 208: 120377 DOI: 10.1016/j.talanta.2019.120377.

Raiswell, R. and Canfield, D.E., 2012. The Iron Biogeochemical Cycle Past and Present. Geochemical Perspectives, 1(1): 1-220 DOI: 10.7185/geochempersp.1.1.

Sakata, K. et al., 2022. Iron (Fe) speciation in size-fractionated aerosol particles in the Pacific Ocean: The role of organic complexation of Fe with humic-like substances in controlling Fe solubility. Atmos. Chem. Phys., 22(14): 9461-9482 DOI: 10.5194/acp-22-9461-2022.

Sakata, K. et al., 2014. Identification of sources of lead in the atmosphere by chemical speciation using X-ray absorption near-edge structure (XANES) spectroscopy. Journal of Environmental Sciences, 26(2): 343-352 DOI: 10.1016/s1001-0742(13)60430-1.

Sakata, K., Sakaguchi, A., Yokoyama, Y., Terada, Y. and Takahashi, Y., 2017. Lead speciation studies on coarse and fine aerosol particles by bulk and micro X-ray absorption fine structure spectroscopy. Geochemical Journal, 51(3): 215-225 DOI: 10.2343/geochemj.2.0456.

Sarthou, G. et al., 2003. Atmospheric iron deposition and sea-surface dissolved iron concentrations in the eastern Atlantic Ocean. Deep Sea Research Part I: Oceanographic Research Papers, 50(10-11): 1339-1352 DOI: 10.1016/s0967-0637(03)00126-2.

Seinfeld, J.H. and Pandis, S.N., 2016. Atmospheric Chemistry And Physics: From Air Pollution to Climate Change. (Wiley-interscience, ed. 3, 2016): 1326

Shelley, R.U., Landing, W.M., Ussher, S.J., Planquette, H. and Sarthou, G., 2018. Regional trends in the fractional solubility of Fe and other metals from North Atlantic aerosols (GEOTRACES cruises GA01 and GA03) following a two-stage leach. Biogeosciences, 15(7): 2271-2288 DOI: 10.5194/bg-15-2271-2018.

Shelley, R.U., Morton, P.L. and Landing, W.M., 2015. Elemental ratios and enrichment factors in aerosols from the US-GEOTRACES North Atlantic transects. Deep Sea Research Part II: Topical Studies in Oceanography, 116: 262-272 DOI: 10.1016/j.dsr2.2014.12.005.

Shi, Z.B. et al., 2012. Impacts on iron solubility in the mineral dust by processes in the source region and the atmosphere: A review. Aeolian Research, 5: 21-42 DOI: 10.1016/j.aeolia.2012.03.001.

Slinn, S.A. and Slinn, W.G.N., 1980. Predictions for particle deposition on natural waters. Atmospheric Environment (1967), 14(9): 1013-1016 DOI: 10.1016/0004-6981(80)90032-3.

Takahashi, Y., Higashi, M., Furukawa, T. and Mitsunobu, S., 2011. Change of iron species and iron solubility in Asian dust during the long-range transport from western China to Japan. Atmospheric Chemistry and Physics, 11(21): 11237-11252 DOI: 10.5194/acp-11-11237-2011.

Wang, B.-S. and Ho, T.-Y., 2020. Aerosol Fe cycling in the surface water of the Northwestern Pacific ocean. Progress in Oceanography, 183 DOI: 10.1016/j.pocean.2020.102291.

Hsin-Yen Wu, Chih-Chiang Hsieh, Tung-Yuan Ho,Trace metal dissolution kinetics of East

Asian size-fractionated aerosols in seawater: The effect of a model siderophore, Marine Chemistry, 2023, 104277, ISSN 0304-4203, DOI:10.1016/j.marchem.2023.104277.

2.7 Figures

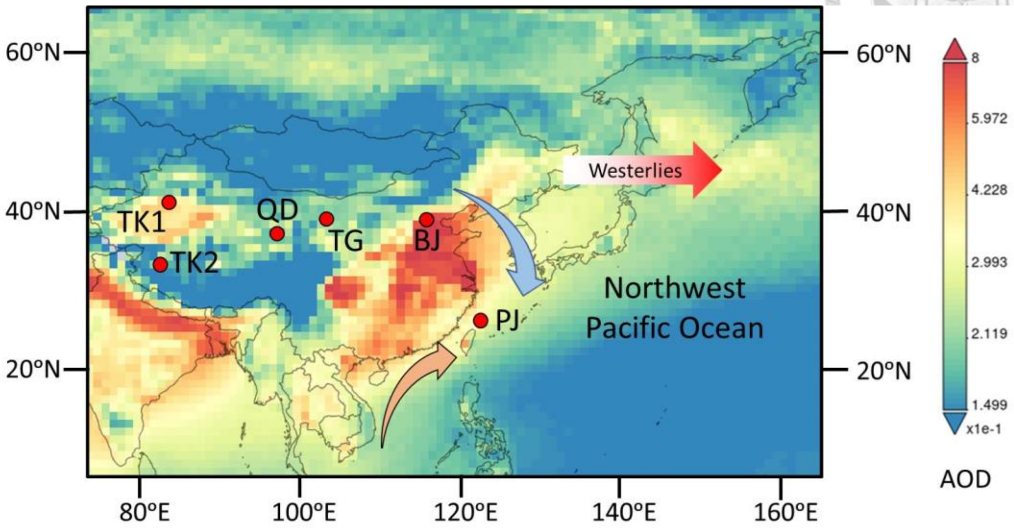

Figure 2.1. The location of aerosol and dessert dust sampling sites of this study with aerosol optical depth as background. The annual averaged data of aerosol optical depth (2002-2022) are obtained by NASA Giovanni software (https://giovanni.gsfc.nasa.gov/giovanni/). The abbreviated letters, PJ, BJ, TK1, TK2, TG, and QD, stand for the sampling stations of aerosol samples or desert dust at Penjia islet, Beijing (NIES CRM No. 28), Taklimakan Desert, Taklimakan Desert, Tengger Desert, and Qaidam Desert, respectively.

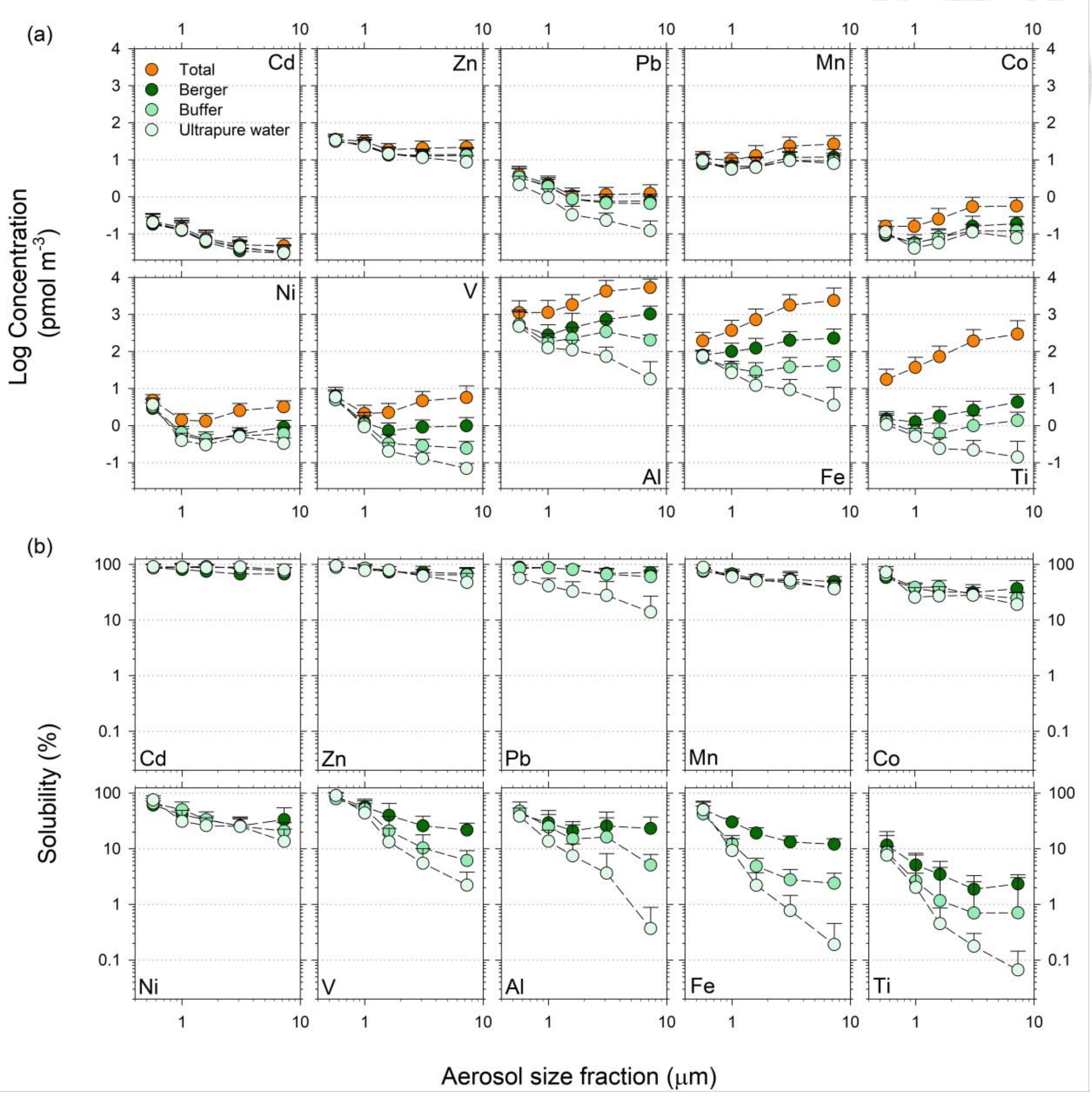

Figure 2.2. The averaged elemental (a) concentrations and (b) solubilities obtained by ultrapure water, buffer, Berger and total digestion treatments in the size-fractionated aerosols collected at PJ. Light green, green, dark green and orange stand for the data of ultrapure water, buffer, Berger and total digestion treatments, respectively. Error bars stand for one standard deviation of all monthly data during the sampling period.

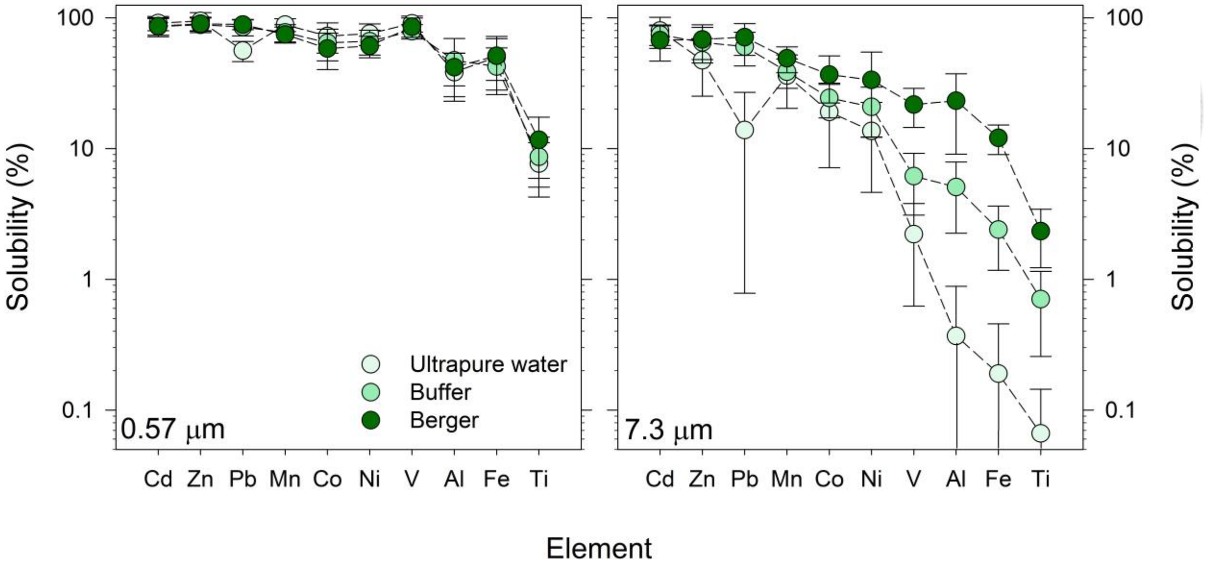

Figure 2.3. The comparison of the elemental solubilities obtained by ultrapure water, buffer, and Berger treatments with the size cut-offs of 0.57 and 7.3 μm.

doi:10.6342/NTU202302200

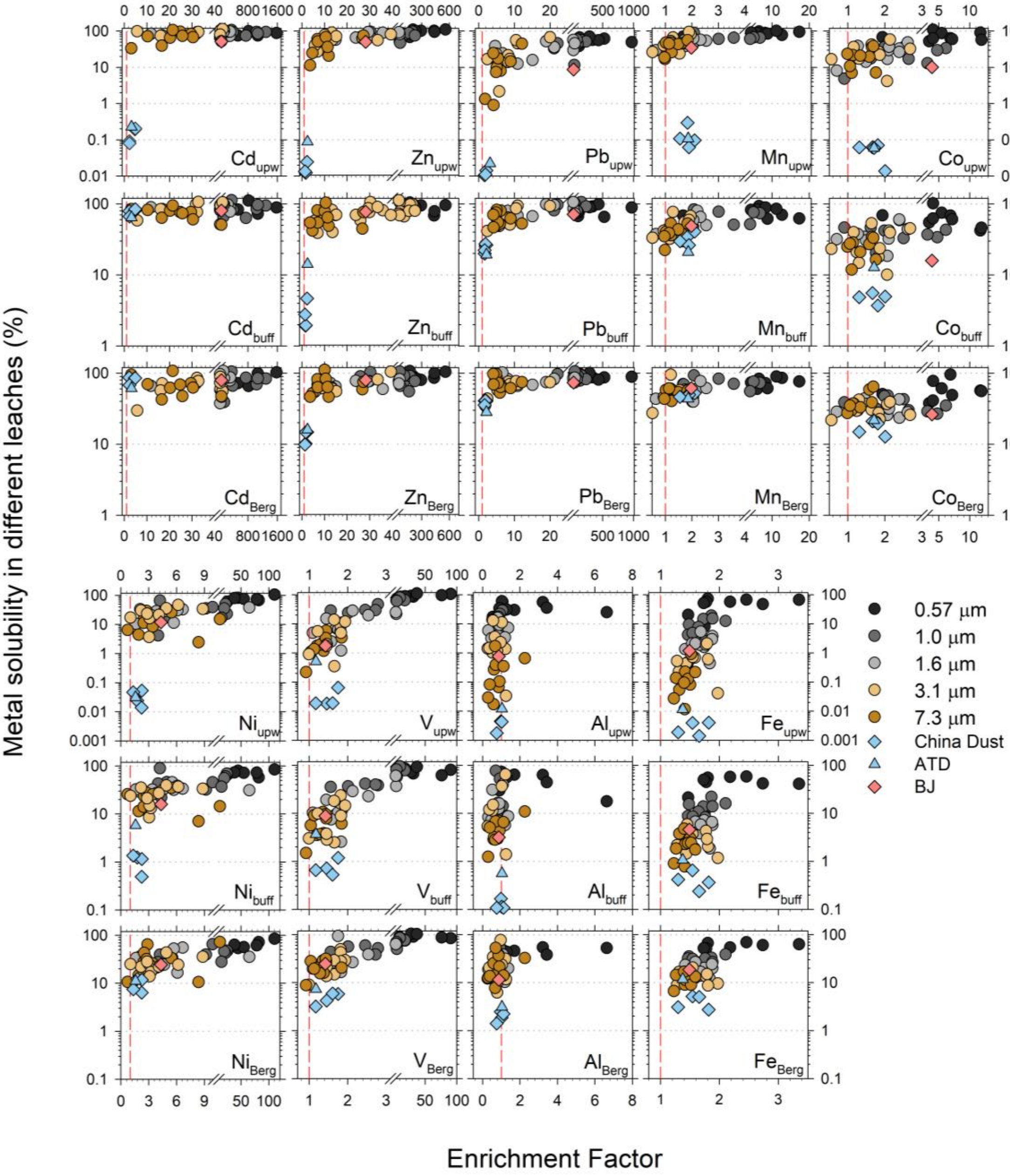

Figure 2.4. The comparison of enrichment factors (EF) and the metal solubilities of size-fractionated aerosols and dust. The circle symbols stand for PJ aerosol samples, blue diamond for Chinese desert dust (China Dust), blue triangle for Arizona Test Dust (ATD), and red diamond for NIES CRM No. 28 Urban aerosols collected in Beijing (BJ). The numbers shown right next to the circle symbols are the size cut-offs of PJ aerosol samples. The three panels for each element stand for the results obtained by the three leaching methods, ultrapure water (upw), buffer (buff), and Berger leaches, respectively.

doi:10.6342/NTU202302200

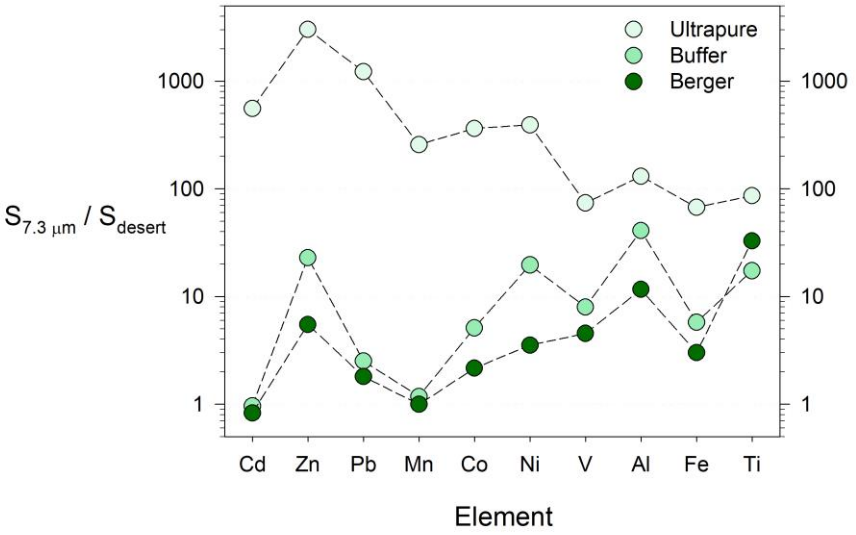

Figure 2.5. The variation patterns of the solubility ratios between the aerosols (7.3 μm) to the Chinese dust for the three leaching treatments.

doi:10.6342/NTU202302200

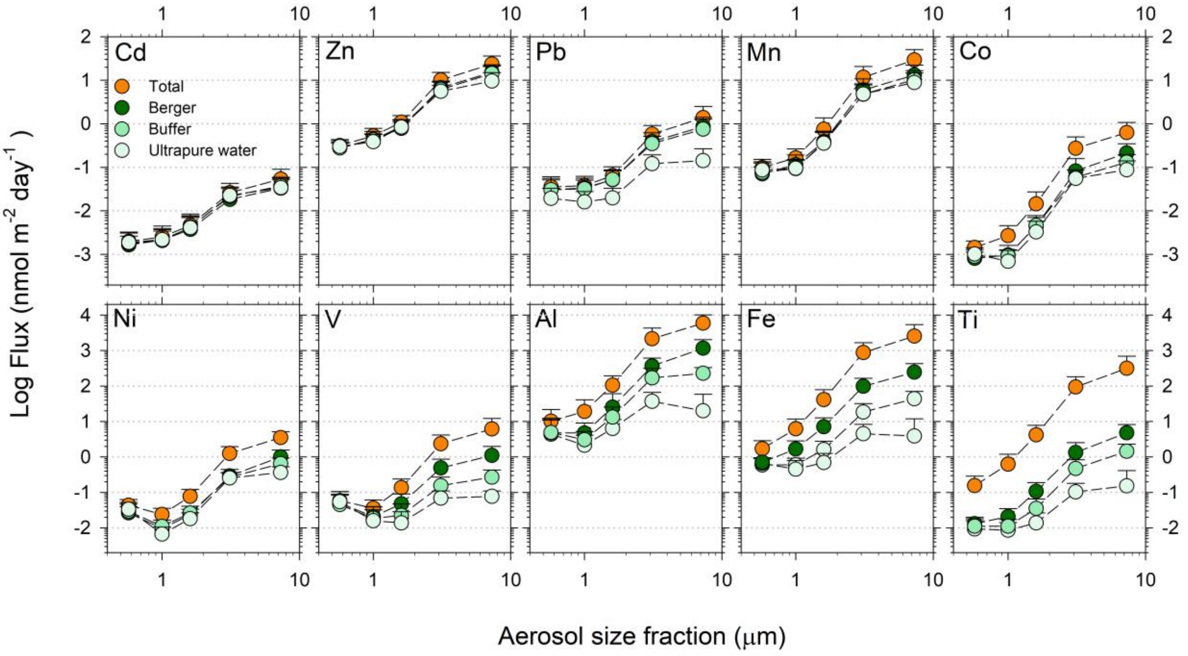

Figure 2.6. The comparison of the averaged dry deposition fluxes estimated from the data obtained by ultrapure water, buffer, Berger, and total digestion treatments of the size-fractionated aerosol metals.

doi:10.6342/NTU202302200

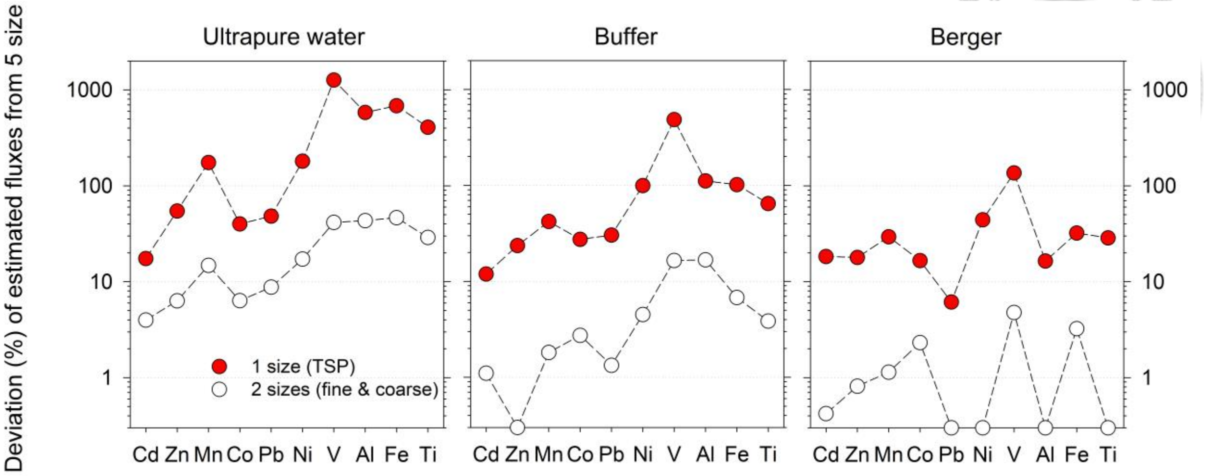

Figure 2.7. The offset (or bias) of the deposition velocities obtained with one-size sampling (total suspended particles, TSP) with red circle symbol or with two-size sampling (fine & coarse) with open circle symbol to the velocities obtained by 5-size aerosol sampling for flux calculation.

doi:10.6342/NTU202302200

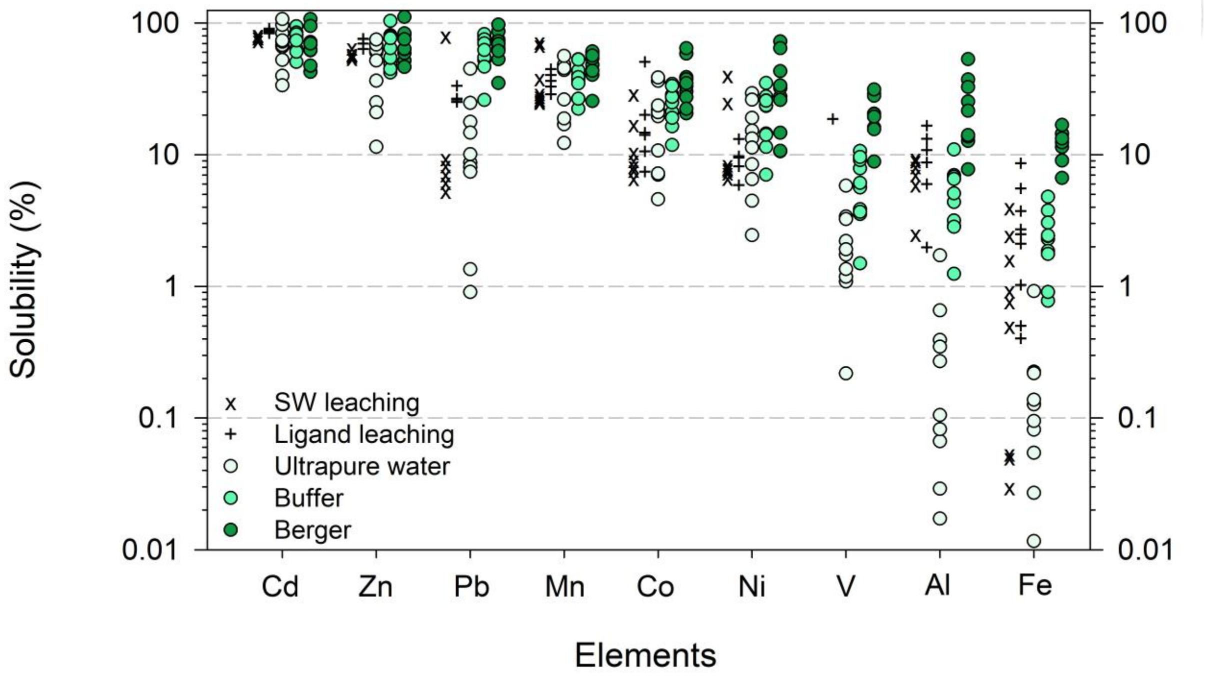

Figure 2.8. The comparison of the solubilities obtained from ultrapure water, buffer, Berger leaching of the largest aerosols collected in PJ with seawater solubilities obtained in previous studies (Bonnet and Guieu, 2004; Félix-Bermúdez et al., 2020; Fishwick et al., 2014; Fishwick et al., 2018; Mackey et al., 2015) or by ligand leaching (Clough et al., 2019; Kessler et al., 2020).

2.8 Tables

Table 2.1. The mass fraction of the 5 size-fractionated aerosols and the averaged deposition velocities estimated by using fine, coarse, or 5-size aerosols collected in this study.

Element	Fraction	Elemental mass fraction (w/w, %) Size cut-offs (μm)					Average deposition velocity (cm s^{-1})		
		0.57	1.0	1.6	3.1	7.3	Fine	Coarse	5-size*
Cd	Ultrapure water	43	27	14	9.3	6.5	0.023	0.87	0.16
	Buffer	42	27	15	8.9	7.2	0.024	0.89	0.16
	Berger	42	29	14	8.1	6.9	0.023	0.90	0.16
	Total	41	27	14	9.4	8.8	0.023	0.92	0.19
Zn	Ultrapure water	37	25	16	13	9.5	0.025	0.88	0.21
	Buffer	32	26	15	13	14	0.026	0.94	0.27
	Berger	32	27	14	14	14	0.025	0.94	0.28
	Total	28	25	15	16	17	0.027	0.94	0.33
Pb	Ultrapure water	57	25	8.8	6.2	3.3	0.019	0.83	0.10
	Buffer	45	25	12	9.1	8.8	0.022	0.93	0.18
	Berger	43	26	11	10	10	0.021	0.93	0.20
	Total	41	23	11	12	13	0.022	0.94	0.25
Mn	Ultrapure water	25	14	16	25	20	0.030	0.90	0.42
	Buffer	22	14	16	24	24	0.032	0.93	0.46
	Berger	17	15	15	26	26	0.032	0.93	0.50
	Total	13	12	15	28	32	0.036	0.95	0.58
Co	Ultrapure water	28	10	14	28	19	0.028	0.87	0.43
	Buffer	21	12	17	25	25	0.033	0.93	0.48
	Berger	16	10	13	28	33	0.033	0.96	0.60
	Total	10	9.5	15	32	34	0.039	0.94	0.63
Ni	Ultrapure water	71	7.6	5.8	10	6.3	0.015	0.86	0.15
	Buffer	60	12	7.9	10	11	0.018	0.95	0.21
	Berger	54	11	7.4	11	17	0.018	1.0	0.29
	Total	36	11	10	19	24	0.022	0.97	0.43
V	Ultrapure water	82	13	2.8	1.8	1.0	0.013	0.83	0.04
	Buffer	72	16	4.8	4.2	3.5	0.015	0.90	0.08
	Berger	59	13	7.8	10	11	0.018	0.94	0.21
	Total	30	10	11	22	27	0.025	0.96	0.49
Al	Ultrapure water	59	16	14	9.1	2.3	0.021	0.73	0.10
	Buffer	36	12	15	23	14	0.026	0.84	0.33
	Berger	17	9.3	15	24	34	0.034	0.99	0.59
	Total	8.2	8.3	13	31	39	0.039	0.97	0.69
Fe	Ultrapure water	59	21	10	7.4	2.8	0.019	0.78	0.10
	Buffer	32	17	13	18	20	0.026	0.94	0.38
	Berger	11	14	17	27	31	0.037	0.95	0.57
	Total	3.6	6.8	13	33	44	0.046	0.98	0.76
Ti	Ultrapure water	49	24	11	10	6.4	0.021	0.86	0.16
	Buffer	26	14	12	20	28	0.027	0.98	0.49
	Berger	13	11	16	23	38	0.036	1.0	0.63
	Total	2.9	6.0	12	31	48	0.047	1.0	0.80

*The averaged velocity is obtained by size specific solubility and mass from the 5-size fractions obtained in this study. Same approach is applied to the fine and coarse fractions.

doi:10.6342/NTU202302200

2.9 Supplementary

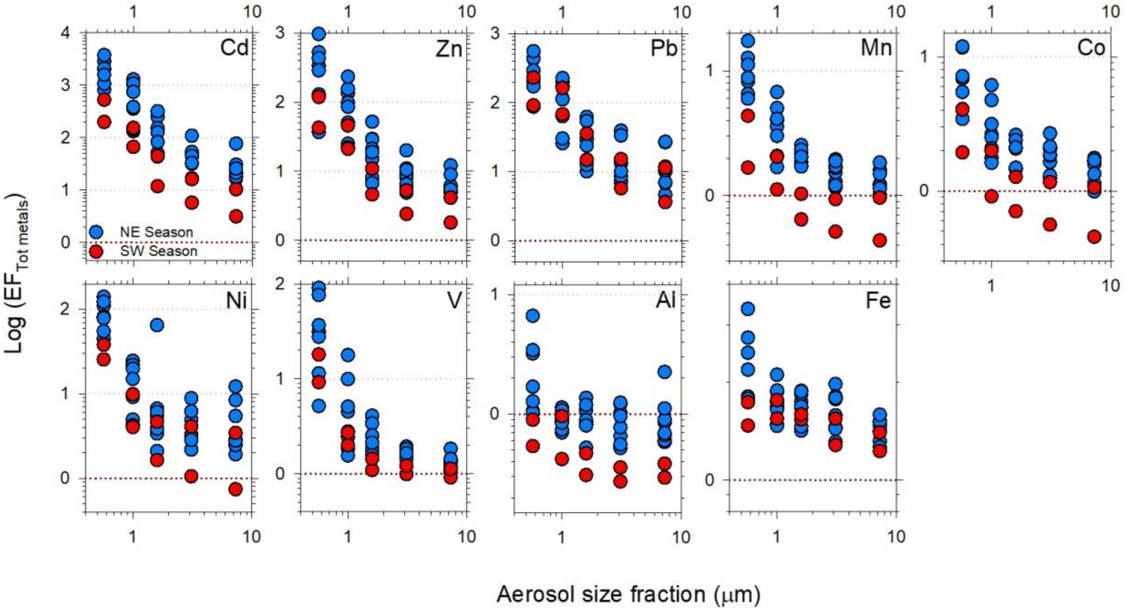

Figure S2.1. The seasonal variations of EF of the size-fractionated aerosol metals. The blue and red symbols stand for the data obtained from Northeastern and Southwestern monsoon seasons, respectively.

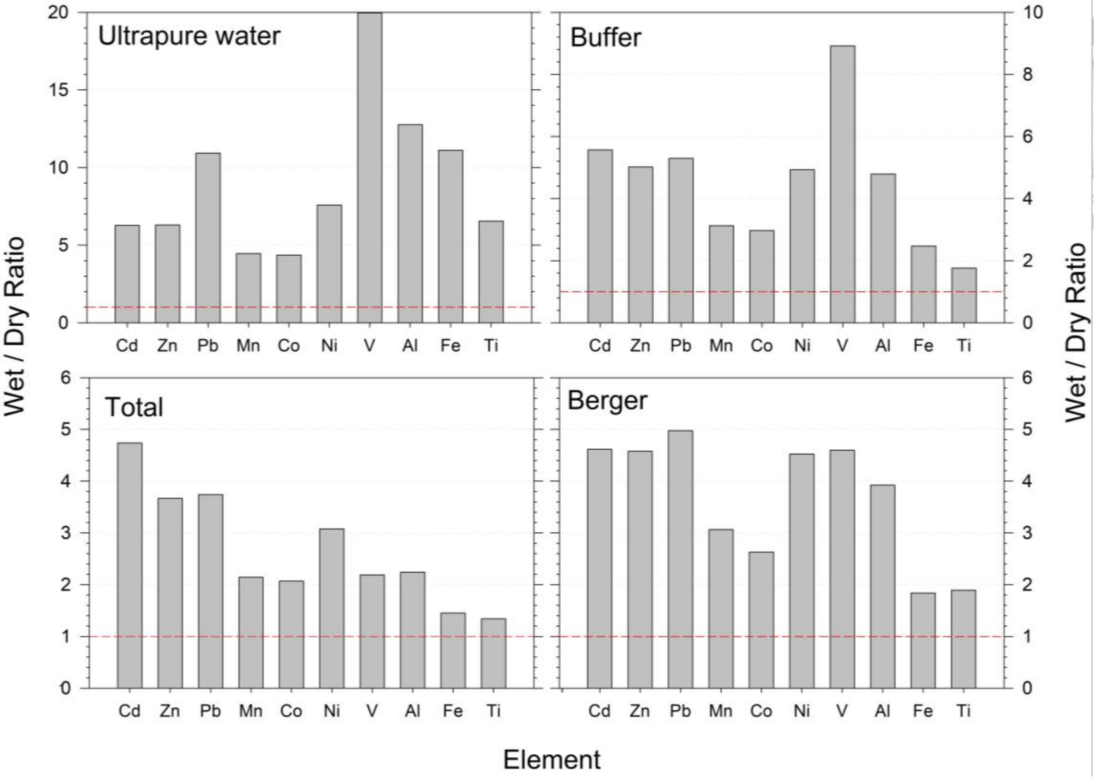

Figure S2.2. The ratios of wet to dry deposition ratios of aerosol metals estimated by ultrapure water, buffer, Berger, and total treatments. The contribution of wet deposition on aerosol metal fluxes is significant in our region, where precipitation is high. The wet to dry ratios of the deposition fluxes ranged from 1.3 to 2.2 for lithogenic type elements and from 3.1 to 4.7 for anthropogenic type elements. The wet deposition fluxes were calculated by following equation: $F_{wet} = P \times S \times C_{air} \times \rho^{-1}$, where P is the precipitation rate (mm yr^{-1}, data source https://e-service.cwb.gov.tw/HistoryDataQuery/index.jsp), S is the scavenging ratio for aerosols ($<PM_3 = 200$, $>PM_3 = 1{,}000$), C_{air} is the metal concentration of aerosols in the air (µg m^{-3}), and ρ is the density of air (1,200 g m^{-3}).

Table S2.1. The elemental background concentrations in filter blank obtained by using ultrapure water, buffer, Berger, and total digestion treatments.

Protocols	n	Blank concentration (nmol per filter)*									
		Al	Ti	V	Mn	Fe	Co	Ni	Zn	Pb	Cd
Ultrapure	3	4.3	0.092	0.012	0.10	0.30	0.006	0.024	0.15	0.003	0.001
Buffer	5	12	0.16	0.030	0.025	0.19	0.006	0.006	1.6	0.017	0.001
Berger	4	6.8	0.14	0.021	0.038	1.5	0.036	0.85	0.39	0.003	0.002
Total	5	60	1.9	0.20	0.57	3.0	0.11	1.2	0.51	0.034	0.039

* The filters were not put in the sampler with the pump off.

Table S2.2. The comparison of total elemental concentrations obtained in the Chinese desert dust and two reference materials, Arizona Test Dust (ATD) and NIES CRM No. 28 Urban Aerosols (BJ), with a previous study (Shelley et al. 2015) or the certified value.

Sample	n	Concentration (ng g^{-1})										Reference
		Al	Ti	V	Mn	Fe	Co	Ni	Zn	Cd	Pb	
Acid blank (ng/vial)	6	10 (1)	0.32 (0.10)	0.057 (0.012)	0.13 (0.07)	1.5 (0.3)	0.029 (0.004)	0.34 (0.03)	0.17 (0.08)	0.11 (0.03)	0.18 (0.06)	This Study
ATD	5	69,600 (1,870)	3,220 (50)	72.7 (1.1)	764 (12)	33,600 (500)	n.a.*	n.a.	n.a.	n.a.	n.a.	Shelley et al., 2015
	9	66,800 (4,750)	3,280 (250)	74.4 (8.5)	700 (50)	32,500 (2380)	20.6 (5.5)	37.0 (7.1)	126 (13)	0.27 (0.01)	32.3 (4.1)	This study
TK1	3	55973 (359)	2914 (34)	80.4 (0.5)	647 (4)	31266 (146)	12.6 (0.2)	31.7 (0.9)	71.7 (1.8)	0.18 (0.02)	22.8 (0.2)	This study
TK2	3	56952 (1179)	2837 (3)	94.2 (1.4)	720 (6)	35895 (822)	14.8 (0.6)	39.3 (1.0)	97.9 (1.9)	0.36 (0.01)	28.3 (0.6)	This study
TG	3	56940 (694)	2593 (47)	79.0 (1.3)	593 (12)	29875 (814)	12.2 (0.4)	36.2 (2.3)	68.8 (1.0)	0.34 (0.04)	22.9 (0.5)	This study
QD	3	49866 (1988)	3357 (295)	74.5 (3.8)	630 (47)	30323 (2390)	11.4 (0.5)	28.0 (2.1)	70.5 (1.5)	0.21 (0.06)	25.5 (2.5)	This study
BJ	6	46,400 (1,890)	2,730 (125)	73.7 (4.5)	653 (27)	28,315 (1240)	27.5 (2.2)	72.9 (4.9)	1157 (51)	5.7 (0.8)	397 (16)	This study
Certified Value		50,400 (1,000)	2,920 (330)	73.2 (7.0)	686 (42)	29,200 (1700)	22.0	63.8 (3.4)	1140 (100)	5.60 (0.43)	403 (32)	
Accuracy[+]		92%	93%	101%	95%	97%	125%	114%	102%	98%	99%	

*n.a.: data are not available. The numbers in all of the brackets shown are monthly averaged value.

[+] The percentage presented is obtained by dividing our measured value to the certified value for each element.

Table S2.3. The deviations of the aerosol elemental concentrations obtained by leaching and total digested treatments.

Element	Size (μm)	Average concentration (pmol m^{-3})				RSD (%)	Avg RSD (%)
		Total	Berger	Buffer	Ultrapure water		
Cd	0.57	0.22	0.18	0.20	0.21	7.8	13
	1.0	0.15	0.13	0.12	0.13	8.6	
	1.6	0.074	0.060	0.068	0.067	8.8	
	3.1	0.051	0.035	0.041	0.044	16	
	7.3	0.047	0.030	0.033	0.031	23	
Zn	0.57	36	31	31	34	6.5	20
	1.0	32	26	26	23	13	
	1.6	19	13	15	14	15	
	3.1	21	14	12	12	28	
	7.3	22	14	13	8.7	38	
Pb	0.57	3.9	3.4	3.4	2.1	24	43
	1.0	2.2	2.0	1.9	0.95	32	
	1.6	1.1	0.86	0.87	0.33	41	
	3.1	1.1	0.76	0.68	0.23	53	
	7.3	1.2	0.77	0.66	0.12	65	
Mn	0.57	11	7.8	8.5	9.6	15	39
	1.0	9.7	6.8	5.5	5.6	28	
	1.6	13	6.7	6.5	6.2	40	
	3.1	23	12	9.5	9.6	49	
	7.3	26	12	9.4	7.9	61	
Co	0.57	0.16	0.091	0.10	0.11	27	71
	1.0	0.16	0.058	0.055	0.041	70	
	1.6	0.25	0.077	0.081	0.058	77	
	3.1	0.54	0.16	0.12	0.11	88	
	7.3	0.57	0.19	0.12	0.079	94	
Ni	0.57	4.8	2.9	3.3	3.7	23	72
	1.0	1.4	0.56	0.65	0.40	60	
	1.6	1.3	0.39	0.43	0.30	77	
	3.1	2.5	0.59	0.53	0.51	96	
	7.3	3.2	0.91	0.60	0.33	105	
V	0.57	6.4	5.5	5.0	5.9	11	91
	1.0	2.1	1.2	1.1	0.93	40	
	1.6	2.2	0.73	0.33	0.20	107	
	3.1	4.7	0.91	0.29	0.13	143	
	7.3	5.7	0.98	0.24	0.070	152	
Al	0.57	1120	514	531	474	47	115
	1.0	1133	278	179	125	111	
	1.6	1819	440	226	110	122	
	3.1	4229	730	343	73	145	
	7.3	5335	1025	203	18	152	

Element	Size (μm)	Average concentration (pmol m^{-3})				RSD (%)	Avg RSD
		Total	Berger	Buffer	Ultrapure water		
Fe	0.57	194	80	67	74	58	135
	1.0	368	100	36	27	121	
	1.6	721	123	28	12	152	
	3.1	1780	200	38	9.3	168	
	7.3	2368	228	42	3.6	173	
Ti	0.57	18	1.5	1.3	1.1	152	183
	1.0	37	1.3	0.67	0.51	184	
	1.6	73	1.8	0.61	0.24	191	
	3.1	192	2.6	0.99	0.22	195	
	7.3	295	4.3	1.4	0.14	195	

Table S2.4. The monthly total concentrations of different elements in the size-fractionated aerosols.

Element	Size (μm)	Concentration (pmol m^{-3})												Avg	SD
		2019				2020									
		Sep	Oct	Nov	Dec	Jan	Feb	Mar	Apr	May	Jun	Jul	Aug		
Cd	0.57	0.24	n.a.	n.a.	0.19	0.33	0.34	0.47	n.a.	0.12	0.11	0.074	0.088	0.22	0.14
	1.0	0.20	n.a.	n.a.	0.13	0.17	0.17	0.44	0.17	0.044	0.051	0.026	0.063	0.15	0.12
	1.6	0.12	n.a.	n.a.	0.043	0.079	0.11	0.18	0.062	0.028	0.026	0.020	0.027	0.070	0.053
	3.1	0.067	n.a.	n.a.	0.027	0.040	0.061	0.11	0.091	0.021	0.044	0.027	0.018	0.051	0.032
	7.3	0.088	n.a.	n.a.	0.029	0.037	0.052	0.062	0.10	0.012	0.047	0.024	0.021	0.047	0.029
Zn	0.57	25	n.a.	n.a.	28	37	35	64	n.a.	19	51	31	30	36	14
	1.0	21	n.a.	n.a.	20	27	32	63	30	8.9	51	27	36	32	16
	1.6	11	n.a.	n.a.	9.0	15	21	33	11	7.7	31	15	17	17	9
	3.1	9.9	n.a.	n.a.	6.4	14	24	34	24	6.4	43	25	18	20	12
	7.3	24	n.a.	n.a.	16	12	12	24	23	5.8	53	26	22	22	13
Pb	0.57	3.8	n.a.	n.a.	3.3	7.8	1.4	9.2	n.a.	1.4	2.3	1.5	1.5	3.9	2.8
	1.0	2.4	n.a.	n.a.	1.5	3.5	3.0	5.4	2.3	0.63	1.5	0.74	1.3	2.2	1.4
	1.6	1.1	n.a.	n.a.	0.46	1.2	1.7	2.3	0.69	0.40	0.94	0.45	0.57	1.1	0.7
	3.1	1.1	n.a.	n.a.	0.51	0.69	1.9	2.1	1.7	0.30	1.7	0.83	0.53	1.1	0.7
	7.3	2.9	n.a.	n.a.	0.82	0.54	0.83	1.1	1.7	0.22	2.5	0.92	0.69	1.2	0.9
Mn	0.57	7.4	n.a.	n.a.	11	10	23	17	n.a.	9.2	8.9	5.6	5.8	11	6
	1.0	7.1	n.a.	n.a.	6.4	7.4	20	19	14	5.9	8.0	3.3	6.2	9.7	5.9
	1.6	6.2	n.a.	n.a.	3.5	5.9	41	20	11	10	13	4.3	6.1	12	11
	3.1	15	n.a.	n.a.	6.0	6.7	51	40	46	7.3	37	15	9.5	23	18
	7.3	48	n.a.	n.a.	16	7.1	17	28	46	6.0	61	21	14	26	19
Co	0.57	0.092	n.a.	n.a.	0.15	0.19	0.27	0.23	n.a.	0.14	0.21	0.10	0.074	0.16	0.07
	1.0	0.093	n.a.	n.a.	0.12	0.14	0.42	0.27	0.15	0.12	0.13	0.064	0.10	0.16	0.11
	1.6	0.10	n.a.	n.a.	0.076	0.12	0.84	0.46	0.22	0.18	0.29	0.11	0.13	0.25	0.24
	3.1	0.32	n.a.	n.a.	0.15	0.18	1.4	0.87	0.99	0.16	0.80	0.37	0.22	0.54	0.43
	7.3	1.1	n.a.	n.a.	0.47	0.15	0.52	0.53	0.82	0.10	1.3	0.47	0.26	0.57	0.39

*n.a.: data are not available.

Element	Size (μm)	Concentration (pmol m^{-3})												Avg	SD
		2019				2020									
		Sep	Oct	Nov	Dec	Jan	Feb	Mar	Apr	May	Jun	Jul	Aug		
Ni	0.57	6.0	n.a.	n.a.	4.1	4.7	8.2	5.5	n.a.	4.1	6.5	2.3	1.9	4.8	2.0
	1.0	2.1	n.a.	n.a.	1.0	1.4	2.5	2.4	1.1	0.57	1.4	0.75	1.1	1.4	0.7
	1.6	0.95	n.a.	n.a.	4.9	0.74	3.3	2.0	1.2	0.59	1.6	0.92	0.87	1.7	1.4
	3.1	1.3	n.a.	n.a.	1.1	1.4	4.9	3.7	3.9	0.83	3.6	3.1	1.5	2.5	1.4
	7.3	4.5	n.a.	n.a.	5.3	2.6	2.2	2.8	3.6	0.69	4.9	3.6	2.0	3.2	1.4
V	0.57	17	n.a.	n.a.	7.9	4.2	3.4	4.0	n.a.	4.9	8.3	3.9	3.2	6.4	4.5
	1.0	5.3	n.a.	n.a.	1.6	1.1	3.8	2.6	1.2	1.2	2.4	0.73	1.3	2.1	1.4
	1.6	2.5	n.a.	n.a.	0.91	1.0	6.2	3.1	1.3	1.6	3.7	1.0	1.1	2.2	1.7
	3.1	4.0	n.a.	n.a.	1.4	1.1	9.4	5.8	6.5	1.9	12	3.2	1.4	4.7	3.7
	7.3	8.6	n.a.	n.a.	3.0	1.4	3.8	4.7	6.6	1.3	22	4.2	1.8	5.7	6.1
Al	0.57	398	n.a.	n.a.	346	1763	4103	719	n.a.	1190	955	383	220	1120	1224
	1.0	411	n.a.	n.a.	330	448	4516	1572	1116	1007	995	508	426	1133	1256
	1.6	970	n.a.	n.a.	568	1050	5748	3239	1804	1575	2075	643	518	1819	1617
	3.1	2227	n.a.	n.a.	1874	1167	13841	5154	6809	1949	6468	1866	934	4229	4021
	7.3	9514	n.a.	n.a.	3742	3300	4884	4641	6809	1205	13644	2794	2820	5335	3740
Fe	0.57	115	n.a.	n.a.	117	124	381	259	n.a.	105	443	126	72	194	135
	1.0	148	n.a.	n.a.	112	155	1139	529	421	235	623	159	161	368	325
	1.6	287	n.a.	n.a.	157	246	2099	1033	482	489	1758	371	284	721	685
	3.1	958	n.a.	n.a.	381	344	3736	2122	2707	496	5169	1372	511	1780	1647
	7.3	3914	n.a.	n.a.	985	354	1388	1922	2633	374	9694	1733	685	2368	2798
Ti	0.57	11	n.a.	n.a.	5.8	7.6	36	20	n.a.	10	51	12	4.9	18	16
	1.0	17	n.a.	n.a.	9.0	14	114	51	43	27	68	15	14	37	33
	1.6	34	n.a.	n.a.	15	22	192	104	43	56	192	39	28	73	67
	3.1	123	n.a.	n.a.	44	33	318	225	251	58	676	149	48	192	197
	7.3	465	n.a.	n.a.	125	42	155	220	291	50	1324	208	72	295	384

*n.a.: data are not available.

Table S2.5. The monthly concentrations of different elements in size-fractionated aerosols treated by Berger leach.

Element	Size (μm)	Concentration (pmol m^{-3})												Avg	SD
		2019				2020									
		Sep	Oct	Nov	Dec	Jan	Feb	Mar	Apr	May	Jun	Jul	Aug		
Cd	0.57	0.21	n.a.	n.a.	0.16	0.29	0.22	0.38	n.a.	0.12	0.11	0.053	0.091	0.18	0.10
	1.0	0.14	n.a.	n.a.	0.11	0.14	0.17	0.38	0.18	0.053	0.045	0.010	0.042	0.13	0.11
	1.6	0.095	n.a.	n.a.	0.037	0.069	0.064	0.15	0.12	0.027	0.017	0.007	0.012	0.060	0.049
	3.1	0.059	n.a.	n.a.	0.016	0.022	0.043	0.083	0.065	0.018	0.013	0.016	0.014	0.035	0.026
	7.3	0.037	n.a.	n.a.	0.018	0.017	0.037	0.043	0.063	0.013	0.045	0.017	0.010	0.030	0.017
Zn	0.57	22	n.a.	n.a.	24	37	27	51	n.a.	20	41	26	31	31	10
	1.0	16	n.a.	n.a.	17	24	29	58	31	9.2	33	15	28	26	14
	1.6	8.6	n.a.	n.a.	7.0	12	14	25	20	5.6	20	9.2	12	13	6
	3.1	6.1	n.a.	n.a.	5.2	15	17	20	15	7.1	23	14	14	14	6
	7.3	12	n.a.	n.a.	7.6	7.3	9.6	27	14	4.8	25	17	16	14	7
Pb	0.57	3.3	n.a.	n.a.	2.9	7.0	3.3	7.4	n.a.	1.3	2.2	1.3	1.5	3.4	2.3
	1.0	1.9	n.a.	n.a.	1.4	2.8	2.8	5.0	2.4	0.83	1.2	0.54	1.1	2.0	1.3
	1.6	0.86	n.a.	n.a.	0.39	1.0	1.4	1.9	1.2	0.40	0.72	0.30	0.42	0.86	0.52
	3.1	0.81	n.a.	n.a.	0.35	0.51	1.4	1.5	1.1	0.26	0.75	0.48	0.41	0.76	0.44
	7.3	1.6	n.a.	n.a.	0.52	0.40	0.72	1.1	1.2	0.21	0.89	0.63	0.42	0.77	0.42
Mn	0.57	6.1	n.a.	n.a.	8.1	8.7	14	12	n.a.	5.6	6.2	4.1	5.6	7.8	3.3
	1.0	4.3	n.a.	n.a.	4.6	5.6	14	14	11	5.4	3.9	1.5	3.5	6.8	4.5
	1.6	3.6	n.a.	n.a.	2.1	3.6	16	12	14	5.3	5.7	1.9	2.4	6.7	5.4
	3.1	8.2	n.a.	n.a.	3.1	3.4	29	20	24	7.0	10	6.8	5.4	12	9
	7.3	21	n.a.	n.a.	6.6	3.4	9.6	17	25	3.6	16	9.1	7.9	12	7
Co	0.57	0.071	n.a.	n.a.	0.082	0.11	0.10	0.14	n.a.	0.14	0.10	0.043	0.037	0.091	0.037
	1.0	0.028	n.a.	n.a.	0.041	0.037	0.13	0.12	0.056	0.057	0.050	0.030	0.028	0.058	0.038
	1.6	0.046	n.a.	n.a.	0.018	0.034	0.22	0.15	0.093	0.065	0.082	0.032	0.040	0.077	0.061
	3.1	0.094	n.a.	n.a.	0.046	0.048	0.51	0.24	0.22	0.067	0.17	0.14	0.085	0.16	0.14
	7.3	0.33	n.a.	n.a.	0.10	0.057	0.30	0.20	0.27	0.028	0.28	0.16	0.17	0.19	0.11

*n.a.: data are not available.

doi:10.6342/NTU202302200

Element	Size (μm)	Concentration (pmol m^{-3})												Avg	SD
		2019				2020									
		Sep	Oct	Nov	Dec	Jan	Feb	Mar	Apr	May	Jun	Jul	Aug		
Ni	0.57	5.0	n.a.	n.a.	2.2	2.5	4.4	3.1	n.a.	3.0	3.1	1.5	1.2	2.9	1.2
	1.0	0.99	n.a.	n.a.	0.42	0.64	0.79	0.94	0.45	0.23	0.38	0.49	0.30	0.56	0.27
	1.6	0.32	n.a.	n.a.	0.35	0.41	0.67	0.42	0.65	0.21	0.53	0.22	0.14	0.39	0.18
	3.1	0.30	n.a.	n.a.	0.48	0.52	1.21	0.63	0.55	0.23	0.89	0.69	0.36	0.59	0.29
	7.3	0.66	n.a.	n.a.	0.56	1.9	1.4	1.2	0.99	0.22	0.53	0.93	0.67	0.91	0.49
V	0.57	15	n.a.	n.a.	7.0	3.8	2.0	3.0	n.a.	5.1	7.5	3.0	3.3	5.5	3.9
	1.0	4.1	n.a.	n.a.	1.3	0.79	1.2	1.3	0.52	0.69	1.4	0.28	0.66	1.2	1.1
	1.6	1.6	n.a.	n.a.	0.58	0.39	1.0	0.74	1.3	0.40	0.73	0.26	0.29	0.73	0.45
	3.1	2.0	n.a.	n.a.	0.61	0.33	1.4	1.3	0.89	0.52	1.1	0.68	0.41	0.91	0.51
	7.3	2.4	n.a.	n.a.	0.88	0.28	0.61	1.0	1.0	0.36	1.9	0.81	0.58	0.98	0.68
Al	0.57	192	n.a.	n.a.	159	926	2233	252	n.a.	456	145	165	97	514	694
	1.0	163	n.a.	n.a.	120	242	918	485	237	166	211	85	151	278	250
	1.6	182	n.a.	n.a.	219	208	2208	636	186	162	390	114	90	440	642
	3.1	518	n.a.	n.a.	588	273	1635	880	424	1500	785	381	320	730	483
	7.3	2408	n.a.	n.a.	1392	1076	1053	646	527	640	1733	383	396	1025	658
Fe	0.57	77	n.a.	n.a.	74	75	66	140	n.a.	54	116	65	50	80	29
	1.0	52	n.a.	n.a.	44	51	234	144	110	75	194	50	43	100	69
	1.6	67	n.a.	n.a.	32	49	253	144	116	70	351	99	47	123	103
	3.1	160	n.a.	n.a.	60	46	358	263	236	58	459	282	77	200	143
	7.3	354	n.a.	n.a.	142	40	172	255	237	54	645	292	91	228	179
Ti	0.57	1.5	n.a.	n.a.	0.56	0.88	1.1	1.2	n.a.	1.9	3.5	2.0	0.92	1.5	0.9
	1.0	1.4	n.a.	n.a.	0.73	0.60	0.81	1.4	0.76	0.67	3.7	1.5	1.1	1.3	0.9
	1.6	1.9	n.a.	n.a.	0.65	0.33	1.3	1.0	3.0	1.4	4.9	3.0	0.6	1.8	1.4
	3.1	5.6	n.a.	n.a.	1.6	0.63	2.5	2.7	1.7	0.92	5.3	4.7	0.23	2.6	2.0
	7.3	9.7	n.a.	n.a.	4.5	1.7	3.9	5.5	2.6	0.86	6.5	6.0	1.8	4.3	2.7

*n.a.: data are not available.

Table S2.6. The monthly concentrations of different elements in size-fractionated aerosols treated by buffer leach.

Element	Size (μm)	Concentration (pmol m^{-3})												Avg	SD
		2019				2020									
		Sep	Oct	Nov	Dec	Jan	Feb	Mar	Apr	May	Jun	Jul	Aug		
Cd	0.57	0.22	n.a.	n.a.	0.13	0.24	0.38	0.47	n.a.	0.088	0.10	0.061	0.078	0.20	0.15
	1.0	0.17	n.a.	n.a.	0.12	0.16	0.11	0.28	0.20	0.062	0.049	0.025	0.052	0.12	0.08
	1.6	0.11	n.a.	n.a.	0.042	0.062	0.089	0.18	0.11	0.023	0.023	0.019	0.027	0.068	0.052
	3.1	0.059	n.a.	n.a.	0.025	0.042	0.051	0.059	0.090	0.016	0.026	0.023	0.019	0.041	0.024
	7.3	0.056	n.a.	n.a.	0.023	0.019	0.040	0.047	0.061	0.011	0.040	0.020	0.016	0.033	0.018
Zn	0.57	24	n.a.	n.a.	19	29	29	61	n.a.	20	43	28	29	31	13
	1.0	18	n.a.	n.a.	19	26	19	42	32	9.4	39	22	29	26	10
	1.6	8.5	n.a.	n.a.	6.5	10	17	29	18	5.5	22	12	19	15	7
	3.1	6.0	n.a.	n.a.	6.9	10	9.4	13	16	4.2	25	17	16	12	6
	7.3	10	n.a.	n.a.	8.0	5.5	9.5	19	12	6.0	29	17	17	13	7
Pb	0.57	3.5	n.a.	n.a.	2.1	7.0	2.8	9.1	n.a.	1.3	2.2	1.2	1.4	3.4	2.8
	1.0	2.1	n.a.	n.a.	1.6	3.2	1.9	4.2	2.3	0.83	1.2	0.65	1.0	1.9	1.1
	1.6	0.90	n.a.	n.a.	0.49	0.89	1.3	2.2	1.1	0.27	0.62	0.31	0.56	0.87	0.59
	3.1	0.69	n.a.	n.a.	0.48	0.64	0.94	1.1	1.2	0.19	0.72	0.42	0.46	0.68	0.31
	7.3	1.5	n.a.	n.a.	0.66	0.28	0.68	0.86	0.92	0.15	0.66	0.43	0.43	0.66	0.39
Mn	0.57	6.8	n.a.	n.a.	6.6	7.1	19	15	n.a.	5.7	6.1	4.6	5.3	8.5	5.1
	1.0	4.2	n.a.	n.a.	4.7	5.6	7.4	9.8	11	4.9	3.6	1.5	3.2	5.5	2.9
	1.6	3.0	n.a.	n.a.	2.8	2.9	17	12	12	4.8	4.9	1.8	3.6	6.5	5.2
	3.1	4.8	n.a.	n.a.	4.6	4.5	17	12	25	2.7	12	6.2	5.7	9.5	7.2
	7.3	11	n.a.	n.a.	5.9	2.7	6.7	15	20	2.3	16	7.3	7.4	9.4	5.9
Co	0.57	0.094	n.a.	n.a.	0.061	0.088	0.15	0.17	n.a.	0.10	0.14	0.065	0.045	0.10	0.04
	1.0	0.041	n.a.	n.a.	0.050	0.047	0.086	0.089	0.068	0.047	0.060	0.027	0.035	0.055	0.021
	1.6	0.036	n.a.	n.a.	0.045	0.053	0.15	0.15	0.13	0.054	0.091	0.040	0.053	0.081	0.047
	3.1	0.068	n.a.	n.a.	0.081	0.083	0.14	0.16	0.23	0.024	0.19	0.15	0.085	0.12	0.06
	7.3	0.13	n.a.	n.a.	0.077	0.050	0.14	0.15	0.17	0.026	0.24	0.13	0.086	0.12	0.06

*n.a.: data are not available.

doi:10.6342/NTU202302200

Element	Size	Concentration (pmol m^{-3})												Avg	SD
		2019				2020									
	(μm)	Sep	Oct	Nov	Dec	Jan	Feb	Mar	Apr	May	Jun	Jul	Aug		
Ni	0.57	5.0	n.a.	n.a.	1.9	2.1	6.5	4.0	n.a.	2.4	4.3	1.7	1.4	3.3	1.8
	1.0	1.4	n.a.	n.a.	0.60	0.77	0.55	0.76	0.49	0.51	0.59	0.34	0.40	0.65	0.31
	1.6	0.43	n.a.	n.a.	0.31	0.25	1.1	0.54	0.40	0.17	0.51	0.31	0.33	0.43	0.25
	3.1	0.48	n.a.	n.a.	0.43	0.49	0.41	0.49	0.59	0.17	0.86	0.84	0.55	0.53	0.20
	7.3	0.51	n.a.	n.a.	0.37	0.37	0.53	0.66	0.51	0.19	1.3	0.92	0.70	0.60	0.31
V	0.57	14	n.a.	n.a.	4.9	2.9	2.6	3.6	n.a.	3.6	6.6	3.4	3.0	5.0	3.6
	1.0	4.2	n.a.	n.a.	1.5	0.92	0.45	0.99	0.42	0.49	0.89	0.29	0.76	1.1	1.1
	1.6	0.91	n.a.	n.a.	0.55	0.23	0.16	0.30	0.14	0.12	0.38	0.19	0.31	0.33	0.24
	3.1	0.64	n.a.	n.a.	0.34	0.16	0.23	0.17	0.24	0.17	0.36	0.32	0.25	0.29	0.14
	7.3	0.48	n.a.	n.a.	0.32	0.08	0.15	0.17	0.24	0.10	0.32	0.38	0.18	0.24	0.13
Al	0.57	258	n.a.	n.a.	221	315	2583	520	n.a.	529	114	116	124	531	786
	1.0	318	n.a.	n.a.	127	237	419	256	103	144	93	29	59	179	125
	1.6	160	n.a.	n.a.	229	91	728	519	102	47	175	47	161	226	223
	3.1	254	n.a.	n.a.	1213	431	193	290	202	131	349	225	140	343	319
	7.3	274	n.a.	n.a.	261	361	213	147	193	82	170	142	184	203	79
Fe	0.57	64	n.a.	n.a.	48	52	40	149	n.a.	47	95	63	42	67	35
	1.0	23	n.a.	n.a.	18	34	51	73	46	21	53	13	22	36	20
	1.6	12	n.a.	n.a.	11	14	39	40	32	9.5	82	25	16	28	22
	3.1	21	n.a.	n.a.	22	15	44	39	55	7.2	112	52	15	38	31
	7.3	30	n.a.	n.a.	37	8.1	42	46	64	6.9	88	83	12	42	29
Ti	0.57	1.3	n.a.	n.a.	0.38	0.57	1.5	1.6	n.a.	0.59	3.1	1.6	0.67	1.3	0.9
	1.0	0.65	n.a.	n.a.	0.28	0.63	0.58	0.97	0.69	0.14	1.6	0.53	0.62	0.67	0.40
	1.6	0.46	n.a.	n.a.	0.36	0.18	0.56	0.56	0.47	0.064	2.0	1.1	0.34	0.61	0.55
	3.1	0.79	n.a.	n.a.	0.75	0.36	0.76	0.86	1.07	0.12	3.0	2.0	0.24	1.0	0.9
	7.3	1.4	n.a.	n.a.	1.5	0.30	1.5	1.3	1.79	0.20	2.0	3.3	0.33	1.4	0.9

*n.a.: data are not available.

Table S2.7. The monthly concentrations of different elements in size-fractionated aerosols treated by superpure water leach.

Element	Size (μm)	Concentration (pmol m^{-3})												Avg	SD
		2019				2020									
		Sep	Oct	Nov	Dec	Jan	Feb	Mar	Apr	May	Jun	Jul	Aug		
Cd	0.57	0.27	n.a.	n.a.	0.20	0.30	0.34	0.42	n.a.	0.092	0.10	0.056	0.078	0.21	0.13
	1.0	0.19	n.a.	n.a.	0.12	0.15	0.13	0.33	0.19	0.064	0.037	0.022	0.059	0.13	0.09
	1.6	0.089	n.a.	n.a.	0.041	0.077	0.088	0.19	0.10	0.019	0.022	0.014	0.028	0.067	0.054
	3.1	0.054	n.a.	n.a.	0.028	0.046	0.046	0.091	0.075	0.020	0.044	0.020	0.017	0.044	0.025
	7.3	0.035	n.a.	n.a.	0.019	0.019	0.043	0.060	0.068	0.013	0.016	0.018	0.016	0.031	0.020
Zn	0.57	27	n.a.	n.a.	29	35	26	66		13	44	31	33	34	15
	1.0	17	n.a.	n.a.	19	23	22	51	16	8.6	24	24	27	23	11
	1.6	8.4	n.a.	n.a.	8.1	13	14	32	17	5.1	18	14	16	14	7
	3.1	5.3	n.a.	n.a.	7.6	12	6.6	19	14	5.0	17	18	10	12	5
	7.3	6.0	n.a.	n.a.	3.4	7.7	7.0	15	12	3.9	6.1	9.5	16	8.7	4.4
Pb	0.57	2.2	n.a.	n.a.	2.0	3.9	2.0	5.2	n.a.	0.92	1.2	0.60	1.1	2.1	1.5
	1.0	1.1	n.a.	n.a.	0.84	1.8	0.68	2.4	0.86	0.40	0.51	0.085	0.76	0.95	0.69
	1.6	0.32	n.a.	n.a.	0.26	0.56	0.23	0.84	0.27	0.10	0.36	0.057	0.30	0.33	0.23
	3.1	0.23	n.a.	n.a.	0.24	0.47	0.042	0.36	0.23	0.072	0.29	0.10	0.30	0.23	0.13
	7.3	0.25	n.a.	n.a.	0.066	0.24	0.084	0.085	0.30	0.054	0.034	0.008	0.10	0.12	0.10
Mn	0.57	7.2	n.a.	n.a.	10	7.9	20	15	n.a.	7.8	6.2	5.1	6.3	9.6	5.0
	1.0	4.1	n.a.	n.a.	4.2	4.9	8.7	13	8.3	5.3	2.6	1.7	3.8	5.6	3.3
	1.6	2.4	n.a.	n.a.	1.9	3.2	16	12	11	5.6	3.9	2.0	3.8	6.2	5.0
	3.1	4.8	n.a.	n.a.	4.0	5.5	12	18	22	3.9	9.7	5.9	9.0	9.6	6.3
	7.3	8.2	n.a.	n.a.	4.3	3.2	8.0	13	20	2.7	7.5	4.0	7.9	7.9	5.3
Co	0.57	0.10	n.a.	n.a.	0.13	0.11	0.14	0.20	n.a.	0.092	0.14	0.066	0.045	0.11	0.05
	1.0	0.016	n.a.	n.a.	0.039	0.041	0.10	0.10	0.026	0.054	0.006	0.023	0.012	0.041	0.033
	1.6	0.018	n.a.	n.a.	0.025	0.059	0.14	0.14	0.058	0.025	0.023	0.041	0.046	0.058	0.046
	3.1	0.067	n.a.	n.a.	0.065	0.060	0.058	0.23	0.22	0.028	0.13	0.13	0.13	0.11	0.07
	7.3	0.077	n.a.	n.a.	0.034	0.053	0.10	0.12	0.17	0.025	0.058	0.050	0.10	0.079	0.045

*n.a.: data are not available.

doi:10.6342/NTU202302200

Element	Size (μm)	Concentration (pmol m^{-3})												Avg	SD
		2019				2020									
		Sep	Oct	Nov	Dec	Jan	Feb	Mar	Apr	May	Jun	Jul	Aug		
Ni	0.57	6.3	n.a.	n.a.	3.1	2.7	6.8	4.2	n.a.	2.8	4.0	1.9	1.4	3.7	1.8
	1.0	0.48	n.a.	n.a.	0.49	0.49	0.54	0.85	0.19	0.38	0.06	0.30	0.19	0.40	0.23
	1.6	0.28	n.a.	n.a.	0.38	0.24	0.50	0.58	0.14	0.20	0.17	0.26	0.27	0.30	0.14
	3.1	0.41	n.a.	n.a.	0.39	0.50	0.18	0.77	0.65	0.19	0.62	0.66	0.70	0.51	0.21
	7.3	0.20	n.a.	n.a.	0.13	0.39	0.30	0.53	0.41	0.20	0.32	0.30	0.52	0.33	0.13
V	0.57	18	n.a.	n.a.	7.6	3.6	2.5	3.4	n.a.	4.5	6.2	3.5	3.6	5.9	5.0
	1.0	3.4	n.a.	n.a.	1.3	0.7	0.4	1.2	0.34	0.35	0.58	0.22	0.80	0.93	0.95
	1.6	0.5	n.a.	n.a.	0.2	0.2	0.1	0.2	0.086	0.039	0.18	0.15	0.31	0.20	0.14
	3.1	0.21	n.a.	n.a.	0.12	0.13	0.033	0.12	0.11	0.092	0.11	0.18	0.19	0.13	0.05
	7.3	0.094	n.a.	n.a.	0.067	0.047	0.045	0.082	0.13	0.074	0.047	0.056	0.060	0.070	0.026
Al	0.57	229	n.a.	n.a.	103	441	2271	430	n.a.	425	166	131	68	474	690
	1.0	66	n.a.	n.a.	95	98	393	262	109	77	62	17	74	125	114
	1.6	39	n.a.	n.a.	55	77	99	300	61	255	122	20	72	110	93
	3.1	23	n.a.	n.a.	26	131	4.6	183	80	45	91	27	120	73	58
	7.3	1.6	n.a.	n.a.	2.5	22	5.1	13	117	4.7	4.0	2.3	10	18	35
Fe	0.57	85	n.a.	n.a.	78	59	31	149	n.a.	60	90	66	49	74	34
	1.0	14	n.a.	n.a.	14	30	30	78	33	10	30	4.0	25	27	21
	1.6	3.9	n.a.	n.a.	2.5	9.3	9.2	20	14	2.1	37	7.9	15	12	11
	3.1	2.2	n.a.	n.a.	1.8	6.6	1.5	15	16	2.2	27	10	11	9.3	8.4
	7.3	0.45	n.a.	n.a.	0.54	0.80	1.1	2.4	24	0.51	2.6	1.6	1.5	3.6	7.3
Ti	0.57	0.93	n.a.	n.a.	0.45	0.58	0.58	1.3	n.a.	0.58	3.2	1.3	0.68	1.1	0.8
	1.0	0.33	n.a.	n.a.	0.23	0.63	0.49	1.1	0.53	0.11	0.89	0.09	0.71	0.51	0.34
	1.6	0.088	n.a.	n.a.	0.16	0.007	0.16	0.38	0.12	0.064	0.82	0.25	0.35	0.24	0.24
	3.1	0.070	n.a.	n.a.	0.15	0.11	0.071	0.22	0.42	0.053	0.58	0.35	0.16	0.22	0.18
	7.3	0.033	n.a.	n.a.	0.027	0.031	0.11	0.13	0.81	0.028	0.13	0.072	0.036	0.14	0.24

*n.a.: data are not available.

doi:10.6342/NTU202302200

Table S2.8. The enrichment factors of the elements in the size-fractionated aerosols.

Element	Size	Enrichment Factor												Avg	SD
		2019				2020									
	(μm)	Sep	Oct	Nov	Dec	Jan	Feb	Mar	Apr	May	Jun	Jul	Aug		
Cd	0.57	2002	n.a.	n.a.	2873	3754	818	2084	n.a.	1068	199	529	1576	1656	1153
	1.0	1038	n.a.	n.a.	1290	1068	132	746	355	144	67	153	385	538	458
	1.6	311	n.a.	n.a.	251	317	50	152	126	43	12	44	83	139	115
	3.1	48	n.a.	n.a.	53	108	17	44	32	32	5.7	16	33	39	29
	7.3	17	n.a.	n.a.	20	77	29	25	30	21	3.1	10	26	26	20
Zn	0.57	208	n.a.	n.a.	435	439	88	294	n.a.	172	92	232	558	280	165
	1.0	115	n.a.	n.a.	199	175	26	112	64	30	68	164	227	118	71
	1.6	30	n.a.	n.a.	54	62	10	29	24	13	15	36	54	33	19
	3.1	7.3	n.a.	n.a.	13	39	6.9	14	8.6	10	5.7	15	33	15	12
	7.3	4.7	n.a.	n.a.	12	27	6.9	10	7.1	11	3.6	11	27	12	8
Pb	0.57	337	n.a.	n.a.	529	971	37	435	n.a.	129	43	119	290	329	292
	1.0	135	n.a.	n.a.	157	234	25	99	51	22	21	46	86	88	70
	1.6	29	n.a.	n.a.	29	52	8.1	21	15	6.7	4.6	11	19	20	14
	3.1	8.3	n.a.	n.a.	11	20	5.8	8.7	6.4	4.9	2.4	5.3	10	8.3	4.9
	7.3	5.9	n.a.	n.a.	6.2	12	5.1	4.9	5.4	4.1	1.8	4.2	8.9	5.9	2.8
Mn	0.57	6.5	n.a.	n.a.	17	13	6.0	8.2	n.a.	8.8	1.7	4.4	11	8.5	4.7
	1.0	4.0	n.a.	n.a.	6.8	5.0	1.7	3.6	3.0	2.1	1.1	2.0	4.1	3.3	1.7
	1.6	1.7	n.a.	n.a.	2.2	2.5	2.0	1.8	2.3	1.7	0.6	1.0	2.1	1.8	0.6
	3.1	1.2	n.a.	n.a.	1.3	2.0	1.5	1.7	1.7	1.2	0.52	0.94	1.9	1.4	0.5
	7.3	0.99	n.a.	n.a.	1.2	1.6	1.0	1.2	1.5	1.1	0.44	0.96	1.8	1.2	0.4
Co	0.57	4.1	n.a.	n.a.	12	12	3.4	5.5	n.a.	6.9	1.9	4.0	7.2	6.3	3.5
	1.0	2.6	n.a.	n.a.	6.1	4.7	1.8	2.5	1.6	2.1	0.91	2.0	3.1	2.8	1.6
	1.6	1.5	n.a.	n.a.	2.4	2.6	2.1	2.1	2.4	1.5	0.70	1.3	2.1	1.9	0.6
	3.1	1.2	n.a.	n.a.	1.6	2.7	2.1	1.8	1.9	1.3	0.56	1.2	2.1	1.6	0.6
	7.3	1.1	n.a.	n.a.	1.8	1.7	1.6	1.1	1.3	1.0	0.46	1.1	1.7	1.3	0.4

*n.a.: data are not available.

Element	Size	Concentration (pmol m^{-3})												Avg	SD
		2019				2020									
	(µm)	Sep	Oct	Nov	Dec	Jan	Feb	Mar	Apr	May	Jun	Jul	Aug		
Ni	0.57	110	n.a.	n.a.	141	123	45	55	n.a.	82	26	38	79	78	40
	1.0	25	n.a.	n.a.	22	20	4.4	9.2	5.0	4.2	4.0	10	15	12	8
	1.6	5.5	n.a.	n.a.	65	6.7	3.4	3.8	5.7	2.1	1.6	4.7	6.1	10	19
	3.1	2.2	n.a.	n.a.	4.9	8.8	3.0	3.3	3.1	2.8	1.1	4.1	6.2	4.0	2.2
	7.3	1.9	n.a.	n.a.	8.4	12	2.9	2.5	2.5	2.8	0.7	3.4	5.5	4.3	3.5
V	0.57	91	n.a.	n.a.	76	31	5.2	11	n.a.	28	9.2	18	37	34	30
	1.0	18	n.a.	n.a.	10	4.5	1.9	2.8	1.6	2.5	2.0	2.7	5.1	5.1	5.1
	1.6	4.1	n.a.	n.a.	3.4	2.5	1.8	1.7	1.7	1.6	1.1	1.4	2.1	2.2	0.9
	3.1	1.8	n.a.	n.a.	1.8	1.9	1.7	1.5	1.4	1.8	1.0	1.2	1.6	1.6	0.3
	7.3	1.0	n.a.	n.a.	1.4	1.8	1.4	1.2	1.3	1.4	0.92	1.1	1.4	1.3	0.3
Al	0.57	1.1	n.a.	n.a.	1.7	6.6	3.2	1.0	n.a.	3.4	0.54	0.90	1.3	2.2	1.9
	1.0	0.70	n.a.	n.a.	1.1	0.92	1.1	0.88	0.74	1.1	0.42	1.0	0.85	0.87	0.21
	1.6	0.82	n.a.	n.a.	1.1	1.4	0.86	0.89	1.2	0.80	0.31	0.47	0.52	0.83	0.33
	3.1	0.52	n.a.	n.a.	1.2	1.0	1.2	0.66	0.78	1.0	0.27	0.36	0.56	0.76	0.34
	7.3	0.59	n.a.	n.a.	0.85	2.3	0.90	0.60	0.67	0.70	0.30	0.39	1.1	0.84	0.55
Fe	0.57	1.8	n.a.	n.a.	3.4	2.7	1.7	2.2	n.a.	1.8	1.5	1.7	2.5	2.1	0.6
	1.0	1.5	n.a.	n.a.	2.1	1.9	1.7	1.7	1.6	1.5	1.5	1.8	1.9	1.7	0.2
	1.6	1.4	n.a.	n.a.	1.7	1.9	1.8	1.7	1.9	1.5	1.5	1.6	1.7	1.7	0.2
	3.1	1.3	n.a.	n.a.	1.5	1.8	2.0	1.6	1.8	1.4	1.3	1.5	1.8	1.6	0.2
	7.3	1.4	n.a.	n.a.	1.3	1.4	1.5	1.5	1.5	1.3	1.2	1.4	1.6	1.4	0.1

*n.a.: data are not available.

Table S2.9. The elemental solubility data of the Chinese desert dust with different leaching treatments.

Leaching Treatment	Sample	n	Solubility (%)									
			Al	Ti	V	Mn	Fe	Co	Ni	Zn	Cd	Pb
Berger	ATD	5	3.1	0.06	7.3	44	12	22	11	17	61	28
	TK1	3	2.5	0.08	4.2	49	5.2	21	12	11	87	41
	TK2	3	1.9	0.06	5.8	52	2.7	13	6.4	14	85	40
	TG	3	2.2	0.10	5.9	50	5.0	19	12	14	85	41
	QD	3	1.4	0.05	3.2	46	3.1	15	7.5	10	68	35
	BJ	6	11	1.4	25	61	19	26	25	80	79	74
Buffer	ATD	5	0.56	0.20	3.7	21	1.1	5.6	5.8	16	64	19
	TK1	3	0.17	0.071	0.71	34	0.64	5.0	1.2	1.9	79	20
	TK2	3	0.11	0.042	1.2	41	0.36	3.7	0.49	4.7	80	26
	TG	3	0.11	0.013	0.53	26	0.24	4.9	1.2	2.0	84	27
	QD	3	0.11	0.036	0.66	30	0.42	13	1.4	2.8	66	22
	BJ	6	3.2	1.7	8.8	49	4.6	16	16	78	80	71
Ultrapure water	ATD	5	0.012	0.004	0.51	0.11	0.004	0.060	0.031	0.088	0.23	0.02
	TK1	3	0.004	0.002	0.018	0.30	0.004	0.062	0.024	0.012	0.09	0.01
	TK2	3	0.004	0.001	0.064	0.10	0.001	0.014	0.014	0.025	0.19	0.01
	TG	3	0.001	0.001	0.019	0.062	0.002	0.071	0.053	0.012	0.20	0.01
	QD	3	0.002	0.001	0.019	0.11	0.012	0.062	0.047	0.013	0.08	0.01
	BJ	6	0.77	0.56	1.8	35	1.2	10	12	51	52	8.7

*n.a.: data are not available.

Table S2.10. The elemental deposition fluxes estimated from concentrations obtained by total digestion.

Element	Size	Deposition flux (nmol m^{-2} day^{-1})												Avg	SD
		2019				2020									
	(μm)	Sep	Oct	Nov	Dec	Jan	Feb	Mar	Apr	May	Jun	Jul	Aug		
Cd	0.57	0.002	n.a.	n.a.	0.002	0.003	0.003	0.004	n.a.	0.001	0.001	0.001	0.001	0.002	0.001
	1.0	0.003	n.a.	n.a.	0.002	0.003	0.003	0.007	0.003	0.001	0.001	0.001	0.001	0.003	0.002
	1.6	0.012	n.a.	n.a.	0.002	0.005	0.006	0.010	0.006	0.002	0.001	0.001	0.002	0.005	0.004
	3.1	0.050	n.a.	n.a.	0.012	0.021	0.033	0.050	0.044	0.010	0.020	0.010	0.012	0.026	0.017
	7.3	0.12	n.a.	n.a.	0.030	0.042	0.062	0.064	0.11	0.012	0.046	0.021	0.027	0.053	0.037
Zn	0.57	0.24	n.a.	n.a.	0.34	0.34	0.33	0.57	n.a.	0.16	0.41	0.24	0.29	0.32	0.12
	1.0	0.33	n.a.	n.a.	0.46	0.46	0.56	1.1	0.51	0.15	0.80	0.42	0.60	0.53	0.26
	1.6	0.50	n.a.	n.a.	0.86	0.86	1.2	1.8	1.4	0.43	1.7	0.81	1.0	1.1	0.5
	3.1	3.9	n.a.	n.a.	7.3	7.3	13	15	11	2.9	19	9.0	11	10	5
	7.3	17	n.a.	n.a.	14	14	14	25	25	5.8	52	22	27	23	13
Pb	0.57	0.039	n.a.	n.a.	0.029	0.073	0.039	0.081	n.a.	0.012	0.019	0.012	0.014	0.035	0.026
	1.0	0.042	n.a.	n.a.	0.025	0.060	0.052	0.090	0.039	0.014	0.024	0.011	0.022	0.038	0.024
	1.6	0.10	n.a.	n.a.	0.026	0.070	0.093	0.13	0.094	0.022	0.051	0.024	0.035	0.065	0.038
	3.1	0.80	n.a.	n.a.	0.24	0.36	1.1	0.93	0.83	0.13	0.78	0.30	0.35	0.58	0.33
	7.3	4.0	n.a.	n.a.	0.85	0.61	1.0	1.2	1.8	0.22	2.5	0.79	0.87	1.4	1.1
Mn	0.57	0.093	n.a.	n.a.	0.095	0.095	0.22	0.15	n.a.	0.079	0.073	0.043	0.059	0.10	0.05
	1.0	0.11	n.a.	n.a.	0.13	0.13	0.35	0.32	0.23	0.10	0.13	0.050	0.11	0.16	0.10
	1.6	0.20	n.a.	n.a.	0.34	0.34	2.3	1.1	1.0	0.57	0.71	0.22	0.37	0.74	0.62
	3.1	2.8	n.a.	n.a.	3.5	3.5	28	18	22	3.3	17	5.3	6.2	12	9
	7.3	17	n.a.	n.a.	8.0	8.0	20	29	50	6.0	60	18	18	29	22
Co	0.57	0.001	n.a.	n.a.	0.002	0.002	0.003	0.002	n.a.	0.001	0.002	0.001	0.001	0.001	0.001
	1.0	0.002	n.a.	n.a.	0.002	0.002	0.007	0.005	0.003	0.002	0.002	0.001	0.002	0.003	0.002
	1.6	0.004	n.a.	n.a.	0.007	0.007	0.047	0.025	0.012	0.010	0.016	0.006	0.008	0.014	0.013
	3.1	0.070	n.a.	n.a.	0.095	0.095	0.76	0.39	0.48	0.071	0.36	0.13	0.14	0.27	0.22
	7.3	0.48	n.a.	n.a.	0.17	0.17	0.62	0.55	0.90	0.10	1.2	0.40	0.33	0.63	0.45

*n.a.: data are not available.

Element	Size (μm)	Deposition flux (nmol m^{-2} day^{-1})												Avg	SD
		2019				2020									
		Sep	Oct	Nov	Dec	Jan	Feb	Mar	Apr	May	Jun	Jul	Aug		
Ni	0.57	0.061	n.a.	n.a.	0.036	0.044	0.078	0.049	n.a.	0.035	0.053	0.018	0.018	0.043	0.019
	1.0	0.036	n.a.	n.a.	0.017	0.024	0.043	0.040	0.018	0.009	0.022	0.012	0.018	0.024	0.012
	1.6	0.094	n.a.	n.a.	0.056	0.042	0.18	0.110	0.069	0.033	0.086	0.048	0.053	0.077	0.044
	3.1	1.0	n.a.	n.a.	0.50	0.75	2.7	1.6	1.9	0.37	1.6	1.1	0.97	1.3	0.7
	7.3	6.1	n.a.	n.a.	5.5	2.9	2.7	2.9	3.9	0.7	4.8	3.1	2.5	3.5	1.6
V	0.57	0.18	n.a.	n.a.	0.069	0.039	0.032	0.036	n.a.	0.042	0.068	0.030	0.031	0.058	0.047
	1.0	0.093	n.a.	n.a.	0.027	0.019	0.065	0.043	0.020	0.019	0.038	0.011	0.022	0.036	0.026
	1.6	0.24	n.a.	n.a.	0.051	0.057	0.35	0.17	0.075	0.088	0.20	0.053	0.065	0.14	0.10
	3.1	2.9	n.a.	n.a.	0.66	0.58	5.2	2.6	3.1	0.85	5.4	1.2	0.91	2.3	1.8
	7.3	12	n.a.	n.a.	3.1	1.6	4.6	4.9	7.3	1.3	21	3.6	2.3	6.1	6.1
Al	0.57	4.0	n.a.	n.a.	3.0	16	39	6.3	n.a.	10	7.8	3.0	2.1	10	12
	1.0	7.2	n.a.	n.a.	5.6	7.7	78	26	19	17	16	7.9	7.2	19	22
	1.6	96	n.a.	n.a.	32	60	322	177	100	88	113	34	32	105	88
	3.1	1649	n.a.	n.a.	864	604	7640	2280	3290	875	2913	673	606	2139	2174
	7.3	12932	n.a.	n.a.	3867	3749	5856	4815	7454	1206	13311	2398	3580	5917	4169
Fe	0.57	1.2	n.a.	n.a.	1.0	1.2	3.6	2.3	n.a.	0.90	3.6	1.0	0.7	1.7	1.2
	1.0	2.6	n.a.	n.a.	1.9	2.7	20	8.8	7.2	3.9	10	2.5	2.7	6.2	5.6
	1.6	28	n.a.	n.a.	8.7	14	117	57	27	27	96	19	17	41	37
	3.1	710	n.a.	n.a.	176	178	2062	939	1308	223	2328	494	332	875	787
	7.3	5320	n.a.	n.a.	1018	403	1664	1994	2883	374	9458	1488	870	2547	2833
Ti	0.57	0.11	n.a.	n.a.	0.051	0.071	0.34	0.18	n.a.	0.085	0.41	0.095	0.047	0.15	0.13
	1.0	0.29	n.a.	n.a.	0.15	0.24	2.0	0.86	0.73	0.44	1.1	0.23	0.24	0.62	0.57
	1.6	3.4	n.a.	n.a.	0.84	1.3	11	5.7	2.4	3.2	10	2.0	1.7	4.2	3.6
	3.1	91	n.a.	n.a.	20	17	175	100	121	26	305	54	31	94	90
	7.3	632	n.a.	n.a.	130	48	186	228	319	50	1292	178	92	315	384

*n.a.: data are not available.

doi:10.6342/NTU202302200

Table S2.11. The elemental deposition fluxes estimated from concentrations obtained by Berger leaching.

Element	Size	Deposition flux (nmol m^{-2} day^{-1})												Avg	SD
		2019				2020									
	(μm)	Sep	Oct	Nov	Dec	Jan	Feb	Mar	Apr	May	Jun	Jul	Aug		
Cd	0.57	0.002	n.a.	n.a.	0.001	0.003	0.002	0.003	n.a.	0.001	0.001	0.001	0.001	0.002	0.001
	1.0	0.002	n.a.	n.a.	0.002	0.002	0.003	0.006	0.003	0.001	0.001	0.001	0.001	0.002	0.002
	1.6	0.009	n.a.	n.a.	0.002	0.004	0.004	0.008	0.007	0.002	0.001	0.001	0.001	0.004	0.003
	3.1	0.044	n.a.	n.a.	0.007	0.012	0.024	0.037	0.031	0.008	0.006	0.006	0.009	0.018	0.014
	7.3	0.051	n.a.	n.a.	0.019	0.020	0.045	0.044	0.069	0.013	0.044	0.015	0.013	0.033	0.020
Zn	0.57	0.23	n.a.	n.a.	0.21	0.34	0.26	0.45	n.a.	0.17	0.34	0.20	0.30	0.28	0.09
	1.0	0.29	n.a.	n.a.	0.29	0.42	0.50	0.97	0.54	0.15	0.53	0.23	0.47	0.44	0.23
	1.6	0.85	n.a.	n.a.	0.39	0.71	0.79	1.4	1.1	0.32	1.1	0.48	0.73	0.79	0.34
	3.1	4.5	n.a.	n.a.	2.4	7.6	9.2	8.9	7.0	3.2	10	5.0	9.3	6.8	2.8
	7.3	17	n.a.	n.a.	7.8	8.3	11	28	16	4.8	24	14	21	15	7
Pb	0.57	0.034	n.a.	n.a.	0.025	0.065	0.031	0.066	n.a.	0.012	0.018	0.010	0.014	0.030	0.021
	1.0	0.033	n.a.	n.a.	0.023	0.049	0.048	0.083	0.041	0.014	0.020	0.008	0.018	0.034	0.022
	1.6	0.086	n.a.	n.a.	0.022	0.060	0.076	0.106	0.064	0.023	0.039	0.016	0.026	0.052	0.031
	3.1	0.60	n.a.	n.a.	0.16	0.27	0.78	0.64	0.54	0.12	0.34	0.17	0.27	0.39	0.23
	7.3	2.1	n.a.	n.a.	0.54	0.46	0.86	1.2	1.3	0.21	0.86	0.54	0.53	0.86	0.55
Mn	0.57	0.062	n.a.	n.a.	0.071	0.081	0.13	0.11	n.a.	0.048	0.051	0.032	0.053	0.071	0.032
	1.0	0.076	n.a.	n.a.	0.078	0.10	0.24	0.23	0.19	0.089	0.062	0.023	0.058	0.11	0.08
	1.6	0.36	n.a.	n.a.	0.12	0.21	0.91	0.64	0.80	0.30	0.31	0.10	0.15	0.39	0.29
	3.1	6.0	n.a.	n.a.	1.4	1.8	16	8.9	11	3.1	4.5	2.4	3.5	5.9	4.8
	7.3	29	n.a.	n.a.	6.8	3.9	11	17	27	3.6	15	7.8	10	13	9
Co	0.57	0.001	n.a.	n.a.	0.001	0.001	0.001	0.001	n.a.	0.001	0.001	0.001	0.001	0.001	0.001
	1.0	0.001	n.a.	n.a.	0.001	0.001	0.002	0.002	0.001	0.001	0.001	0.001	0.001	0.001	0.001
	1.6	0.005	n.a.	n.a.	0.001	0.002	0.012	0.008	0.005	0.004	0.004	0.002	0.002	0.004	0.003
	3.1	0.070	n.a.	n.a.	0.021	0.025	0.28	0.11	0.11	0.030	0.079	0.049	0.055	0.082	0.076
	7.3	0.45	n.a.	n.a.	0.099	0.064	0.36	0.21	0.30	0.028	0.28	0.14	0.21	0.21	0.13

*n.a.: data are not available.

doi:10.6342/NTU202302200

Element	Size (μm)	Deposition flux (nmol m^{-2} day^{-1})												Avg	SD
		2019				2020									
		Sep	Oct	Nov	Dec	Jan	Feb	Mar	Apr	May	Jun	Jul	Aug		
Ni	0.57	0.051	n.a.	n.a.	0.019	0.024	0.042	0.028	n.a.	0.025	0.025	0.011	0.011	0.026	0.013
	1.0	0.017	n.a.	n.a.	0.007	0.011	0.014	0.016	0.008	0.004	0.006	0.008	0.005	0.009	0.005
	1.6	0.032	n.a.	n.a.	0.020	0.024	0.038	0.023	0.036	0.012	0.029	0.012	0.009	0.023	0.010
	3.1	0.22	n.a.	n.a.	0.22	0.27	0.67	0.28	0.26	0.10	0.40	0.25	0.24	0.29	0.15
	7.3	0.89	n.a.	n.a.	0.58	2.1	1.7	1.2	1.1	0.22	0.51	0.80	0.84	1.0	0.6
V	0.57	0.15	n.a.	n.a.	0.061	0.036	0.019	0.026	n.a.	0.044	0.061	0.023	0.032	0.050	0.040
	1.0	0.071	n.a.	n.a.	0.023	0.014	0.020	0.022	0.009	0.011	0.022	0.004	0.011	0.021	0.019
	1.6	0.16	n.a.	n.a.	0.032	0.022	0.058	0.041	0.070	0.023	0.040	0.014	0.017	0.047	0.043
	3.1	1.4	n.a.	n.a.	0.28	0.17	0.77	0.56	0.43	0.24	0.48	0.24	0.27	0.49	0.38
	7.3	3.3	n.a.	n.a.	0.91	0.32	0.73	1.0	1.1	0.36	1.9	0.70	0.73	1.1	0.9
Al	0.57	1.9	n.a.	n.a.	1.4	8.6	21	2.2	n.a.	3.9	1.2	1.3	0.92	4.7	6.6
	1.0	2.9	n.a.	n.a.	2.0	4.2	16	8.1	4.0	2.7	3.3	1.3	2.5	4.7	4.3
	1.6	18	n.a.	n.a.	12	12	124	35	10	9.1	21	6.0	5.5	25	36
	3.1	384	n.a.	n.a.	271	141	903	389	205	674	353	137	208	366	246
	7.3	3273	n.a.	n.a.	1438	1223	1263	671	577	641	1691	329	503	1161	870
Fe	0.57	0.79	n.a.	n.a.	0.64	0.70	0.63	1.2	n.a.	0.46	0.94	0.51	0.48	0.71	0.25
	1.0	0.91	n.a.	n.a.	0.73	0.88	4.1	2.4	1.9	1.2	3.1	0.78	0.73	1.7	1.2
	1.6	6.6	n.a.	n.a.	1.8	2.8	14.1	7.9	6.5	3.9	19.1	5.2	2.9	7.1	5.5
	3.1	118	n.a.	n.a.	27	24	197	116	114	26	207	102	50	98	67
	7.3	482	n.a.	n.a.	146	46	206	265	260	54	630	250	115	245	185
Ti	0.57	0.015	n.a.	n.a.	0.005	0.008	0.010	0.011	n.a.	0.016	0.029	0.016	0.009	0.013	0.007
	1.0	0.024	n.a.	n.a.	0.012	0.010	0.014	0.023	0.013	0.011	0.059	0.023	0.018	0.021	0.014
	1.6	0.19	n.a.	n.a.	0.036	0.019	0.070	0.057	0.16	0.078	0.27	0.16	0.036	0.11	0.08
	3.1	4.1	n.a.	n.a.	0.72	0.33	1.4	1.2	0.83	0.41	2.4	1.7	0.15	1.3	1.2
	7.3	13.1	n.a.	n.a.	4.7	1.9	4.7	5.7	2.9	0.86	6.3	5.2	2.3	4.8	3.4

*n.a.: data are not available.

doi:10.6342/NTU202302200

Table S2.12. The elemental deposition fluxes estimated from concentrations obtained by buffer leaching.

Element	Size	Deposition flux (nmol m^{-2} day^{-1})												Avg	SD
		2019				2020									
	(μm)	Sep	Oct	Nov	Dec	Jan	Feb	Mar	Apr	May	Jun	Jul	Aug		
Cd	0.57	0.002	n.a.	n.a.	0.001	0.002	0.004	0.004	n.a.	0.001	0.001	0.001	0.001	0.002	0.001
	1.0	0.003	n.a.	n.a.	0.002	0.003	0.002	0.005	0.003	0.001	0.001	0.001	0.001	0.002	0.001
	1.6	0.011	n.a.	n.a.	0.002	0.004	0.005	0.010	0.006	0.001	0.001	0.001	0.002	0.004	0.004
	3.1	0.044	n.a.	n.a.	0.012	0.022	0.028	0.026	0.043	0.007	0.012	0.008	0.012	0.021	0.014
	7.3	0.076	n.a.	n.a.	0.024	0.021	0.048	0.049	0.067	0.011	0.039	0.017	0.020	0.037	0.022
Zn	0.57	0.25	n.a.	n.a.	0.17	0.27	0.27	0.54	n.a.	0.17	0.35	0.21	0.27	0.28	0.11
	1.0	0.32	n.a.	n.a.	0.33	0.45	0.33	0.70	0.54	0.15	0.62	0.33	0.48	0.43	0.16
	1.6	0.84	n.a.	n.a.	0.36	0.59	0.95	1.6	1.0	0.31	1.2	0.65	1.15	0.86	0.39
	3.1	4.4	n.a.	n.a.	3.2	5.1	5.2	5.9	7.8	1.9	11	6.3	10	6.1	2.9
	7.3	14	n.a.	n.a.	8.3	6.3	11	20	13	6.0	28	14	21	14	7
Pb	0.57	0.036	n.a.	n.a.	0.019	0.065	0.026	0.080	n.a.	0.011	0.018	0.009	0.013	0.031	0.025
	1.0	0.036	n.a.	n.a.	0.026	0.055	0.032	0.070	0.040	0.014	0.019	0.010	0.018	0.032	0.019
	1.6	0.089	n.a.	n.a.	0.027	0.051	0.074	0.12	0.063	0.015	0.034	0.016	0.034	0.053	0.035
	3.1	0.51	n.a.	n.a.	0.22	0.33	0.52	0.47	0.57	0.087	0.32	0.15	0.30	0.35	0.17
	7.3	2.1	n.a.	n.a.	0.68	0.32	0.82	0.89	1.0	0.15	0.64	0.37	0.54	0.75	0.54
Mn	0.57	0.069	n.a.	n.a.	0.058	0.066	0.18	0.13	n.a.	0.049	0.050	0.036	0.050	0.077	0.048
	1.0	0.073	n.a.	n.a.	0.079	0.10	0.13	0.16	0.18	0.080	0.057	0.024	0.054	0.093	0.049
	1.6	0.29	n.a.	n.a.	0.16	0.17	0.93	0.67	0.68	0.27	0.26	0.095	0.22	0.37	0.28
	3.1	3.6	n.a.	n.a.	2.1	2.3	9.5	5.2	12	1.2	5.5	2.2	3.7	4.7	3.5
	7.3	15	n.a.	n.a.	6.1	3.1	8.0	15	22	2.3	16	6.3	9.4	10	6
Co	0.57	0.001	n.a.	n.a.	0.001	0.001	0.001	0.002	n.a.	0.001	0.001	0.001	0.001	0.001	0.001
	1.0	0.001	n.a.	n.a.	0.001	0.001	0.001	0.001	0.001	0.001	0.001	0.001	0.001	0.001	0.001
	1.6	0.004	n.a.	n.a.	0.003	0.003	0.009	0.008	0.007	0.003	0.005	0.002	0.003	0.005	0.002
	3.1	0.050	n.a.	n.a.	0.037	0.043	0.077	0.069	0.11	0.011	0.083	0.052	0.055	0.059	0.028
	7.3	0.17	n.a.	n.a.	0.079	0.057	0.17	0.16	0.19	0.026	0.24	0.11	0.11	0.13	0.07

*n.a.: data are not available.

Element	Size (μm)	Deposition flux (nmol m^{-2} day^{-1})												Avg	SD
		2019				2020									
		Sep	Oct	Nov	Dec	Jan	Feb	Mar	Apr	May	Jun	Jul	Aug		
Ni	0.57	0.051	n.a.	n.a.	0.017	0.019	0.062	0.035	n.a.	0.020	0.035	0.013	0.013	0.030	0.017
	1.0	0.025	n.a.	n.a.	0.010	0.013	0.010	0.013	0.008	0.008	0.009	0.005	0.007	0.011	0.006
	1.6	0.043	n.a.	n.a.	0.018	0.014	0.059	0.030	0.022	0.010	0.028	0.016	0.020	0.026	0.015
	3.1	0.35	n.a.	n.a.	0.20	0.25	0.23	0.22	0.28	0.079	0.39	0.30	0.36	0.27	0.09
	7.3	0.70	n.a.	n.a.	0.39	0.42	0.63	0.68	0.56	0.19	1.2	0.79	0.88	0.65	0.29
V	0.57	0.14	n.a.	n.a.	0.043	0.027	0.025	0.032	n.a.	0.031	0.054	0.026	0.028	0.045	0.037
	1.0	0.074	n.a.	n.a.	0.025	0.016	0.008	0.016	0.007	0.008	0.014	0.005	0.013	0.019	0.020
	1.6	0.090	n.a.	n.a.	0.031	0.013	0.009	0.016	0.008	0.007	0.021	0.010	0.019	0.022	0.025
	3.1	0.47	n.a.	n.a.	0.16	0.084	0.13	0.073	0.12	0.075	0.16	0.12	0.17	0.15	0.12
	7.3	0.66	n.a.	n.a.	0.33	0.10	0.18	0.17	0.27	0.10	0.32	0.33	0.22	0.27	0.16
Al	0.57	2.6	n.a.	n.a.	1.9	2.9	24	4.6	n.a.	4.5	0.93	0.90	1.2	4.9	7.5
	1.0	5.6	n.a.	n.a.	2.1	4.1	7.3	4.3	1.8	2.4	1.5	0.45	1.0	3.0	2.2
	1.6	16	n.a.	n.a.	77	5.2	41	28	5.7	2.6	9.5	2.5	10	20	24
	3.1	188	n.a.	n.a.	559	223	106	128	98	59	157	81	91	169	146
	7.3	372	n.a.	n.a.	270	410	256	152	211	82	165	122	234	227	105
Fe	0.57	0.65	n.a.	n.a.	0.42	0.48	0.38	1.3	n.a.	0.41	0.77	0.49	0.40	0.59	0.30
	1.0	0.41	n.a.	n.a.	0.30	0.59	0.89	1.2	0.78	0.34	0.84	0.20	0.38	0.60	0.33
	1.6	1.2	n.a.	n.a.	0.63	0.81	2.2	2.2	1.8	0.53	4.5	1.3	1.0	1.60	1.2
	3.1	16	n.a.	n.a.	10	7.7	24	17	27	3.2	51	19	10	18.40	13
	7.3	41	n.a.	n.a.	38	9.2	51	48	70	6.9	86	71	15	43.67	27
Ti	0.57	0.013	n.a.	n.a.	0.003	0.005	0.014	0.014	n.a.	0.005	0.026	0.013	0.006	0.011	0.007
	1.0	0.011	n.a.	n.a.	0.005	0.011	0.010	0.016	0.012	0.002	0.025	0.008	0.010	0.011	0.006
	1.6	0.045	n.a.	n.a.	0.020	0.010	0.031	0.031	0.026	0.004	0.11	0.058	0.021	0.035	0.030
	3.1	0.59	n.a.	n.a.	0.35	0.19	0.42	0.38	0.52	0.05	1.3	0.72	0.16	0.47	0.37
	7.3	1.9	n.a.	n.a.	1.6	0.34	1.8	1.4	2.0	0.20	1.9	2.9	0.4	1.4	0.9

*n.a.: data are not available.

Table S2.13. The elemental deposition fluxes estimated by concentrations obtained by ultrapure water leaching.

Element	Size	Deposition flux (nmol m^{-2} day^{-1})												Avg	SD
		2019				2020									
	(μm)	Sep	Oct	Nov	Dec	Jan	Feb	Mar	Apr	May	Jun	Jul	Aug		
Cd	0.57	0.003	n.a.	n.a.	0.002	0.003	0.003	0.004	n.a.	0.001	0.001	0.001	0.001	0.002	0.001
	1.0	0.003	n.a.	n.a.	0.002	0.003	0.002	0.005	0.003	0.001	0.001	0.001	0.001	0.002	0.002
	1.6	0.009	n.a.	n.a.	0.002	0.004	0.005	0.010	0.006	0.001	0.001	0.001	0.002	0.004	0.003
	3.1	0.040	n.a.	n.a.	0.013	0.024	0.026	0.040	0.036	0.009	0.020	0.007	0.011	0.023	0.013
	7.3	0.048	n.a.	n.a.	0.020	0.022	0.052	0.062	0.075	0.013	0.016	0.015	0.020	0.034	0.023
Zn	0.57	0.27	n.a.	n.a.	0.25	0.33	0.25	0.58	n.a.	0.11	0.36	0.24	0.32	0.30	0.13
	1.0	0.30	n.a.	n.a.	0.32	0.40	0.38	0.85	0.26	0.14	0.38	0.37	0.46	0.39	0.18
	1.6	0.83	n.a.	n.a.	0.45	0.72	0.78	1.7	0.93	0.29	0.98	0.73	0.96	0.84	0.38
	3.1	3.9	n.a.	n.a.	3.5	6.0	3.6	8.6	7.0	2.3	7.8	6.5	6.4	5.6	2.1
	7.3	8.1	n.a.	n.a.	3.5	8.8	8.4	16	13	4.0	5.9	8.1	20.5	10	5
Pb	0.57	0.022	n.a.	n.a.	0.018	0.036	0.019	0.046	n.a.	0.008	0.010	0.005	0.010	0.019	0.014
	1.0	0.020	n.a.	n.a.	0.014	0.031	0.012	0.040	0.015	0.007	0.008	0.001	0.013	0.016	0.012
	1.6	0.031	n.a.	n.a.	0.015	0.032	0.013	0.046	0.015	0.005	0.020	0.003	0.018	0.020	0.013
	3.1	0.17	n.a.	n.a.	0.11	0.24	0.023	0.16	0.11	0.032	0.13	0.035	0.19	0.12	0.07
	7.3	0.35	n.a.	n.a.	0.068	0.27	0.10	0.088	0.33	0.054	0.033	0.007	0.13	0.14	0.13
Mn	0.57	0.073	n.a.	n.a.	0.089	0.074	0.19	0.13	n.a.	0.067	0.051	0.040	0.060	0.087	0.048
	1.0	0.072	n.a.	n.a.	0.070	0.085	0.15	0.21	0.14	0.086	0.041	0.026	0.064	0.10	0.06
	1.6	0.24	n.a.	n.a.	0.11	0.18	0.91	0.67	0.60	0.32	0.21	0.11	0.23	0.36	0.27
	3.1	3.6	n.a.	n.a.	1.8	2.8	6.8	8.1	11	1.7	4.4	2.1	5.9	4.8	3.0
	7.3	11	n.a.	n.a.	4.4	3.7	10	14	22	2.7	7.3	3.4	10	8.8	6.0
Co	0.57	0.001	n.a.	n.a.	0.001	0.001	0.001	0.002	n.a.	0.001	0.001	0.001	0.001	0.001	0.001
	1.0	0.001	n.a.	n.a.	0.001	0.001	0.002	0.002	0.001	0.001	0.001	0.001	0.001	0.001	0.001
	1.6	0.002	n.a.	n.a.	0.001	0.003	0.008	0.008	0.003	0.001	0.001	0.002	0.003	0.003	0.002
	3.1	0.049	n.a.	n.a.	0.030	0.031	0.032	0.10	0.11	0.012	0.060	0.048	0.082	0.055	0.032
	7.3	0.10	n.a.	n.a.	0.035	0.060	0.12	0.12	0.19	0.025	0.057	0.043	0.13	0.088	0.052

*n.a.: data are not available.

Element	Size (μm)	Deposition flux (nmol m^{-2} day^{-1})												Avg	SD
		2019				2020									
		Sep	Oct	Nov	Dec	Jan	Feb	Mar	Apr	May	Jun	Jul	Aug		
Ni	0.57	0.064	n.a.	n.a.	0.027	0.025	0.064	0.037	n.a.	0.024	0.032	0.015	0.014	0.034	0.019
	1.0	0.009	n.a.	n.a.	0.008	0.008	0.009	0.014	0.003	0.006	0.001	0.005	0.003	0.007	0.004
	1.6	0.028	n.a.	n.a.	0.021	0.014	0.028	0.032	0.008	0.011	0.009	0.014	0.016	0.018	0.009
	3.1	0.30	n.a.	n.a.	0.18	0.26	0.10	0.34	0.31	0.087	0.28	0.24	0.46	0.26	0.11
	7.3	0.27	n.a.	n.a.	0.13	0.44	0.36	0.55	0.45	0.20	0.31	0.26	0.66	0.36	0.16
V	0.57	0.19	n.a.	n.a.	0.067	0.034	0.023	0.030	n.a.	0.039	0.051	0.027	0.034	0.055	0.052
	1.0	0.060	n.a.	n.a.	0.021	0.012	0.007	0.020	0.006	0.006	0.009	0.003	0.013	0.016	0.017
	1.6	0.053	n.a.	n.a.	0.013	0.011	0.004	0.012	0.005	0.002	0.010	0.008	0.019	0.014	0.015
	3.1	0.16	n.a.	n.a.	0.055	0.069	0.018	0.052	0.054	0.041	0.048	0.065	0.13	0.069	0.042
	7.3	0.13	n.a.	n.a.	0.069	0.053	0.054	0.085	0.14	0.074	0.046	0.048	0.076	0.077	0.032
Al	0.57	2.3	n.a.	n.a.	0.90	4.1	21	3.8	n.a.	3.6	1.4	1.0	0.65	4.4	6.6
	1.0	1.2	n.a.	n.a.	1.6	1.7	6.8	4.4	1.9	1.3	1.0	0.27	1.3	2.1	2.0
	1.6	3.9	n.a.	n.a.	3.1	4.4	5.5	16	3.4	14	6.7	1.1	4.4	6.3	5.0
	3.1	17	n.a.	n.a.	12	68	2.5	81	38	20	41	9.9	78	37	29
	7.3	2.2	n.a.	n.a.	2.6	25	6.2	13	128	4.7	3.9	2.0	12	20	39
Fe	0.57	0.86	n.a.	n.a.	0.68	0.55	0.29	1.3	n.a.	0.52	0.74	0.51	0.46	0.66	0.30
	1.0	0.25	n.a.	n.a.	0.24	0.51	0.52	1.3	0.55	0.16	0.48	0.06	0.41	0.45	0.34
	1.6	0.38	n.a.	n.a.	0.14	0.54	0.52	1.1	0.79	0.12	2.0	0.41	0.93	0.69	0.57
	3.1	1.6	n.a.	n.a.	0.81	3.4	0.84	6.5	8.0	0.97	12	3.6	6.9	4.5	3.8
	7.3	0.62	n.a.	n.a.	0.55	0.91	1.4	2.5	27	0.52	2.6	1.4	1.9	3.9	8.0
Ti	0.57	0.009	n.a.	n.a.	0.004	0.005	0.006	0.012	n.a.	0.005	0.026	0.010	0.006	0.009	0.007
	1.0	0.006	n.a.	n.a.	0.004	0.011	0.008	0.019	0.009	0.002	0.014	0.001	0.012	0.009	0.006
	1.6	0.009	n.a.	n.a.	0.009	0.001	0.009	0.021	0.007	0.004	0.045	0.013	0.021	0.014	0.013
	3.1	0.052	n.a.	n.a.	0.071	0.055	0.039	0.096	0.21	0.024	0.26	0.13	0.10	0.10	0.08
	7.3	0.044	n.a.	n.a.	0.027	0.035	0.13	0.14	0.88	0.028	0.12	0.06	0.05	0.15	0.26

*n.a.: data are not available.

doi:10.6342/NTU202302200

Chapter 3

The solubility and deposition flux of East Asian aerosol metals in the East China Sea: the effects of aeolian transport processes

By
Chih-Chiang Hsieh[a,b], Hung-Yu Chen[c], and Tung-Yuan Ho[*a,b]

[a] Research Center for Environmental Changes, Academia Sinica, Taipei, Taiwan
[b] Institute of Oceanography, National Taiwan University, Taipei, Taiwan
[c] Department of Marine Environmental Informatics, National Taiwan Ocean University, Keelung, Taiwan

[*]corresponding author: tyho@gate.sinica.edu.tw

Published in *Marine Chemistry*.

Paper Citation:

Hsieh, C.-C., Chen, H.-Y. and Ho, T.-Y., 2022. The effect of aerosol size on Fe solubility and deposition flux: A case study in the East China Sea. Marine Chemistry, 241 DOI: 10.1016/j.marchem.2022.104106.

3.0 Abstract

Aerosol sizes are highly associated with the solubilities and the deposition fluxes of aerosol Fe in the surface ocean since the sizes may reflect the sources and decide the deposition velocities. However, systematic studies on the association of the solubilities and fluxes have been limited. In this study, five size-fractions of dry aerosols were collected monthly for a year at two islets in the East China Sea, where large amounts of both fine anthropogenic and coarse lithogenic aerosols deposit. Both pure water and buffer leached methodologies were applied to determine the two operationally defined soluble Fe fractions, instantly dissolved Fe (DFe) and supposedly Fe-ligand complexed labile Fe (LFe), respectively. We found that the solubilities of DFe varied up to 4 orders of magnitude with the size spectrum and exhibited a highly linear correlation with non-sea-salt sulfur, indicating that the solubilities of DFe were closely associated with the acidity. Finer aerosols (PM 3) accounted for 90% of total DFe but coarser aerosols (>PM 3) contributed 66% of the difference between LFe and DFe (LFe-DFe). The increasing trend of the difference with increasing sizes indicates that the residence time of coarse aerosol particles and their interaction with Fe-ligands are critical factors deciding the total fluxes of LFe in the ocean. Considering the deposition velocities of each size of aerosols, the averaged fluxes of aerosol Fe of the fine and coarse aerosols were 1.8 and 5.9 nmol m^{-2} d^{-1} for DFe; and 2.8 and 62 nmol m^{-2} d^{-1} for LFe in the East China Sea, respectively. Attributed to the relatively low deposition velocities of fine aerosols, we found that either single or two averaged deposition velocities (fine/coarse) that were used in most of the previous studies would significantly overestimate soluble Fe fluxes in regions where the contribution of fine anthropogenic aerosols is dominant, such as the open ocean. In conclusion, this study demonstrates that aerosol sizes are essential and powerful parameters to accurately estimate the solubility and the fluxes of aerosol soluble Fe.

doi:10.6342/NTU202302200

3.1 Introduction

Since iron (Fe) is a major limiting micronutrient for phytoplankton growth in the large area of the global ocean, Fe supply in the euphotic zone may affect the oceanic biological pump and global carbon cycling (Martin, 1990; Martin and Fitzwater, 1988). Aerosol deposition is a major process supplying external Fe to the euphotic zone of the surface ocean so that the quantification of aeolian bioavailable Fe supply in the surface water is crucial to study biological pump and material cycling in the ocean (Jickells et al., 2005; Tagliabue et al., 2017). Aerosol dissolvable Fe is generally considered to be bioavailable to marine phytoplankton (Raiswell and Canfield, 2012). However, the quantification of aerosol dissolvable Fe in the euphotic zone of the ocean is a highly challenging task operationally, attributed to the extremely complicated atmospheric and aquatic physicochemical processes and reactions involved in aerosol transport and the post-deposited phase transformation of aerosol soluble Fe in the surface water (Meskhidze et al., 2019).

The lack of a standard methodology for assessing aerosol dissolvable iron is a major challenge (Meskhidze et al., 2019). Aerosol soluble or bioavailable Fe can be separated into two fractions, dissolved Fe (DFe) and labile Fe (LFe). Operationally, DFe is defined as instantly dissolved aerosol Fe in pure water or seawater that passes through 0.2 μm filter (Buck et al., 2006); LFe stands for buffer or acid leached Fe to present for Fe release from aerosols in rainwater (Baker et al., 2006; Sarthou et al., 2003) or Fe-ligand complexed fraction that may be bioaccessible (Perron et al., 2020b). DFe and LFe can thus be referred to the lower and upper limits of bioavailable aerosol Fe post-deposited in the surface ocean, respectively (Perron et al., 2020b), and the comparison of DFe and LFe fractions among different studies would require standardized leaching protocols. However, previous studies on the measurement of aerosol Fe solubility have used various leaching methods with different extraction solutions, pH, or leaching time et al. Large discrepancies of the solubility of DFe and LFe are observed. Baker et al. (2016) recommended using a common reference aerosol material to decide the solubilities (Arizona Test Dust or ATD, Powder Technology Inc.). Perron et al. (2020b) proposed a 3-step leaching protocol combining commonly used approaches to obtain DFe and LFe in aerosols, in which DFe is obtained by super pure water instant leach and LFe is by soaking aerosol samples in 1.1 M ammonia acetate buffer solution at pH 4.7 for 1 hr to mimic Fe-ligand complexation. For future studies, it is necessary to

doi:10.6342/NTU202302200

measure the solubilities of DFe and LFe in aerosol Fe studies by using comparable approaches.

Sampling aerosols across a range of sizes is an additional challenge. Although aerosol size is a critical factor reflecting the sources and influencing the deposition velocities, limited studies reported size-fractionated information in marine aerosol field observations (Baker et al., 2020; Buck et al., 2010; Gao et al., 2020; Kurisu et al., 2016b; Sakata et al., 2018; Yang et al., 2020), mainly due to the limited sampling time to obtain sufficient masses in cruises. On the other hand, relatively long aerosol sampling time may encounter highly varying meteorological conditions, which may introduce uncertainty for flux estimates. The estimates of aerosol Fe deposition fluxes of previous studies have been mostly based on bulk aerosol Fe concentrations and fixed average deposition velocity (Buck et al., 2013; Hsu et al., 2010; Perron et al., 2020a). The deposition velocities used to estimate aerosol Fe fluxes are generally oversimplified and may introduce large uncertainties (Duce et al., 1991). As pointed out by Foret et al. (2006), increasing the number of size bins would significantly increase the accuracy of the estimate of the fluxes. Moreover, aerosol sizes may reflect their sources. For example, size-fractionated aerosols exhibited significantly different Fe solubilities and composition (Kurisu et al., 2016b). As far as we know, the effects of aerosol sizes on the solubilities and the deposition fluxes of aerosol Fe have not been systematically studied in the surface ocean.

Right next to mainland China, the East China Sea receives a large amount of fine anthropogenic and coarse lithogenic aerosols from the continent, serving as an excellent sampling region for the size study. Selecting two islets in the marginal sea, we have systematically investigated DFe and LFe solubilities among five different size-fractionated dry aerosols collected at two islets in the oceanic region for one year by following the standard protocols proposed (Perron et al., 2020b). We have also evaluated the discrepancy of the deposition fluxes caused by using different deposition velocities of aerosols. The findings of this study shall provide insights for the impacts of aerosol sizes on the solubility and the fluxes and how to obtain a more accurate estimate of the deposition fluxes of aerosol dissolvable Fe regionally and globally.

3.2 Method

3.2.1 Sampling sites and method

Size-fractionated aerosol samples were collected on polytetrafluoroethylene (PTFE) filters (TE-230-PTFE, Tisch Environmental Inc., US) by using a high volume air sampler (TISCH Environmental Inc., US, MODEL-TE-5170) with a cascade impactor (TISCH Environmental Inc., US, Series 235) on the roofs of buildings in Matsu Island (26.17°N; 119.92°E; with height about 6 m above the ground) and Pengjia Islet (25.63°N; 122.08°E; with height about 6 m above the ground) from September 2019 to August 2020 (Fig. 3.1). The flow rates of the samplers were calibrated once per month, and the averaged flow rates were 1.0 ± 0.1 m^{-3} min^{-1}. The sampling sites of Matsu Island and Pengjia Islet are abbreviated as MT and PJ in the text hereafter, respectively. MT station is close to mainland China, only about 19 km from Fujian province, with area to be 30 km^2 and population to be 12,700. On the other hand, mainly composed of igneous minerals, PJ station is a small islet with area to be 1.1 km^2 and about 66 km from the northernmost of Taiwan (Fig. 3.1). Except governmental staff who carry out routine meteorological monitoring, there are no anthropogenic activities on PJ, which would thus be ideal to serve as a representative aerosol sampling site for the East China Sea. Monthly aerosol samples were obtained by collecting dry aerosols for 7~8 days continuously in each month, but not included the months of September, December, January, and July for MT and October and November for PJ due to temporary breakdown and regular maintenance of the samplers. The cascade impactor separated aerosols into five size fractions, the size cut-offs including stage 1, 7.3 μm; stage 2, 3.1 μm; stage 3, 1.6 μm; stage 4, 1.0 μm; and stage 5, 0.57 μm (Table 3.1). To simplify some of the discussion for size fractions, we have separated the five fractions into coarse and fine modes by using 3 μm as the cut-off. Fine and coarse aerosols mentioned in this study refer to $PM\leq3$ (the sum of sizes 0.57, 1.0, and 1.6 μm) and $PM>3$ (the sum of sizes 3.1 and 7.3 μm), respectively (Table 3.1). Sampling filters were freeze-dried and weighed at constant humidity before and after sampling. The filters with aerosols were then stored in a $-20^{o}C$ freezer before further chemical processes. It should be noted that $PM\leq3$ may still contain a small amount of lithogenic aerosols and vice versa, although the two size fractions may be representative for anthropogenic and lithogenic aerosols in general. We would like to point out that the impactors did not produce equal distributions of particles across all 10 slots of the substrate. We have used the software ImageJ to quantify the relative proportion by the intensity of the grayscale image in each slot and to calculate the total concentrations of the whole filters.

3.2.2 Quantification of DFe, LFe, and TFe

All chemicals used in this study were ultra-high purity grade, including nitric acid, hydrochloric acid, hydrofluoric acid, ammonium hydroxide, and acetic acid (J.T. Baker). All of the laboratory procedures were carried out in a positive pressured class 5 cleanroom, either in a HEPA-filtered class 5 laminar flow bench or hood. Powder-free polyvinyl chloride (PVC) gloves were worn while handling samples. We followed the suggested protocols of the GEOTRACES Cookbook to carry out the cleaning procedures for storage vials and sample digestion (Cutter et al., 2017).

For leaching procedures, we have followed the protocols suggested by Perron et al. (2020b) and made some modifications. The fractions of dissolved (DFe), labile (LFe), and total Fe (TFe) concentrations in aerosols were defined by three different digestion and leaching protocols. The samples for the three fractions were obtained from different slots of filters. DFe was leached by 5 mL of ultrapure water (Millipore Elix plus Element purification system) with gentle shaking for 10 seconds, then filtered through a 13 mm pre-acid washed polypropylene syringe filter with 0.2 μm hydrophilic PTFE membrane (Advantec) into a pre-acid washed 15 mL polypropylene vial (Buck et al., 2006). The LFe leach was processed using another aerosol filter soaked in 8 mL of ammonium acetate (1.4 M, pH 4.7) for 1 h. Then, the samples were centrifuged after removing the filter (Baker et al., 2006; Sarthou et al., 2003). The supernatant was collected by an autopipette for the quantification of target elements. TFe was obtained by digesting aerosol samples using a freshly prepared mixture of 4M HF, 4M HCl, and 4M HNO_3 for 4 h at 120°C (Ohnemus et al., 2014). The blank concentrations were measured by processing new filters with same digestion procedures as samples. The concentration levels of almost all of the digested samples were at least two orders of magnitude higher than the blank value for TFe, DFe, and LFe, which were 0.13, 0.036, and 0.023 pmol m^{-3}, respectively (Table S3.1 & S3.2).

The leachates and digests were diluted by super ultrapure water to obtain the final concentration of 0.5M HNO_3 and with 1 ppb of indium as an internal standard. All of the samples were analyzed by a sector field high resolution ICP-MS (Element XR, Thermo Fisher Scientific). The detailed information of the analytical method, blank, precision, accuracy was reported in our previous studies (Ho et al., 2010; Wang et al., 2014). In brief, the isotopes of ^{115}In, ^{207}Pb and ^{208}Pb were determined at low resolution (M/ΔM~ 300), ^{27}Al, ^{32}S, ^{47}Ti, ^{49}Ti , ^{51}V, ^{31}P, ^{54}Fe, ^{56}Fe, ^{60}Ni, ^{61}Ni, and ^{115}In were analyzed at medium resolution (M/ΔM ~ 4000),

doi:10.6342/NTU202302200

and ^{23}Na, and ^{115}In were determined at high resolution (M/ΔM ~ 10000). Na and S were only determined in the dissolved fraction, and all other elements were determined in each fraction. We also used Arizona Test Dust (ATD, <3 µm, Powder Technologies Inc.) and NIES CRM No. 28 Urban Aerosols collected in Beijing (BJ, National Institute for Environmental Studies) as reference material for accuracy validation. The ratios of our measured value to the previously reported value for Arizona test dust were 92% (Al), 100% (Ti), 102% (V), and 97% (Fe) (Shelley et al., 2015); The ratios to the certified values for urban aerosol reference material, NIES CRM No. 28, were 92% (Al), 93% (Ti), 101% (V), 97% (Fe), 114% (Ni), and 99% (Pb) (Table S3.3). The concentrations and solubilities of DFe and LFe in these two reference materials were also reported in Table 3.2 for future comparison from other laboratories. The solubilities of DFe or LFe were calculated as the leached concentration ratios of either DFe or LFe to TFe concentrations.

3.2.3 The calculation of fluxes, enrichment factors, and non-sea-salt sulfur

We calculated the fluxes by multiplying size-fractionated aerosol Fe concentrations measured (TFe, DFe, or LFe) with their individual deposition velocities:

$$F_{dry} = \sum_{i=1}^{5} C_{Fe\_i} * V_{d\_i}$$

The term, C_{Fe_i}, refers to the concentrations of aerosol Fe measured in each size fraction, and V_{d_i} represents the dry deposition velocity of each size range. The velocity is a function of aerosol sizes and atmospheric conditions, which are mainly decided by wind speed, relative humidity, and sea surface temperature. Since the relative humidity were extremely high at the sampling sites (Table S3.4), we have calculated the velocities of size-fractionated aerosols by assuming humidity equilibrium condition. Meteorological data of the sampling sites were obtained from the reports of the Weather Bureau of Taiwan (https://e-service.cwb.gov.tw/, Table S3.4) and the velocities were calculated by using the model proposed previously (Quinn and Ondov, 1998; Slinn and Slinn, 1980). The velocities estimated are comparable to the value estimated by a recent study (Emerson et al., 2020).

The enrichment factors (EF) of some specific metals, such as Pb and V, are useful indicators to distinguish anthropogenic aerosols from natural lithogenic dusts (Jickells et al., 2016; Shelley et al., 2017; Sholkovitz et al., 2009). Titanium (Ti) has been shown to be a more reliable proxy to present the mass of upper or bulk continental crust than Al (Lam et al., 2015). The EF presented in this study would be calculated by the total mass ratios of the metals to Ti measured in aerosols divided by the ratio of the upper continental crust (UCC):

$$EF_{Pb} = (\text{Metals/Ti})_{aerosol} / (\text{Metals/Ti})_{UCC}$$

The term, $(\text{Metals/Ti})_{UCC}$, is the reference value of the upper continental crust cited from Hu and Gao (2008).

Acidic conditions on aerosol surfaces in the atmosphere solubilize mineral Fe in aerosol particles (Meskhidze et al., 2003; Zhu et al., 1992). Aerosol acidity is mainly decided by the concentrations of SO_2, NO_x, and NH_3 and its aeolian transport processes (Baker et al., 2021). Buck et al. (2006) found the acidity of the aerosol samples has a significant correlation with the concentrations of soluble Fe in the North Western Pacific Ocean (NWPO) and non-sea-salt (nss-) sulfate is the major acidity contributor. Indeed, nss-sulfate accounts for a major fraction of aerosol acidity in our studied region. Normalized to nitrate acidity, the molar ratios of the acidities of nss-sulfate and ammonium were 2.5 and 2.3 in the East China Sea, 2.8 and 2.1 at Cape Fuguei station, and 5.5 and 3.9 at Penghu (Chou et al., 2008; Hsu et al., 2010), respectively. Although the acidity from nss-sulfate cannot represent total aerosol acidity, it is a good proxy for the variations of total aerosol acidity in our studied region. In this study, we have measured Na and total S and assume that nss-S is mainly from nss-sulfate and the concentrations were calculated by subtracting the sulfate contribution from sea salt to the aerosols:

$$[\text{nss-S}] = [\text{S}] - [\text{Na}] \times (\text{S/Na})_{seawater}$$

The terms, [S] and [Na], are the dissolved concentrations of sulfur and sodium measured by ICPMS, and $(\text{S/Na})_{seawater}$ stands for the molar ratio of S to Na in seawater, which is 0.060.

3.3 Result and Discussion

3.3.1 The distribution patterns of aerosol Fe concentrations

The prevailing seasons of northeastern (NE) and southwestern(SW) monsoons in our studied region are October to April and May to September, respectively. We found that the contribution of anthropogenic type elements (e.g., Pb or V) was generally higher in the NE monsoon period than in the SW period (Fig. S3.1 & S3.2). The ratios of EF_{Pb} and EF_V

between the NE and SW seasons ranged from 2.2 to 4.8 and from 1.3 to 2.9-fold at PJ, respectively, generally showing decreasing ratios with increasing sizes. The ratios for EF_{Fe} were 1.4, 1.0, 1.1, 1.2, and 1.1-fold for the aerosols from the smallest to the largest. As the seasonal variations of Fe were insignificant for most of the size fractions, the seasonality was not discussed in this study.

Generally, the masses of fine aerosols were less than coarse aerosols, with average values to be 15 and 19 μg m^{-3} at MT and 11 and 25 μg m^{-3} at PJ (Table S3.6), respectively. As expected, the concentrations of total aerosol Fe generally increased with increasing particle sizes for the two sampling stations for almost all of the sampling time. On average, the concentrations were 531, 938, 1743, 3849, and 3097 pmol m^{-3} with increasing sizes at MT and 194, 368, 721, 1780, and 2368 pmol m^{-3} at PJ (Fig. 3.2, Table S3.7). The average TFe at MT was about twice that of PJ. Based on the 5-day air mass back trajectories (Fig. S3.1), the relatively high TFe observed for MT was probably attributed to the relative high percentage of the aerosol transport pathways close to eastern mainland China. However, the concentrations of DFe exhibit opposite patterns with aerosol sizes. On average, the concentrations of DFe were 121, 46, 9.0, 9.5, and 2.6 pmol m^{-3} at MT and 74, 27, 12, 9.3, and 3.6 pmol m^{-3} at PJ (Fig. 3.2, Table S3.7). The differences between TFe and DFe increased with increasing particle sizes for both stations and was up to 3 orders of magnitude for size 7.3 μm, showing that the coarse fraction accounts for most of non-instantly soluble Fe. The average concentrations of LFe were 116, 60, 30, 46, and 48 pmol m^{-3}, and 67, 36, 28, 38, and 42 pmol m^{-3} for MT and PJ, respectively (Fig. 3.2, Table S3.7). The concentration patterns of LFe were similar to DFe for size 0.57 and 1.0 μm but closer to TFe for size 1.6, 3.1, and 7.3 μm, indicating that dissolvable Fe in the fine fraction was mainly from DFe and dissolvable Fe in the coarse fraction was mainly from LFe.

3.3.2 The solubility of DFe and the sources

The solubilities of DFe decreased exponentially with increasing particle sizes for both stations in all months, ranging for almost 4 orders of magnitude (Fig. 3.2, Table S3.8). The solubilities ranged from 0.011 to 44% and from 0.012 to 74% for MT and PJ, respectively. On average, the solubilities were 25, 7.6, 0.87, 0.41, and 0.19 with increasing sizes at MT and 50, 9.3, 2.2, 0.77, and 0.19 at PJ (Fig. 3.2, Table S3.8).

Although both anthropogenic and lithogenic aerosols may have widely spanned size ranges, for most of the oceanic regions, anthropogenic aerosols account for a dominant fraction in fine aerosols (Matsui et al., 2018). Aerosol sizes may thus reflect their sources (Mead et al., 2013) and aerosol Fe solubilities. For example, Schroth et al. (2009) reported that Fe solubility was 0.04% in African dust but was up to 81% in oil fly ash. The enrichment factor of Pb has been used to evaluate the contribution of anthropogenic and lithogenic aerosols in many previous aerosol studies (Jickells et al., 2016; Shelley et al., 2017). In this study, we found that the overall DFe solubility was linearly correlated with EF_{Pb} for both stations in this study (Fig. 3.3). The solubility increased from 0.011 to 74% with EF_{Pb} ranging from 1.5 to 1067 (Fig. 3.3, Table S3.9). We also found that the solubility variations within the same size fraction may be up to 1 to 2 orders of magnitude. The variations are positively associated with EF_{Pb} in most of the fractions. For example, the solubility of size 0.57 μm in MT varied from 0.011 to 0.80 with EF_{Pb} increased for about one order of magnitude. In brief, highly associated with the size spectrum and EF_{Pb}, the wide range of the Fe solubilities appears to be associated with the relative contribution of lithogenic and anthropogenic aerosols, suggesting that the two end member physical mixing of lithogenic and anthropogenic aerosols decides the patterns of DFe solubility (Fig. 3.3).

We have also found that the distribution of DFe and LFe solubilities with EF_{Pb} exhibits a significant spatial difference between MT and PJ but the distribution patterns with EF_V and TFe normalized non-sea-salt sulfur (nss-S) are comparable (Fig. 3.4). As V serves as a representative metal in heavy oil, the comparable results indicate that the source of aerosols with highly dissolvable Fe and high nss-S are associated with heavy oil burning. Moreover, the distribution of DFe solubility and TFe normalized nss-S exhibits the highest correlation among EF_{Pb}, EF_V, and the TFe normalized nss-S, spanning over 4 orders of magnitude among the 5 size fractions, in comparison to the 2 and 3 orders of magnitude for EF_V and EF_{Pb}, respectively. The strong correlation suggests that the acidity may promote aerosol Fe solubilities in the size-fractionated aerosols.

3.3.3 The solubility of LFe and the sources

The distribution patterns of LFe solubility exhibit partial dissimilarities with DFe, with a much higher value for the coarse fraction but a relatively comparable value for the fine fraction (Fig. 3.2). The solubilities ranged from 0.50 to 39% and from 0.78 to 59% for MT

doi:10.6342/NTU202302200

and PJ stations, respectively. On average, the solubilities were 24, 8.2, 2.4, 1.6, and 2.0 at MT and 42, 12, 4.8, 2.8, and 2.4 at PJ from size 0.57 to 7.3 μm, respectively (Table S3.8).

The overall labile solubilities were also linearly correlated with EF_{Pb} for both stations, generally showing increasing solubilities and EF_{Pb} with decreasing sizes (Fig. 3.3). Limited studies have focused on investigating the causes on the differences between LFe and DFe. Using the same buffer dissolution treatment, Perron et al. (2020b) reported that LFe solubility was 1.4-fold of DFe solubility in total suspended aerosol particles. Using a weak and a strong Fe binding ligand-solution treatment for 1 day, Clough et al. (2019) observed 1.5 and 1.7-fold of DFe solubility, respectively. The LFe solubilities observed in these two studies using bulk aerosols were comparable to our whole size result, 1.9±1.0 (Table S3.8). All of these previous studies have used total suspended aerosols to carry out the leaching experiments so that the effects of different leaching treatments on lithogenic and anthropogenic aerosols remain unknown. To the best of our knowledge, the differences between DFe and LFe solubilities have not been systematically investigated among size-fractionated aerosols. Our results show that the coarser the sizes the differences of the solubilities between DFe and LFe are larger. The differences were over one order of magnitude for size 7.3 μm, indicating the organic buffer can leach much more extra Fe in coarse aerosols than fine aerosols (Fig. 3.5). Comparable to the solubilities observed in the size 7.3 μm fraction of this study, the solubilities of LFe we measured in ATD reference material was 1.2%, which is also about two order of the magnitude higher than the solubility of DFe, which is 0.013% (Table 3.2). The coarse aerosols (>PM 3) contributed majorities of the difference between LFe and DFe masses, 70% for MT and 73% for PJ (Table S3.8).

In brief, fine anthropogenic aerosols would instantly release soluble Fe into seawater but lithogenic particles would need a relatively long time to leach dissolvable Fe to seawater by organic ligand complexion, presented by the buffer leach. The LFe availability would then depend on the capacity of organic ligands available in the water. Thus, the residence time of aerosol particles and the ligand capacity in seawater would be critical factors on deciding their Fe solubility. Perron et al. (2020b) proposed that the 1-hr buffer leaching protocol is based on the comparable solubility observation obtained by using strong ligand treatment for 24 hr (Clough et al., 2019). Kessler et al. (2020) reported that the solubilities of total suspended particles increased 2-fold from 1 to 8 days by using siderophore desferrioxamine-B

(DFOB) as Fe complexation ligand. Based on ^{234}Th and sediment trap data, Black et al. (2020) estimated that the residence time of 75% lithogenic aerosol particles in oceanic surface water range from 10 to 100 days. For future studies, long term laboratory leaching experiments may be required to better estimate the fluxes of LFe.

3.3.4 The fluxes of DFe and LFe and the overestimate

The deposition velocities of dry aerosols are known to be size dependent and may vary for a couple of orders of magnitude between fine and coarse aerosols (Slinn and Slinn, 1980). Generally, the velocities used range from 0.03 to 0.3 and from 0.3 to 3 cm s^{-1} for fine and coarse aerosols, respectively (Duce et al., 1991). As most of the previous studies did not carry out size-fractionated aerosol sampling, the dry aerosol Fe deposition fluxes were commonly estimated by multiplying concentrations of total aerosol Fe with an ‘averaged’ deposition velocity. For example, Buck et al. (2013) used 1.16 cm s^{-1} to calculate total and soluble aerosol Fe deposition fluxes in the Pacific Ocean.

Since the larger the sizes are, the higher the deposition velocities would be, the fluxes of coarse aerosols would be weighted more in comparison to concentrations (or masses) among different sizes. The weighting extents for the flux estimate would be dependent on the quantitative information of the masses for size-fractionated aerosols in TFe, LFe, and DFe. In terms of the masses of TFe, coarse aerosols accounted for 68% and 76% at MT and PJ, respectively. In terms of the fluxes, considering the deposition velocities of aerosol sizes, the contribution of coarse aerosols at MT and PJ would up to 97 and 98%, respectively. The averaged TFe fluxes were 3.8, 15, 94, 1286, and 2536 nmol m^{-2} day^{-1} at MT and 1.7, 6.2, 41, 875, and 2547 nmol m^{-2} day^{-1} at PJ for aerosols from size 0.57 to 7.3 μm (Fig. 3.6, Table S3.10), respectively. For the fluxes of LFe, the contribution of coarse aerosols becomes dominant, which were 94% and 95% at MT and PJ, respectively, in comparison to 31% and 38% on the masses. The LFe fluxes were 0.82, 0.93, 1.6, 15, and 39 nmol m^{-2} day^{-1} at MT and 0.59, 0.60, 1.6, 18, and 44 nmol m^{-2} day^{-1} at PJ from size 0.57 to 7.3 μm (Fig. 3.6, Table S3.10), respectively. For the fluxes of DFe, the contribution of fine aerosols decreased in comparison to the contribution on masses. In comparison to 6.4% of aerosol mass at MT and 10% at PJ, the contribution of coarse aerosols for the fluxes increased to 72% and 77% at MT and PJ, respectively, with averaged fluxes to be 0.85, 0.72, 0.49, 3.2, and 2.1 and 0.66, 0.45, 0.69, 4.5, and 1.4 nmol m^{-2} day^{-1} for MT and PJ from size 0.57 to 7.3 μm, respectively (Fig.

doi:10.6342/NTU202302200

3.6, Table S3.10). In brief, the quantitative information of the masses for each aerosol size is essential to obtain an accurate estimate on the fluxes.

Since the relative contribution of each size fraction on the masses of TFe, DFe, and LFe varies dramatically (Fig. 3.2), the averaged velocities calculated from the individual size in this study vary significantly among the three different fractions, TFe, LFe, and DFe, which were 0.45, 0.22, and 0.045 cm s^{-1} at MT and 0.76, 0.38, and 0.097 cm s^{-1} at PJ, respectively. Without knowing the relative contribution, single deposition velocity, which is commonly used in most of the published field studies, would cause significant bias for the flux estimates. For aerosol samples with a relatively high percentage of fine particles, a general single deposition velocity would tend to overestimate the fluxes of DFe due to their relatively high solubility but relatively low deposition velocity. Table 3.3 exhibits the fluxes estimated by using individually size-fractionated deposition velocities and the offsets from the fluxes estimated by either using fine and coarse averaged or total averaged velocities. In terms of dissolved fluxes, the value obtained by fine/coarse and total averaged velocities are 1.7- and 9.8-fold of the value obtained by 5 size-fractionated velocities at MT, and are 1.5- and 7.8-fold at PJ, respectively. In terms of labile Fe fluxes, the values were 1.02- and 2.0-fold at MT and 1.07- and 2.0-fold at PJ, respectively. The offset of the fluxes obtained by fine/coarse averaged velocity is significantly smaller than the one estimated by total averaged velocity. With the relatively high percentage of labile Fe in large aerosols, the value of labile Fe estimated by fine/coarse velocities is only 2 to 7% higher than the value estimated by size-fractionated velocity (Table 3.3). These results show that the information of aerosol size spectrum and their solubilities are essential to obtain reliable soluble Fe fluxes, particularly in the oceanic regions where fine anthropogenic aerosols are the dominant fraction.

3.3.5 Implications to the estimates of global Fe fluxes

Our study demonstrates that sufficient size-fractionated sampling is required to accurately estimate the fluxes of dissolved and labile aerosol Fe. Table 3.4 compiles the studies with the data of aerosol Fe concentrations and fluxes estimated by using different leaching protocols. Either in marginal seas or the open oceans, while only collecting total suspended particles, we found that the ratios of dissolved to total Fe concentrations are comparable to the ratios of their corresponding fluxes as an averaged deposition velocity, which tends to be weighted or biased by coarse fraction, was generally applied for their flux calculation. However, once five size-dependent deposition velocities are applied for the estimate, our data indicate that the flux ratios are only one-tenth of the concentration ratios (Table 3.4). In order to accurately estimate DFe or LFe fluxes, the deposition velocities used have to be size dependent. For studies without size-fractionated information, we suggest using fine aerosol deposition velocity to estimate dissolved Fe fluxes because dissolved Fe mainly originates from fine aerosols, with the exception for samples dominated by lithogenic particles in fine aerosols. For the estimate of LFe fluxes, both the solubilities of DFe and LFe should be determined. Then, two different velocities can be applied to estimate the fluxes: including the dissolved Fe fraction mainly from fine aerosols, [DFe], and the fraction between the labile and dissolved concentrations mainly from coarse aerosols, [LFe] - [DFe].

$$[LFe] = [DFe] + ([LFe] - [DFe])$$

$$F_{LFe} = [DFe] \times V_{d\_Fine} + ([LFe] - [DFe]) \times V_{d\_Coarse}$$

Where [LFe] and [DFe] stand for the concentrations of LFe or DFe; F_{LFe} refers to the flux of LFe; V_{d_Fine} and V_{d_Coarse} represent the dry deposition velocities of fine and coarse aerosols.

Only a few studies collected size-fractionated aerosols in large scale cross basin studies. Buck et al. (2010) surveyed DFe in the Northern Atlantic Ocean, and Gao et al. (2019) reported LFe solubility and fluxes in the Arctic Ocean. Both studies reported one kind of solubility only, either DFe or LFe. In addition, DFe stands for instantly dissolved aerosol Fe and LFe solubility is supposed to be closely associated with organic ligand availability in the surface water. While oceanic surface water receiving a large amount of aerosol input, organic ligands may be fully saturated by DFe, such as the pulse events of dust storms (Meskhidze et al., 2017). To fully understand Fe cycling mechanisms among dissolved Fe, abiotic and biotic particulate Fe in the surface ocean would rely on the information of dissolved and labile Fe fluxes, organic ligand concentrations, and particulate residence time. Thus, it is essential to measure both dissolved and labile Fe solubilities in size-fractionated aerosols in the global ocean.

In brief, the size-dependent distribution patterns of DFe, LFe, or TFe vary dramatically so that the averaged deposition velocities also vary significantly among the three pools in the East China Sea. We found that either single or two averaged deposition velocities that are used in most of the previous studies may significantly overestimate soluble Fe fluxes in

doi:10.6342/NTU202302200

regions with a significant contribution of fine anthropogenic aerosols. The findings of this study show that the size-fractionated sampling is critical for the estimate of aerosol dissolvable Fe fluxes for both DFe and LFe. Aerosol sizes are essential and powerful parameters to obtain a more accurate estimate for the solubility and the fluxes of aerosol soluble Fe.

doi:10.6342/NTU202302200

3.4 References

Baker, A.R., Jickells, T.D., Witt, M. and Linge, K.L., 2006. Trends in the solubility of iron, aluminium, manganese and phosphorus in aerosol collected over the Atlantic Ocean. Marine Chemistry, 98(1): 43-58 DOI: 10.1016/j.marchem.2005.06.004.

Baker, A.R. et al., 2021. Changing atmospheric acidity as a modulator of nutrient deposition and ocean biogeochemistry. Sci Adv, 7(28) DOI: 10.1126/sciadv.abd8800.

Baker, A.R. et al., 2016. Trace element and isotope deposition across the air-sea interface: progress and research needs. Philos Trans A Math Phys Eng Sci, 374(2081) DOI: 10.1098/rsta.2016.0190.

Baker, A.R., Li, M. and Chance, R., 2020. Trace Metal Fractional Solubility in Size-Segregated Aerosols From the Tropical Eastern Atlantic Ocean. Global Biogeochemical Cycles, 34(6) DOI: 10.1029/2019gb006510.

Black, E.E. et al., 2020. Ironing Out Fe Residence Time in the Dynamic Upper Ocean. Global Biogeochemical Cycles, 34(9) DOI: 10.1029/2020gb006592.

Buck, C.S., Landing, W.M. and Resing, J., 2013. Pacific Ocean aerosols: Deposition and solubility of iron, aluminum, and other trace elements. Marine Chemistry, 157: 117-130 DOI: 10.1016/j.marchem.2013.09.005.

Buck, C.S., Landing, W.M. and Resing, J.A., 2010. Particle size and aerosol iron solubility: A high-resolution analysis of Atlantic aerosols. Marine Chemistry, 120(1-4): 14-24 DOI: 10.1016/j.marchem.2008.11.002.

Buck, C.S., Landing, W.M., Resing, J.A. and Lebon, G.T., 2006. Aerosol iron and aluminum solubility in the northwest Pacific Ocean: Results from the 2002 IOC cruise. Geochemistry, Geophysics, Geosystems, 7(4) DOI: 10.1029/2005gc000977.

Chou, C.C.K. et al., 2008. Implications of the chemical transformation of Asian outflow aerosols for the long-range transport of inorganic nitrogen species. Atmospheric Environment, 42(32): 7508-7519 DOI: 10.1016/j.atmosenv.2008.05.049.

Clough, R., Lohan, M.C., Ussher, S.J., Nimmo, M. and Worsfold, P.J., 2019. Uncertainty associated with the leaching of aerosol filters for the determination of metals in aerosol particulate matter using collision/reaction cell ICP-MS detection. Talanta, 199: 425-430 DOI: 10.1016/j.talanta.2019.02.067.

Cutter, G. et al., 2017. Sampling and Sample-handling Protocols for GEOTRACES Cruises. 3 DOI: 10.25607/OBP-2.

Duce, R.A. et al., 1991. The atmospheric input of trace species to the world ocean. Global Biogeochemical Cycles, 5(3): 193-259 DOI: 10.1029/91gb01778.

Emerson, E.W. et al., 2020. Revisiting particle dry deposition and its role in radiative effect estimates. Proc Natl Acad Sci U S A, 117(42): 26076-26082 DOI: 10.1073/pnas.2014761117.

Foret, G., Bergametti, G., Dulac, F. and Menut, L., 2006. An optimized particle size bin scheme for modeling mineral dust aerosol. Journal of Geophysical Research, 111(D17) DOI: 10.1029/2005jd006797.

Gao, Y. et al., 2019. Particle-Size Variability of Aerosol Iron and Impact on Iron Solubility and Dry Deposition Fluxes to the Arctic Ocean. Sci Rep, 9(1): 16653 DOI: 10.1038/s41598-019-52468-z.

Gao, Y. et al., 2020. Particle-Size Distributions and Solubility of Aerosol Iron Over the Antarctic Peninsula During Austral Summer. Journal of Geophysical Research: Atmospheres, 125(11) DOI: 10.1029/2019jd032082.

Ho, T.Y., Chien, C.T., Wang, B.N. and Siriraks, A., 2010. Determination of trace metals in seawater by an automated flow injection ion chromatograph pretreatment system with ICPMS. Talanta, 82(4): 1478-84 DOI: 10.1016/j.talanta.2010.07.022.

Hsu, S.-C. et al., 2010. Sources, solubility, and dry deposition of aerosol trace elements over the East China Sea. Marine Chemistry, 120(1-4): 116-127 DOI: 10.1016/j.marchem.2008.10.003.

Hu, Z.C. and Gao, S., 2008. Upper crustal abundances of trace elements: A revision and update. Chemical Geology, 253(3-4): 205-221 DOI: 10.1016/j.chemgeo.2008.05.010.

Jickells, T.D. et al., 2005. Global iron connections between desert dust, ocean biogeochemistry, and climate. Science, 308(5718): 67-71 DOI: 10.1126/science.1105959.

Jickells, T.D., Baker, A.R. and Chance, R., 2016. Atmospheric transport of trace elements and nutrients to the oceans. Philos Trans A Math Phys Eng Sci, 374(2081) DOI: 10.1098/rsta.2015.0286.

Kessler, N., Kraemer, S.M., Shaked, Y. and Schenkeveld, W.D.C., 2020. Investigation of Siderophore-Promoted and Reductive Dissolution of Dust in Marine Microenvironments Such as Trichodesmium Colonies. Frontiers in Marine Science, 7 DOI: 10.3389/fmars.2020.00045.

Kurisu, M., Takahashi, Y., Iizuka, T. and Uematsu, M., 2016. Very low isotope ratio of iron in fine aerosols related to its contribution to the surface ocean. Journal of Geophysical Research: Atmospheres, 121(18): 11,119-11,136 DOI: 10.1002/2016jd024957.

Lam, P.J., Ohnemus, D.C. and Auro, M.E., 2015. Size-fractionated major particle composition and concentrations from the US GEOTRACES North Atlantic Zonal Transect. Deep Sea Research Part II: Topical Studies in Oceanography, 116: 303-320 DOI: 10.1016/j.dsr2.2014.11.020.

Martin, J.H., 1990. Glacial-interglacial CO_2change: The Iron Hypothesis. Paleoceanography, 5(1): 1-13 DOI: 10.1029/PA005i001p00001.

Martin, J.H. and Fitzwater, S.E., 1988. Iron deficiency limits phytoplankton growth in the north-east Pacific subarctic. Nature, 331(6154): 341-343 DOI: 10.1038/331341a0.

Matsui, H. et al., 2018. Anthropogenic combustion iron as a complex climate forcer. Nat

Commun, 9(1): 1593 DOI: 10.1038/s41467-018-03997-0.

Mead, C., Herckes, P., Majestic, B.J. and Anbar, A.D., 2013. Source apportionment of aerosol iron in the marine environment using iron isotope analysis. Geophysical Research Letters, 40(21): 5722-5727 DOI: 10.1002/2013gl057713.

Meskhidze, N., Chameides, W.L., Nenes, A. and Chen, G., 2003. Iron mobilization in mineral dust: Can anthropogenic SO2 emissions affect ocean productivity? Geophysical Research Letters, 30(21) DOI: 10.1029/2003gl018035.

Meskhidze, N., Hurley, D., Royalty, T.M. and Johnson, M.S., 2017. Potential effect of atmospheric dissolved organic carbon on the iron solubility in seawater. Marine Chemistry, 194: 124-132 DOI: 10.1016/j.marchem.2017.05.011.

Meskhidze, N. et al., 2019. Perspective on identifying and characterizing the processes controlling iron speciation and residence time at the atmosphere-ocean interface. Marine Chemistry, 217 DOI: 10.1016/j.marchem.2019.103704.

Ohnemus, D.C. et al., 2014. Laboratory intercomparison of marine particulate digestions including Piranha: a novel chemical method for dissolution of polyethersulfone filters. Limnology and Oceanography-Methods, 12(8): 530-547 DOI: 10.4319/lom.2014.12.530.

Perron, M.M.G. et al., 2020a. Origin, transport and deposition of aerosol iron to Australian coastal waters. Atmospheric Environment, 228 DOI: 10.1016/j.atmosenv.2020.117432.

Perron, M.M.G. et al., 2020b. Assessment of leaching protocols to determine the solubility of trace metals in aerosols. Talanta, 208: 120377 DOI: 10.1016/j.talanta.2019.120377.

Quinn, T.L. and Ondov, J.M., 1998. Influence of temporal changes in relative humidity on dry deposition velocities and fluxes of aerosol particles bearing trace elements. Atmospheric Environment, 32(20): 3467-3479 DOI: 10.1016/s1352-2310(98)00047-8.

Raiswell, R. and Canfield, D.E., 2012. The Iron Biogeochemical Cycle Past and Present. Geochemical Perspectives, 1(1): 1-220 DOI: 10.7185/geochempersp.1.1.

Sakata, K. et al., 2018. Custom-made PTFE filters for ultra-clean size-fractionated aerosol sampling for trace metals. Marine Chemistry, 206: 100-108 DOI: 10.1016/j.marchem.2018.09.009.

Sarthou, G. et al., 2003. Atmospheric iron deposition and sea-surface dissolved iron concentrations in the eastern Atlantic Ocean. Deep Sea Research Part I: Oceanographic Research Papers, 50(10-11): 1339-1352 DOI: 10.1016/s0967-0637(03)00126-2.

Schroth, A.W., Crusius, J., Sholkovitz, E.R. and Bostick, B.C., 2009. Iron solubility driven by speciation in dust sources to the ocean. Nature Geoscience, 2(5): 337-340 DOI: 10.1038/ngeo501.

Shelley, R.U., Morton, P.L. and Landing, W.M., 2015. Elemental ratios and enrichment factors in aerosols from the US-GEOTRACES North Atlantic transects. Deep Sea Research Part II: Topical Studies in Oceanography, 116: 262-272 DOI: 10.1016/j.dsr2.2014.12.005.

doi:10.6342/NTU202302200

Shelley, R.U. et al., 2017. Quantification of trace element atmospheric deposition fluxes to the Atlantic Ocean (>40°N; GEOVIDE, GEOTRACES GA01) during spring 2014. Deep Sea Research Part I: Oceanographic Research Papers, 119: 34-49 DOI: 10.1016/j.dsr.2016.11.010.

Sholkovitz, E.R., Sedwick, P.N. and Church, T.M., 2009. Influence of anthropogenic combustion emissions on the deposition of soluble aerosol iron to the ocean: Empirical estimates for island sites in the North Atlantic. Geochimica et Cosmochimica Acta, 73(14): 3981-4003 DOI: 10.1016/j.gca.2009.04.029.

Slinn, S.A. and Slinn, W.G.N., 1980. Predictions for particle deposition on natural waters. Atmospheric Environment (1967), 14(9): 1013-1016 DOI: 10.1016/0004-6981(80)90032-3.

Tagliabue, A. et al., 2017. The integral role of iron in ocean biogeochemistry. Nature, 543(7643): 51-59 DOI: 10.1038/nature21058.

Wang, B.S., Lee, C.P. and Ho, T.Y., 2014. Trace metal determination in natural waters by automated solid phase extraction system and ICP-MS: the influence of low level Mg and Ca. Talanta, 128: 337-44 DOI: 10.1016/j.talanta.2014.04.077.

Yang, T. et al., 2020. Solubilities and deposition fluxes of atmospheric Fe and Cu over the Northwest Pacific and its marginal seas. Atmospheric Environment, 239 DOI: 10.1016/j.atmosenv.2020.117763.

Zhu, X., Prospero, J.M., Millero, F.J., Savoie, D.L. and Brass, G.W., 1992. The solubility of ferric ion in marine mineral aerosol solutions at ambient relative humidities. Marine Chemistry, 38(1-2): 91-107 DOI: 10.1016/0304-4203(92)90069-m.

3.5 Figures

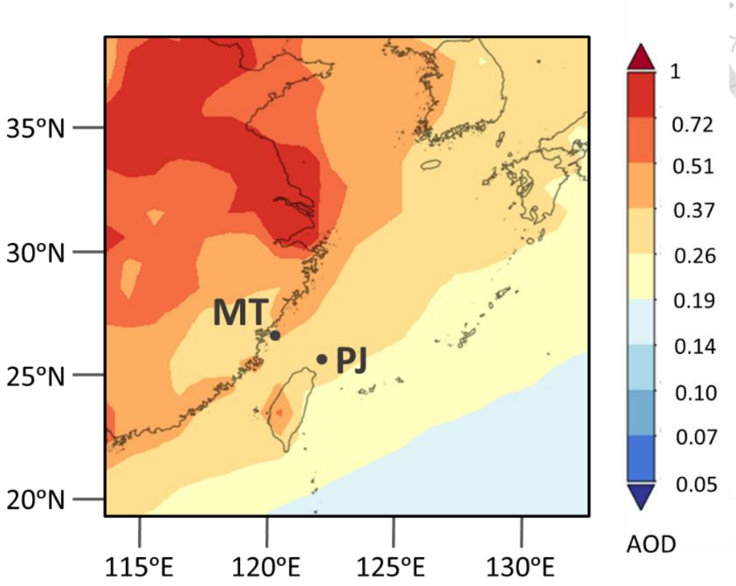

Figure 3.1. The location of the sampling stations, Matsu island (MT) and Penjia islet (PJ), and the decadal averaged aerosol optical depths from 2010 to 2020. The aerosol optical depth data were obtained by NASA Giovanni software (https://giovanni.gsfc.nasa.gov/giovanni/).

doi:10.6342/NTU202302200

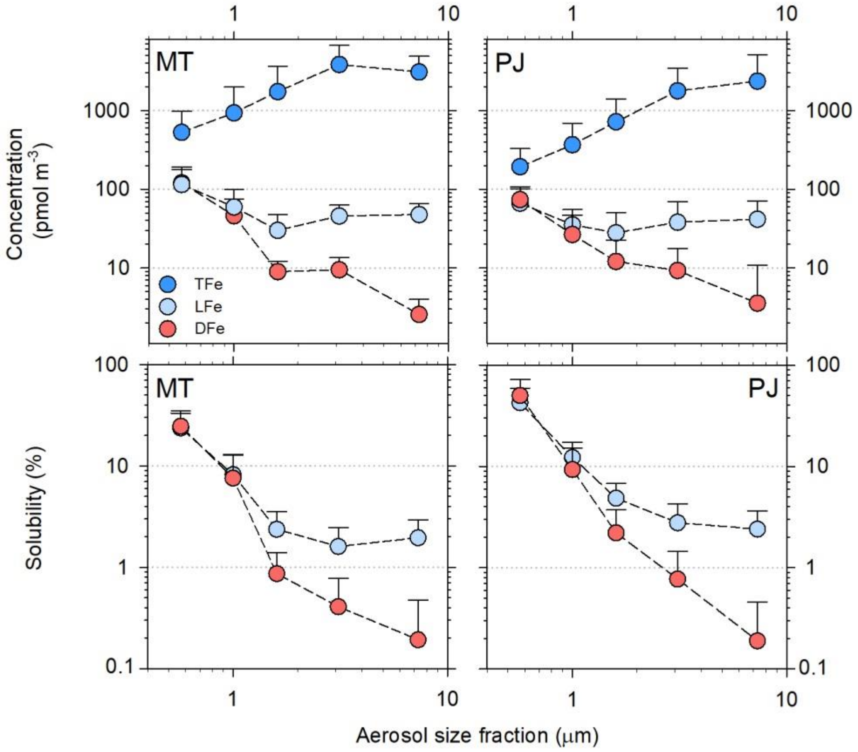

Figure 3.2. The averaged concentrations of DFe, LFe, and TFe and the solubility of DFe and LFe in the size-fractionated aerosols collected among different months at MT (left) and PJ (right). Red, light blue, and dark blue symbols stand for DFe, LFe, and TFe, respectively. The deviation bars stand for one standard deviation of all monthly data during the sampling period (Table S3.7 and S3.8).

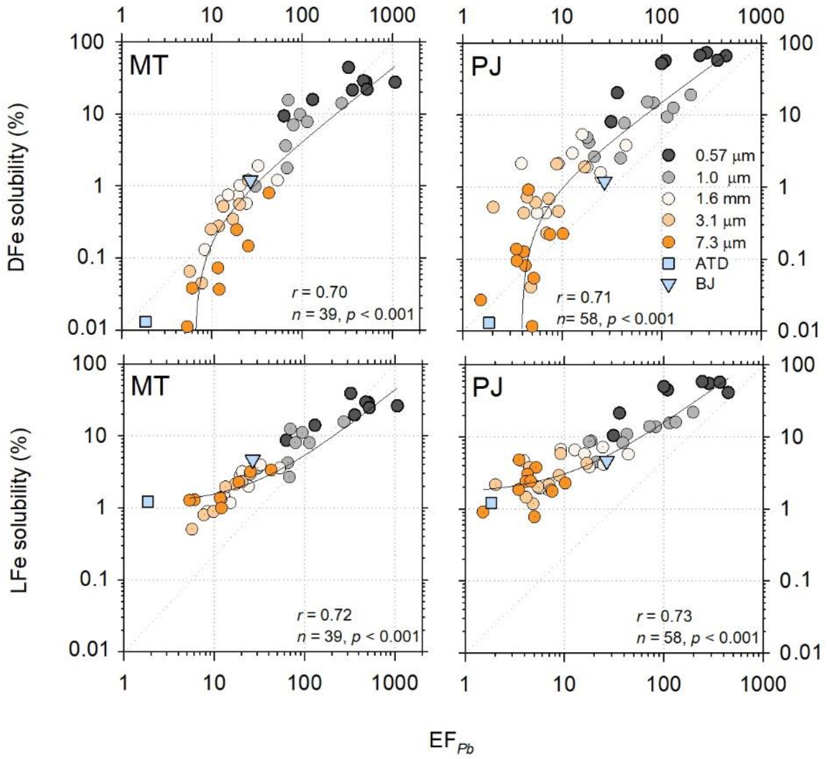

Figure 3.3. The comparison of the solubilities of DFe and LFe of the size-fractionated aerosols with the enrichment factor of Pb (EF$_{Pb}$) at MT (left) and PJ (right). The symbol colors are black for size cut-offs 0.57 µm, gray for 1.0 µm, white for 1.6 µm, light orange for 3.1 µm, and dark orange for 7.3 µm, respectively. ATD and BJ stand for the two reference materials, Arizona Test Dust (light blue square) and NIES CRM No. 28 Urban Aerosols collected in Beijing (light blue triangle), respectively. The solid lines in each plot stand for linear regression lines of the data.

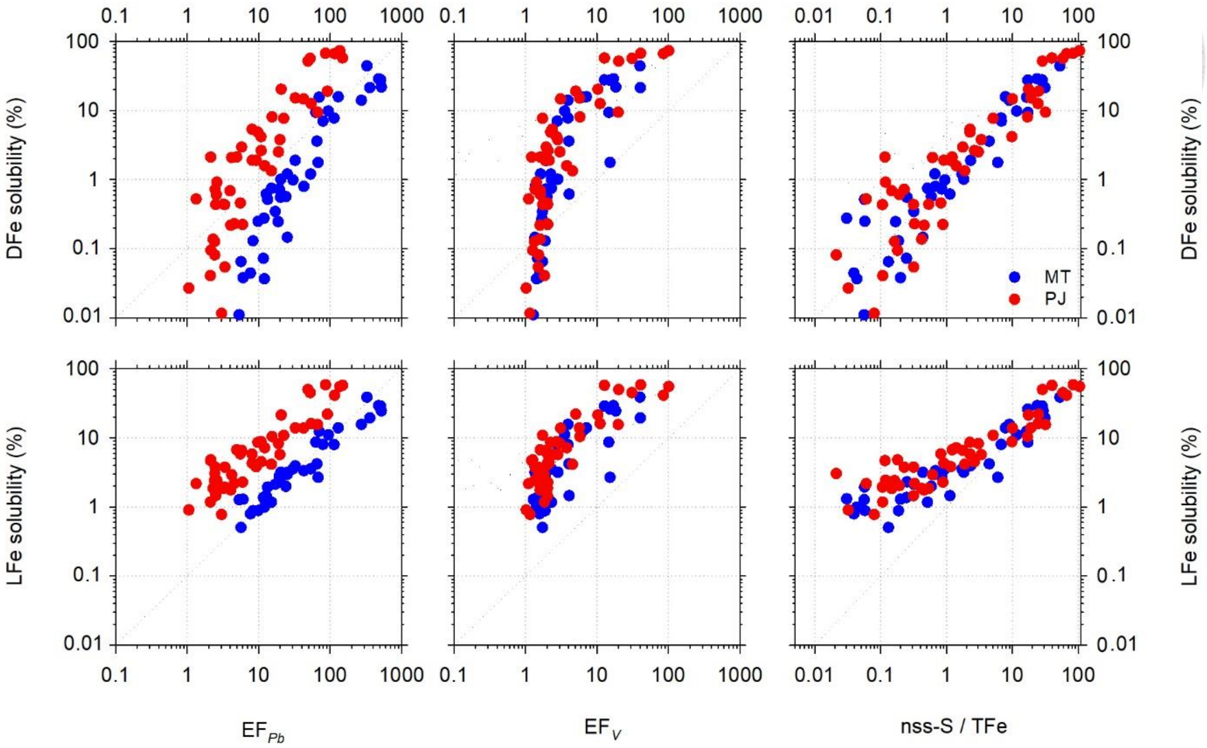

Figure 3.4. The comparison of DFe and LFe solubilities with EF$_{Pb}$, EF$_{V}$, and total Fe normalized nss-S among the two sampling sites. The blue circle refers to MT; the red circle refers to PJ. The term, nss-S/TFe, stand for TFe normalized nss-S.

doi:10.6342/NTU202302200

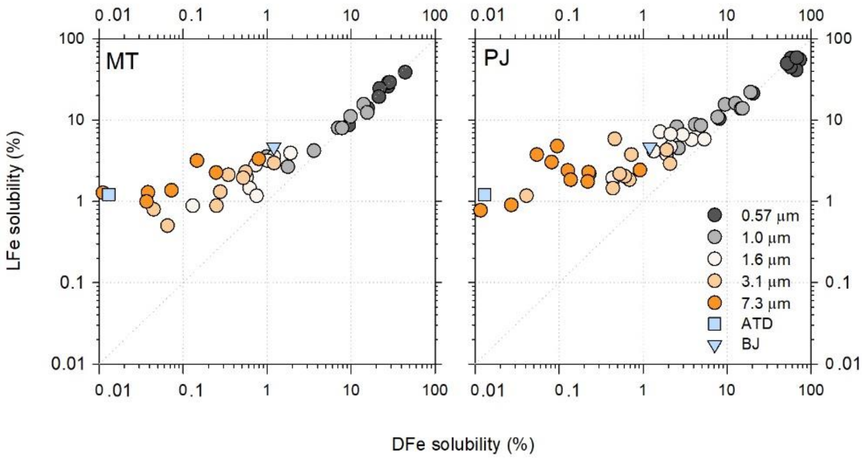

Figure 3.5. The comparison of DFe solubility with LFe solubility among size-fractionated aerosols at MT and PJ.

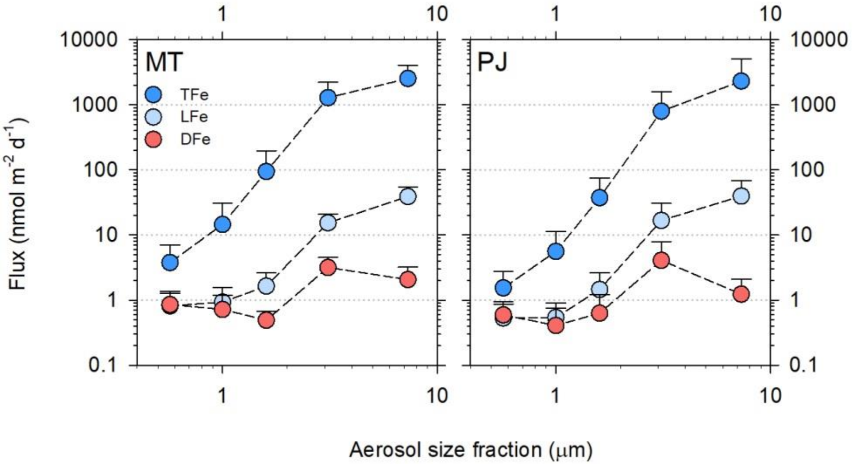

Figure 3.6. The comparison of the averaged fluxes of DFe, LFe, and TFe of the size-fractionated aerosols at MT and PJ (Table S3.10).

doi:10.6342/NTU202302200

3.6 Tables

Table 3.1. The information of the size cut-offs and size ranges of size-fractionated aerosols collected in this study.

Impactor stage	5	4	3	2	1
Size range (μm)	0.57~1.0	1.0~1.6	1.6~3.1	3.1~7.3	>7.3
Size cut-off (μm)	0.57	1.0	1.6	3.1	7.3

doi:10.6342/NTU202302200

Table 3.2. The concentrations and solubilities of DFe and LFe in the two reference materials, Arizona Test Dust (ATD) and NIES CRM No. 28 Urban Aerosols (BJ).

Sample	n	Concentration (mg g^{-1})		Solubility (%)	
		DFe	LFe	DFe	LFe
Blank (ng)	5	1.7±1.1	2.1±1.5	—	—
ATD	3	3.8±0.7	347±13	0.013±0.002	1.2±0.1
BJ	3	351±29	1360±24	1.2±0.1	4.7±0.1

Table 3.3. Sensitivity test for the flux calculation of DFe and LFe by using different deposition velocities. The offset (%) is defined as the percentage of the difference (between the fluxes obtained by the two or single velocities and the fluxes obtained by the size-fractionated velocities) to the fluxes obtained by the size-fractionated velocities.

Sampling site	Velocity*	Fe flux (nmol m^{-2} day^{-1})			
		DFe	Offset (%)	LFe	Offset (%)
MT	Size-fractionated	50	0	241	0
	Fine & coarse avg	106	74	284	2
	Total avg	286	880	455	100
PJ	Size-fractionated	45	0	202	0
	Fine & coarse avg	81	46	234	7
	Total avg	220	680	368	102

* Size-fractionated velocities used for flux calculations from size cut-offs 0.57 μm to 7.3 μm were 0.008, 0.018, 0.063, 0.39, 0.94 cm s^{-1} at MT and 0.010, 0.019, 0.070, 0.59, 1.3 cm s^{-1} at PJ, respectively. The fine and coarse average velocities were 0.041 and 0.63 cm s^{-1} at MT and 0.046 and 0.98 cm s^{-1} at PJ, respectively. The total average velocity were 0.45 and 0.76 cm s^{-1} for MT and PJ, respectively.

doi:10.6342/NTU202302200

Table 3.4. The comparison of the concentrations and the deposition fluxes of TFe, DFe, LFe, and DFe/TFe in dry aerosols of this study and some of the previous studies.

Sampling	Size	Fe conc. (pmol m^{-3})			DFe/TFe	Fe flux (nmol m^{-2} day^{-1})			DFe/TFe
site	no.	TFe	DFe	LFe	(%)	TFe	DFe	LFe	(%)
MT, ECS	5	10,100	190	300	1.9	3,920	7	58	0.19
PJ, ECS	5	5,400	130	210	2.4	3,150	7	59	0.22
NWPO[a]	2	355	12	n.a.	3.4	265	4	n.a.	1.6
YECS[b]	11	9,700	620[#]	n.a.*	6.4	8,380	466[#]	n.a.	5.6
NWPO[b]	9	2,080	110[#]	n.a.*	5.3	890	52[#]	n.a.	5.8
NWPO[c]	1	460	44	n.a.	9.6	461	44	n.a.	9.5
NEPO[c]	1	164	13	n.a.	7.9	165	13	n.a.	7.9

[abc] The data are from the studies of Kurisu et al. (2021), Yang et al. (2020), and Buck et al. (2013), respectively. High aerosol events are excluded from the dataset of Buck et al. (2013).

* n.a.: not available

[#] The samples were ultrasonically extracted in Milli-Q for 40-minute.

doi:10.6342/NTU202302200

3.7 Supplementary

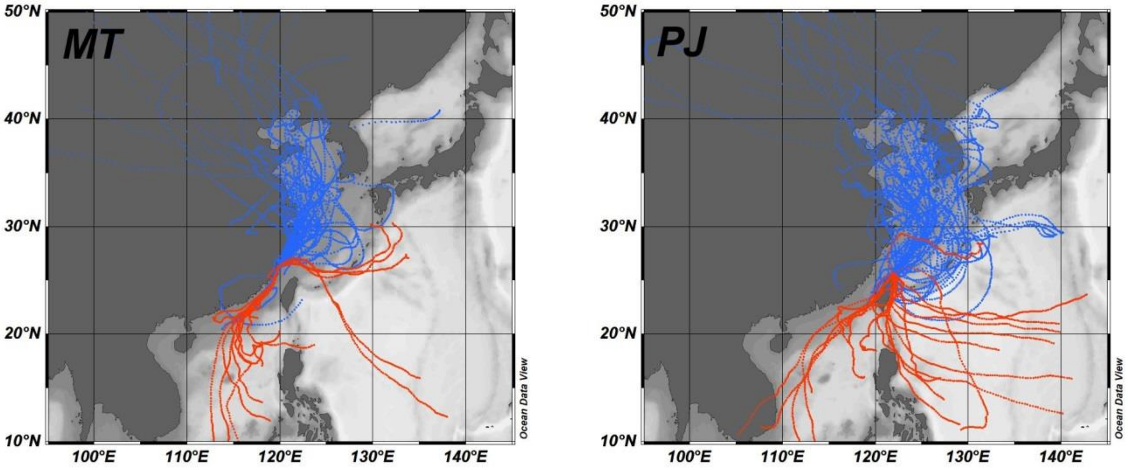

Figure S3.1. Air mass back trajectories for 5-day and 10-m height during the Northeastern (blue) and Southwestern (red) monsoon seasons of this study at MT and PJ.

doi:10.6342/NTU202302200

Table S3.1. The filter blank concentrations of some elements for the samples of TFe, DFe, and LFe (nmol per filter).

Blank	n	Concentration (nmol per filter)*							
		Na	Al	S	Ti	V	Fe	Ni	Pb
TFe	5	82	72	31	1.9	0.23	1.3	4.1	0.12
DFe	3	214	5	10	0.080	0.071	0.37	0.18	0.003
LFe	5	33	14	13	0.19	0.035	0.24	0.085	0.016

doi:10.6342/NTU202302200

Table S3.2. The air volume normalized blank concentrations of some elements for the samples of TFe, DFe, and LFe (pmol m^{-3}).

Blank	n	Concentration (pmol m^{-3})*							
		Na	Al	S	Ti	V	Fe	Ni	Pb
TFe	5	8.1	7.1	3.1	0.19	0.023	0.13	0.41	0.012
DFe	3	21	0.53	1.0	0.0085	0.0070	0.036	0.018	0.00034
LFe	5	3.3	1.4	1.3	0.019	0.0035	0.023	0.0085	0.0016

* The concentrations were obtained by using the total mass (pmol) of the blank in each filter divided by the total air volume for 7 days, 10,800 m^3.

doi:10.6342/NTU202302200

Table S3.3. The comparison of total elemental concentrations obtained in this study in the two reference materials, Arizona Test Dust (ATD) and NIES CRM No. 28 Urban Aerosols (BJ), with a previous study (Shelley et al. 2015) or the certified value.

Sample	n	Concentration (ng g^{-1})						Reference
		Al	Ti	V	Fe	Ni	Pb	
Acid blank (ng/vial)	6	10 ± 1	0.32 ± 0.10	0.057 ± 0.012	1.5 ± 0.3	0.34 ± 0.03	0.18 ± 0.06	This Study
ATD	5	69,600 ± 1,870	3,220 ± 50	72.7 ± 1.1	33,600 ± 500	n.a.*	n.a.	Shelley et
	9	66,800 ± 4,750	3,280 ± 250	74.4 ± 8.5	32,500 ± 2380	37.0 ± 7.1	32.3 ± 4.1	This study
BJ	6	46,400 ± 1,890	2,730 ± 125	73.7 ± 4.5	28,315 ± 1240	72.9 ± 4.9	397 ± 16	This study
Certified Value		50,400 ± 1,000	2,920 ± 330	73.2 ± 7.0	29,200 ± 1700	63.8 ± 3.4	403 ± 32	
Recovery		92%	93%	101%	97%	114%	99%	

*n.a.: data are not available.

doi:10.6342/NTU202302200

Table S3.4. The range and averaged value of monthly meteorological conditions during the sampling periods. The data were obtained from the Weather Bureau of Taiwan (https://e-service.cwb.gov.tw/HistoryDataQuery/index.jsp)

Sampling site	Date of sampling	Air pressure (hPa)	Air Temp. (K)	Relative humidity (%)	Wind speed (m s^{-1})	Wind direction (degree)	Precipitation (mm day^{-1})
MT	10/24-11/2/2019	1,017~1,021 (1,019)*	292~296 (294)	65~88 (73)	2.7~4.7 (3.8)	(38)	0.0~2.5 (0.43)
	12/24-31/2019	1,019~1,032 (1,023)	285~290 (287)	71~92 (82)	1.7~6.4 (3.6)	(31)	0.0~12 (1.6)
	2/24-3/2/2020	1,015~1,025 (1,020)	285~290 (287)	76~93 (84)	1.3~4.9 (3.0)	(11)	0.0~1.7 (0.21)
	3/25-4/1/2020	1,014~1,020 (1,017)	284~292 (288)	77~96 (87)	1.4~5.7 (3.0)	(13)	0.0~23 (5.5)
	4/27-5/4/2020	1,008~1,022 (1,015)	290~297 (294)	77~87 (83)	1.6~4.2 (2.7)	(274)	0.0~10 (1.5)
	5/24-31/2020	1,008~1,013 (1,011)	295~299 (297)	86~90 (88)	1.6~6.0 (2.7)	(7.5)	0.0~1.6 (0.65)
	6/24-7/1/2020	1,004~1,008 (1,006)	300~301 (301)	80~90 (84)	3.2~7.9 (6.8)	(205)	0.0~5 (0.6)
	8/25-9/1/2020	1,001~1,008 (1,004)	300~303 (301)	75~90 (85)	2.1~6.1 (3.9)	(151)	0.0~14 (3.6)
PJ	9/20-27/2019	1,002~1,019 (1,014)	297~298 (298)	62~84 (71)	5.5~16 (9.4)	(7.5)	0.0~14 (1.7)
	12/20-27/2019	1,017~1,024 (1,019)	288~293 (292)	66~92 (84)	3.3~10 (6.2)	(3.8)	0.0~9.3 (1.4)
	1/20-27/2020	1,012~1,025 (1,020)	288~295 (291)	67~92 (82)	3.7~11 (7.4)	(57)	0.0~39 (8.7)
	2/20-27/2020	1,019~1,028 (1,024)	291~295 (292)	66~88 (80)	4.1~9.1 (7.5)	(61)	0.0~7.0 (1.3)
	3/20-27/2020	1,014~1,017 (1,016)	293~297 (295)	76~89 (82)	4.5~8.4 (6.9)	(82)	0.0~0.8 (0.2)
	4/20-27/2020	1,015~1,021 (1,018)	290~296 (293)	59~91 (77)	5~11 (7.5)	(60)	0.0~7.0 (2.3)
	5/20-27/2020	1,004~1,011 (1,009)	295~299 (296)	89~100 (96)	4.5~10 (6.5)	(29)	0.0~51 (14)
	6/22-29/2020	1,006~1,010 (1,007)	302~303 (303)	81~85 (83)	3.1~9.0 (5.9)	(193)	0.0~0.5 (0.1)
	7/21-28/2020	1,008~1,012 (1,009)	302~303 (303)	80~89 (86)	4.2~7.1 (5.5)	(183)	0.0~0.0 (0.0)
	8/20-27/2020	1,002~1,011 (1,005)	300~303 (302)	83~92 (86)	4.6~14 (9.0)	(340)	0.0~4.3 (9.7)

*The numbers in brackets are monthly averaged value.

Table S3.5. The total masses of size-fractionated aerosols of each filter collected at MT and PJ.

Sampling site	Size (μm)	mass (mg)												Avg	SD
		2019				2020									
		Sep	Oct	Nov	Dec	Jan	Feb	Ma	Apr	Ma	Jun	Jul	Aug		
MT	0.57	n.a.	64	n.a.	73	n.a.	75	42	63	47	12	n.a.	36	52	22
	1.0	n.a.	74	n.a.	57	n.a.	71	33	39	48	41	n.a.	21	48	19
	1.6	n.a.	108	n.a.	53	n.a.	82	27	54	59	35	n.a.	34	56	27
	3.1	n.a.	215	n.a.	102	n.a.	117	50	106	101	99	n.a.	91	110	47
	7.3	n.a.	177	n.a.	89	n.a.	69	48	85	n.a.	110	n.a.	101	97	41
PJ	0.57	34	n.a.	n.a.	28	33	85	42	n.a.	29	24	24	19	35	20
	1.0	27	n.a.	n.a.	22	21	34	31	28	17	17	14	20	23	7
	1.6	44	n.a.	n.a.	32	31	55	47	47	28	37	23	36	38	10
	3.1	125	n.a.	n.a.	79	67	83	106	102	57	96	70	103	89	21
	7.3	215	n.a.	n.a.	142	97	53	110	175	78	130	80	134	121	49

*n.a.: data are not available.

Table S3.6. The mass concentrations of size-fractionated aerosols collected at MT and PJ.

Sampling site	Size (μm)	Concentration (μg m^{-3})													
		2019				2020								Avg	SD
		Sep	Oct	Nov	Dec	Jan	Feb	Mar	Apr	May	Jun	Jul	Aug		
MT	0.57	n.a.*	4.5	n.a.	6.5	n.a.	7.6	4.4	6.2	4.8	1.4	n.a.	3.4	4.8	1.9
	1.0	n.a.	5.2	n.a.	5.0	n.a.	7.2	3.4	3.9	4.8	4.9	n.a.	1.9	4.5	1.5
	1.6	n.a.	7.6	n.a.	4.6	n.a.	8.3	2.8	5.3	6.0	4.3	n.a.	3.1	5.2	2.0
	3.1	n.a.	15	n.a.	9.0	n.a.	12	5.2	10	10	12	n.a.	8.4	10	2.9
	7.3	n.a.	12	n.a.	7.8	n.a.	7.0	5.0	8.3	n.a.	13	n.a.	9.4	9.0	2.9
PJ	0.57	4.0	n.a.	n.a.	3.3	4.1	11	5.0	n.a.	3.6	3.2	2.2	1.8	4.2	2.6
	1.0	3.2	n.a.	n.a.	2.7	2.6	4.3	3.7	3.2	2.1	2.3	1.3	1.8	2.7	0.9
	1.6	5.2	n.a.	n.a.	3.8	3.9	6.9	5.5	5.5	3.5	5.0	2.1	3.4	4.5	1.4
	3.1	15	n.a.	n.a.	9.4	8.4	10	12	12	7.2	13	6.4	10	10	2.7
	7.3	26	n.a.	n.a.	17	12	6.7	13	20	10	18	7.3	12	14	6.0

*data not available.

Table S3.7. The concentrations of TFe, DFe, and LFe.

Item	Sampling site	Size (μm)	Fe concentration (pmol m^{-3})												Avg	SD
			2019				2020									
			Sep	Oct	Nov	Dec	Jan	Feb	Mar	Apr	May	Jun	Jul	Aug		
TFe	MT	0.57	n.a.	1,572	n.a.	626	n.a.	507	279	514	260	80	n.a.	405	531	455
		1.0	n.a.	3,468	n.a.	662	n.a.	897	257	901	365	410	n.a.	542	938	1,049
		1.6	n.a.	6,266	n.a.	1,068	n.a.	1,898	425	1,791	531	891	n.a.	1,07	1,743	1,902
		3.1	n.a.	10,585	n.a.	2,010	n.a.	3,481	915	4,368	2,752	3,975	n.a.	2,71	3,849	2,935
		7.3	n.a.	5,556	n.a.	1,511	n.a.	1,914	593	3,886	n.a.	4,633	n.a.	3,58	3,097	1,801
	PJ	0.57	115	n.a.	n.a.	117	124	381	259	n.a	105	443	126	72	194	135
		1.0	148	n.a.	n.a.	112	155	1,139	529	421	235	623	159	161	368	325
		1.6	287	n.a.	n.a.	157	246	2,099	1,033	482	489	1,758	371	284	721	685
		3.1	958	n.a.	n.a.	381	344	3,736	2,122	2,707	496	5,169	1,372	511	1,780	1,647
		7.3	3,914	n.a.	n.a.	985	354	1,388	1,922	2,633	374	9,694	1,733	685	2,368	2,798
DFe	MT	0.57	n.a.	249	n.a.	173	n.a.	141	80	113	115	7.5	n.a.	87	121	71
		1.0	n.a.	34	n.a.	93	n.a.	63	25	70	57	7.3	n.a.	20	46	29
		1.6	n.a.	8.2	n.a.	13	n.a.	14	8.1	10	5.4	5.5	n.a.	8.0	9.0	3.1
		3.1	n.a.	6.9	n.a.	11	n.a.	12	11	12	14	1.8	n.a.	6.8	9.5	4.1
		7.3	n.a.	2.1	n.a.	3.7	n.a.	2.8	4.7	2.8	n.a	0.51	n.a.	1.3	2.6	1.4
	PJ	0.57	85	n.a.	n.a.	78	59	31	149	n.a	60	90	66	49	74	34
		1.0	14	n.a.	n.a.	14	30	30	78	33	10	30	4.0	25	27	21
		1.6	3.9	n.a.	n.a.	2.5	9.3	9.2	20	14	2.1	37	7.9	15	12	11
		3.1	2.2	n.a.	n.a.	1.8	6.6	1.5	15	16	2.2	27	10	11	9.3	8.4
		7.3	0.45	n.a.	n.a.	0.54	0.80	1.1	2.4	24	0.51	2.6	1.6	1.5	3.6	7.3
LFe	MT	0.57	n.a.	220	n.a.	163	n.a.	147	81	126	101	6.9	n.a.	79	116	64
		1.0	n.a.	123	n.a.	104	n.a.	72	29	72	45	11	n.a.	23	60	40
		1.6	n.a.	55	n.a.	38	n.a.	53	17	36	17	13	n.a.	13	30	18
		3.1	n.a.	53	n.a.	46	n.a.	74	27	57	54	32	n.a.	24	46	17
		7.3	n.a.	72	n.a.	34	n.a.	61	20	53	n.a	59	n.a.	36	48	18
	PJ	0.57	64	n.a.	n.a.	48	52	40	149	n.a	47	95	63	42	67	35
		1.0	23	n.a.	n.a.	18	34	51	73	46	21	53	13	22	36	20
		1.6	12	n.a.	n.a.	11	14	39	40	32	9.5	82	25	16	28	22
		3.1	21	n.a.	n.a.	22	15	44	39	55	7.2	112	52	15	38	31
		7.3	30	n.a.	n.a.	37	8.1	42	46	64	6.9	88	83	12	42	29

Table S3.8. The solubilities of DFe and LFe.

Items	Sampling site	Size (μm)	Fe Solubility (%)													
			2019				2020								Avg	SD
			Sep	Oct	Nov	Dec	Jan	Feb	Mar	Apr	May	Jun	Jul	Aug		
DFe	MT	0.57	n.a.*	16	n.a.	28	n.a.	28	29	22	44	9.4	n.a.	22	25	10
		1.0	n.a.	1.0	n.a.	14	n.a.	7.0	10	7.8	16	1.8	n.a.	3.6	7.6	5.4
		1.6	n.a.	0.13	n.a.	1.2	n.a.	0.73	1.9	0.57	1.0	0.62	n.a.	0.75	0.87	0.53
		3.1	n.a.	0.07	n.a.	0.56	n.a.	0.35	1.21	0.28	0.52	0.04	n.a.	0.25	0.41	0.37
		7.3	n.a.	0.04	n.a.	0.25	n.a.	0.15	0.80	0.07	n.a.	0.01	n.a.	0.04	0.19	0.28
	PJ	0.57	74	n.a.	n.a.	67	48	8.1	58	n.a.	57	20	52	67	50	22.1
		1.0	9.5	n.a.	n.a.	13	19	2.6	15	7.7	4.2	4.9	2.5	15	9.3	5.9
		1.6	1.3	n.a.	n.a.	1.6	3.8	0.44	1.9	3.0	0.44	2.1	2.1	5.4	2.2	1.5
		3.1	0.23	n.a.	n.a.	0.46	1.91	0.04	0.69	0.61	0.44	0.53	0.73	2.09	0.77	0.68
		7.3	0.01	n.a.	n.a.	0.05	0.22	0.08	0.13	0.92	0.14	0.03	0.09	0.22	0.19	0.27
LFe	MT	0.57	n.a.	14	n.a.	26	n.a.	29	29	25	39	8.7	n.a.	19	24	9.5
		1.0	n.a.	3.5	n.a.	16	n.a.	8.0	11	8.0	12	2.7	n.a.	4.2	8.2	4.6
		1.6	n.a.	0.88	n.a.	3.6	n.a.	2.8	3.9	2.0	3.2	1.5	n.a.	1.2	2.4	1.2
		3.1	n.a.	0.50	n.a.	2.3	n.a.	2.1	3.0	1.3	1.9	0.80	n.a.	0.88	1.6	0.9
		7.3	n.a.	1.3	n.a.	2.3	n.a.	3.2	3.3	1.4	n.a.	1.28	n.a.	1.0	2.0	1.0
	PJ	0.57	55	n.a.	n.a.	41	42	10	58	n.a.	45	21	50	59	42	17
		1.0	16	n.a.	n.a.	16	22	4.5	14	11	8.8	8.6	8.3	14	12	5.1
		1.6	4.1	n.a.	n.a.	7.2	5.7	1.9	3.8	6.6	1.9	4.7	6.7	5.8	4.8	1.9
		3.1	2.2	n.a.	n.a.	5.9	4.3	1.2	1.8	2.0	1.5	2.2	3.8	2.9	2.8	1.5
		7.3	0.78	n.a.	n.a.	3.8	2.3	3.0	2.4	2.4	1.9	0.91	4.8	1.8	2.4	1.2

doi:10.6342/NTU202302200

Table S3.9. EF_{Pb} and EF_{V}.

Items	Location	Size	2019				2020								Avg	SD
		(μm)	Sep	Oct	Nov	Dec	Jan	Feb	Mar	Apr	May	Jun	Jul	Aug		
EF_{Pb}	MT	0.57	n.a.*	130	n.a.	1,0	n.a.	508	476	521	326	63	n.a.	359	431	308
		1.0	n.a.	30	n.a.	273	n.a.	80	94	113	70	68	n.a.	65	99	74
		1.6	n.a.	8.3	n.a.	53	n.a.	19	32	24	20	13	n.a.	15	23	14
		3.1	n.a.	5.7	n.a.	20	n.a.	17	25	12	13	7.7	n.a.	10	14	6.5
		7.3	n.a.	6.1	n.a.	19	n.a.	25	43	12	n.a.	5.3	n.a.	12	17	13
	PJ	0.57	284	n.a.	n.a.	446	818	31	367	n.a.	109	36	100	244	271	252
		1.0	114	n.a.	n.a.	132	197	21	83	43	19	18	39	72	74	59
		1.6	25	n.a.	n.a.	24	44	6.8	18	13	5.6	3.9	9.2	16	17	12
		3.1	7.0	n.a.	n.a.	9.2	17	4.8	7.4	5.4	4.1	2.0	4.4	8.8	7.0	4.2
		7.3	5.0	n.a.	n.a.	5.2	10	4.3	4.1	4.6	3.5	1.5	3.5	7.5	4.9	2.3
EF_{V}	MT	0.57	n.a.	7.1	n.a.	15	n.a.	13	17	18	40	15	n.a.	40	21	12
		1.0	n.a.	2.3	n.a.	3.9	n.a.	2.8	3.5	3.9	6.3	15	n.a.	4.1	5.2	4.1
		1.6	n.a.	1.9	n.a.	2.3	n.a.	1.9	2	2	2.8	4.1	n.a.	2.3	2.4	0.7
		3.1	n.a.	1.7	n.a.	1.9	n.a.	1.7	1.6	1.7	1.8	1.6	n.a.	1.7	1.7	0.1
		7.3	n.a.	1.5	n.a.	1.7	n.a.	1.4	1.4	1.5	n.a.	1.3	n.a.	1.4	1.5	0.1
	PJ	0.57	101	n.a.	n.a.	85	35	5.8	13	n.a.	31	10	20	41	38	34
		1.0	20	n.a.	n.a.	11	5.1	2.1	3.1	1.7	2.7	2.2	3.0	5.7	5.7	5.7
		1.6	4.6	n.a.	n.a.	3.8	2.8	2.0	1.9	2.0	1.8	1.2	1.6	2.4	2.4	1.1
		3.1	2.0	n.a.	n.a.	2.0	2.2	1.8	1.6	1.6	2.0	1.1	1.4	1.8	1.8	0.3
		7.3	1.2	n.a.	n.a.	1.5	2.1	1.5	1.3	1.4	1.6	1.0	1.3	1.6	1.5	0.3

Table S3.10. The deposition fluxes of TFe, DFe, and LFe.

Item	Sampling site	Size (μm)	Fe flux (nmol m^{-2} day^{-1})												Avg	SD
			2019				2020									
			Sep	Oct	Nov	Dec	Jan	Feb	Mar	Apr	May	Jun	Jul	Aug		
TFe	MT	0.57	n.a.	11	n.a.	4.7	n.a.	3.5	2.0	3.5	1.7	0.69	n.a.	2.9	3.8	3.3
		1.0	n.a.	54	n.a.	11	n.a.	14	4.1	14	5.5	6.6	n.a.	8.2	15	16
		1.6	n.a.	339	n.a.	60	n.a.	105	24	96	28	47	n.a.	56	94	103
		3.1	n.a.	3,434	n.a.	689	n.a.	1,172	310	1,424	906	1,483	n.a.	872	1,286	950
		7.3	n.a.	4,245	n.a.	1,244	n.a.	1,520	479	2,998	n.a.	4,492	n.a.	2,775	2,536	1,525
	PJ	0.57	1.2	n.a.	n.a.	1.0	1.2	3.6	2.3	n.a.	0.90	3.6	1.0	0.7	1.7	1.2
		1.0	2.6	n.a.	n.a.	1.9	2.7	20	8.8	7.2	3.9	10	2.5	2.7	6.2	5.6
		1.6	28	n.a.	n.a.	8.7	14.1	117	57	27	27	96	19	17	41	37
		3.1	710	n.a.	n.a.	176	178	2,062	939	1,308	223	2,328	494	332	875	787
		7.3	5,320	n.a.	n.a.	1,018	403	1,664	1,994	2,883	374	9,458	1,488	870	2,547	2,833
DFe	MT	0.57	n.a.	1.8	n.a.	1.3	n.a.	1.0	0.57	0.76	0.77	0.06	n.a.	0.62	0.85	0.51
		1.0	n.a.	0.53	n.a.	1.5	n.a.	1.0	0.40	1.1	0.85	0.12	n.a.	0.29	0.72	0.46
		1.6	n.a.	0.44	n.a.	0.72	n.a.	0.77	0.45	0.55	0.29	0.29	n.a.	0.42	0.49	0.18
		3.1	n.a.	2.2	n.a.	3.8	n.a.	4.1	3.8	3.9	4.7	0.66	n.a.	2.2	3.2	1.3
		7.3	n.a.	1.6	n.a.	3.1	n.a.	2.2	3.8	2.2	n.a.	0.50	n.a.	1.0	2.1	1.1
	PJ	0.57	0.86	n.a.	n.a.	0.68	0.55	0.29	1.3	n.a.	0.52	0.74	0.51	0.46	0.66	0.30
		1.0	0.25	n.a.	n.a.	0.24	0.51	0.52	1.3	0.55	0.16	0.48	0.06	0.41	0.45	0.34
		1.6	0.38	n.a.	n.a.	0.14	0.54	0.52	1.1	0.79	0.12	2.0	0.41	0.93	0.69	0.57
		3.1	1.6	n.a.	n.a.	0.81	3.4	0.84	6.5	8.0	1.0	12	3.6	6.9	4.5	3.8
		7.3	0.62	n.a.	n.a.	0.55	0.91	1.4	2.5	n.a.	0.52	2.6	1.4	1.9	1.4	0.8
LFe	MT	0.57	n.a.	1.6	n.a.	1.2	n.a.	1.0	0.58	0.85	0.67	0.06	n.a.	0.56	0.82	0.46
		1.0	n.a.	1.9	n.a.	1.7	n.a.	1.1	0.45	1.1	0.68	0.18	n.a.	0.34	0.93	0.63
		1.6	n.a.	3.0	n.a.	2.1	n.a.	2.9	0.93	1.9	0.90	0.69	n.a.	0.66	1.6	1.0
		3.1	n.a.	17	n.a.	16	n.a.	25	9.2	19	18	12	n.a.	7.7	15	5.6
		7.3	n.a.	55	n.a.	28	n.a.	48	16	41	n.a.	57	n.a.	28	39	16
	PJ	0.57	0.65	n.a.	n.a.	0.42	0.48	0.38	1.3	n.a.	0.41	0.77	0.49	0.40	0.59	0.30
		1.0	0.41	n.a.	n.a.	0.30	0.59	0.89	1.2	0.78	0.34	0.84	0.20	0.38	0.60	0.33
		1.6	1.2	n.a.	n.a.	0.63	0.81	2.2	2.2	1.8	0.53	4.5	1.3	1.0	1.6	1.2
		3.1	16	n.a.	n.a.	10	7.7	24	17	27	3.2	51	19	9.7	18	13
		7.3	41	n.a.	n.a.	38	9.2	51	48	70	6.9	86	71	15	44	27

Chapter 4

Contribution of anthropogenic and lithogenic aerosol Fe in the Northwestern Pacific Ocean: The evidence of elemental and isotopic composition

By

Chih-Chiang Hsieh[a,b] and Tung-Yuan Ho*[a,b]

[a] Institute of Oceanography, National Taiwan University, Taipei, Taiwan

[b] Research Center for Environmental Changes, Academia Sinica, Taipei, Taiwan

doi:10.6342/NTU202302200

4.0 Abstract

Aerosol deposition is a critical source providing Fe to the remote surface ocean. Anthropogenic aerosol with high solubility has been reported to be an important source suppling dissolvable or bioavailable Fe to marine phytoplankton. However, it is highly challenging to quantify the contribution of anthropogenic aerosol Fe (AN-Fe) to the ocean. In this study, we collected the size-fractionate aerosols in the East China Sea (ECS) and used Fe isotopic composition and specific elemental ratios to investigate the question. We found that the lowest δ^{56}Fe value was down to -3.4 ‰ in bulk marine aerosols, and the lowest δ^{56}Fe value for dissolved and labile Fe were -4.5 and -4.3 ‰, respectively, indicating that δ^{56}Fe end member of anthropogenic Fe is as low as -4.5 ‰ in East Asian An-Fe. Based on the strong association between δ^{56}Fe and some specific metal to Ti ratios, we confirmed that aerosol Fe in the ECS were mainly mixed by lithogenic and anthropogenic aerosols, and AN-Fe is mainly from high temperature combustion activities. For the three larger aerosol sizes (size cut-offs 1.6, 3.1, 7.3 μm), the variations of δ^{56}Fe (0.16 to -0.08‰) were too small to distinguish and quantify the contribution. Instead, we found that Cd/Ti ratio is a more sensitive tool to quantify the contribution of bulk AN-Fe in aerosols. When δ^{56}Fe data in aerosols is unavailable, Cd or Pb to Ti ratios may potentially be an alternative tool to quantify the contribution of AN-Fe. Based on the approaches, we found that AN-Fe contributed more than 50% of dissolved Fe concentrations during the NE monsoon seasons. However, since anthropogenic Fe is primarily from PM 1.0 aerosols, the deposition velocities of the small aerosols are much lower than lithogenic aerosols. Overall, lithogenic aerosol Fe is still the dominant Fe source for bulk, dissolved, or labile Fe in the oceanic region.

doi:10.6342/NTU202302200

4.1 Introduction

The quantification of anthropogenic aerosol Fe (AN-Fe) fluxes in the ocean is highly challenging due to the lack of suitable tools. The variation of enrichment of Fe can potentially be a tool, but the values among sources are relatively insignificant differences compared to other elements (Buck et al., 2019; Hsieh et al., 2023). Thus, some studies use EF_{Pb} or EF_{V} as indicators of Fe sources, but those parameters are not necessarily related to Fe sources. Instead, Fe isotopic composition may be a useful proxy to trace the sources of aerosol Fe and estimate the contribution of different sources since different aerosol Fe may possess specific isotopic values. The averaged δ^{56}Fe of lithogenic dust and loess are +0.1 ± 0.1 ‰ (Beard et al., 2003; Conway et al., 2019; Mead et al., 2013; Waeles et al., 2007), which are not significantly fractionated during transport processes and the average δ^{56}Fe of upper continental crust is 0.09 ± 0.03 ‰ (Gong et al., 2016). In terms of AN-Fe, the sources are relatively diverse, which may come from fossil fuel (e.g., coal and heavy oil) combustion, industry activities, and biomass burning. Fossil fuel with high temperature combustion can cause Fe isotope fractionation during evaporation and yield much lower δ^{56}Fe, as low as -3.2 ‰ (Kurisu et al., 2016). Similarly, temperature level in smelting activities like steel manufacturing processes is also extremely high, 1,000-2,000 ^{o}C, and δ^{56}Fe value in the emitted aerosols from smelting processes is reported to be relatively light, which is near -3.5 ‰ (Kurisu et al., 2019). The biomass burning aerosol Fe has no significant fractionation from lithogenic dust Fe. The combustion temperature of biomass burning is generally low, approximately 300-500 ^{o}C, and possibly result in limited isotopic fractionation (Kurisu and Takahashi, 2019). Assuming that aerosol Fe mainly comes from lithogenic dust and fossil fuel high temperature combustion, we may estimate the contribution of An-Fe flux to the ocean by the following two-component mixing model:

doi:10.6342/NTU202302200

$$\delta^{56}\mathrm{Fe}_{\mathrm{meaured}} = \delta^{56}\mathrm{Fe}_{\mathrm{dust}} \times f_{\mathrm{dust}} + \delta^{56}\mathrm{Fe}_{\mathrm{anthropogenic}} \times f_{\mathrm{anthropogenic}}$$

The terms of $\delta^{56}\mathrm{Fe}_{\mathrm{dust}}$ and $\delta^{56}\mathrm{Fe}_{\mathrm{anthropogenic}}$ stand for end member values of dust and the fossil fuel high temperature combustion aerosols, and f_{dust} and $f_{\mathrm{anthropogenic}}$ stand for the portion of aerosol source in the bulk aerosol. Kurisu et al. (2019) suggest the δ^{56}Fe range of high temperature combustion aerosols is -3.9 to -4.7 ‰, and indicated that aerosol Fe from combustion accounted for up to 50 % and 20 % in the air mass of fine and bulk (coarse + fine) aerosols in the Northwestern Pacific Ocean, respectively. Overall, An-Fe accounted for 33% in soluble Fe deposition flux. However, Pinedo-Gonzalez et al. (2020) assume the δ^{56}Fe range of AN-Fe is from -1.8 to -1.6 ‰, and reported that anthropogenic Fe contributes 21-59 % of dissolved Fe in the same oceanic region, the North Pacific Ocean (158°W from 35 to 40°N). The inconsistent δ^{56}Fe value of AN-Fe may introduce huge uncertainty for global aerosol Fe flux estimates by models. Further effort is needed to validate δ^{56}Fe value of AN-Fe in the oceanic region.

Previous studies have shown that Pb to Al ratio has a high correlation with δ^{56}Fe in the aerosol dissolved Fe in the North Atlantic Ocean, indicating light δ^{56}Fe is strongly influenced by anthropogenic activity (Conway et al., 2019). However, the δ^{56}Fe values in bulk aerosols are poorly correlated with EF of Pb and V in the Nroth Pacific Ocean. The poor correlation in the North Pacific Ocean may be due to different AN-Fe sources. If marine aerosol contains multiple anthropogenic sources, the δ^{56}Fe itself may not be enough to distinguish the sources with comparable values. Coupling δ^{56}Fe and elemental ratios may useful to distinguish the sources of aerosol Fe. For example, Ni or V in aerosols are known to be associated with oil combustion (Nriagu and Pacyna, 1988; Sholkovitz et al., 2009). K in fine aerosols is known to be an indicator for biomass and fossil fuel burning (Andreae, 1983). The elements, Cd, Zn, and Pb are also enriched in fossil fuel combustion processes (Nriagu and Pacyna, 1988). We plan to examine the correlation between these specific elements and δ^{56}Fe to evaluate the sources of An-Fe.

We collected the size-fractionated aerosols in the East China Sea (ECS), which receives large amounts of anthropogenic and lithogenic aerosols from mainland China during the Northwestern monsoon season and biomass burning aerosols from equatorial Southeast Asia during the Southwestern monsoon season (Fig. 4.1). The ECS thus provides an excellent platform to investigate the sources of different aerosol Fe. We applied both δ^{56}Fe and elemental ratios to estimate the contribution of different aerosol sources for total aerosol Fe and dissolvable Fe in mass and fluxes. The dissolvable Fe followed the standardized leaching protocols Perron et al. (2020) proposed, including dissolved Fe and labile Fe. The dissolved Fe is obtained by instantaneously passing ultrapure water through 0.2 or 0.45 μm aerosol filters (Buck et al., 2006; Morton et al., 2013). The labile Fe used ammonia acetate buffer solution at pH 4.7 to mimic aerosol metals dissolution processes by rainwater (Baker and Jickells, 2006; Sarthou et al., 2003) or short period complexation processes by seawater ligand (Perron et al., 2020). The findings of this study shall provide useful information for tracing An-Fe sources and estimating the deposition fluxes of dissolvable An-Fe regionally and globally.

4.2 Method

4.2.1 Sampling sites and method

The aerosol samples were collected in the small islet Pengjiayu (PJ, 1.1 km^2, 25.63°N, 122.08°E), which is located at 66 km from the northernmost of Taiwan (Fig. 4.1). Only limited governmental staff from the Taiwanese Coastal Guard Administration and Central Weather Bureau on the volcanic islet so that PJ serves as an ideal time series sampling site for

doi:10.6342/NTU202302200

the aerosol study in the Northwestern Pacific Ocean (NWPO). Size-fractionated aerosol samples were collected by polytetrafluoroethylene filters (TE-230-PTFE, Tisch Environmental Inc., US) which were installed on the high volume aerosol sampler (TISCH Environmental Inc., US, MODEL-TE-5170) and coupled with a cascade impactor (TISCH Environmental Inc., US, Series 235). The cascade impactor separated aerosols into five size fractions, including stage 1 (>7.3 μm), stage 2 (3.1-7.3 μm), stage 3 (1.6-3.1 μm), stage 4 (1.0-1.6 μm), and stage 5 (0.57-1.0 μm). The stage 3-5 and stage 1-2 aerosols are referred to as fine aerosols and coarse aerosols, respectively. The aerosol samples were distributed into 9-10 strings in each slotted impactor filter, and we carried out total digestion or leaching treatment by using one of the strings. To collect adequate masses for the isotopic composition analysis in different treatments, we continuously collected size-fractionated aerosols for 7-8 days on one filter every month from September 2019 to August 2020. The data are unavailable in October and November 2019 dued to the sampler being under maintenance. Each filter was freeze-dried and weighed before the sample collection or the chemical processes. Aerosol samples were stored in a -20^{o}C freezer before further chemical processes.

Seven-day air mass backward trajectory analysis was conducted by the Hybrid Single-Particles Lagrangian Integrated Trajectory (HYSPLIT) model (Air Resources Laboratory, NOAA, U.S.A.). Figure 4.1 showed the air mass transport pathways were completely opposite between northeastern monsoon (NE) season and southwestern monsoon (SW) season. The aerosols came from the north during the NE season from September 2019 to May 2020, and aerosols came from the south during the SW season from June 2020 to July 2020. In terms of aerosol samples collected in August 2020, there was a typhoon Maysak (category 4) passed by sampling location PJ and caused changes in wind direction. Thus, we exclude the samples from the SW season in this study.

doi:10.6342/NTU202302200

4.2.2 Quantification of dissolvable and total Fe concentration

Laboratory procedures while handling samples were carried out in an ISO Class 5 positive pressure cleanroom by wearing powder-free polyvinyl chloride (PVC) gloves. All acids and bases used for sample pretreatments were ultra-high purity grade, including nitric acid (HNO_3, J. T. Baker), hydrochloric acid (HCl, J. T. Baker), hydrofluoric acid (HF, J. T. Baker), acetic acid (CH_3COOH, J. T. Baker), ammonium hydroxide (NH_4OH, J. T. Baker). For cleaning procedures of digestion and storage vials, we followed the protocols suggested in the GEOTRACES Cookbook (Cutter et al., 2017).

Regarding the dissolvable fraction, we conducted two different leaching protocols, including instantaneous ultrapure water (dissolved), acetate buffer (labile). The dissolved aerosol Fe fraction was obtained by aerosol samples immersed in 5 mL of ultrapure water (> 18.2 MΩ.cm) with gentle shaking for 10 seconds. Leaching solution was then filtered particles through a 13 mm pre-acid washed 0.2 μm hydrophilic PTFE syringe filter (Advantec) and stored final solution into a pre-acid washed 15 mL polypropylene vial (Morton et al., 2013). Samples for labile aerosol Fe leach were soaked in 8 mL of ammonium acetate (1.4 M, pH 4.7) at room temperature for 1 h (Baker and Jickells, 2006). The total digested solution was freshly prepared mixed solution with 4M HF, 4M HCl, and 4M HNO_3 (Eggimann and Betzer, 1976). Samples for total digestion were heated for 4 h at 120°C (heater temperature) in 2ml of premixed digested solution. For buffer leach and total digestion, insoluble particles were removed by centrifuge after removing the filters (Baker and Jickells, 2006; Sarthou et al., 2003). The supernatant was dried up with open caps then redissolved dried samples in 10 ml 0.5 M HNO_3 solution at 120°C (heater temperature) with closed caps for 1 h for further concentration quantification. New filters were treated with the same leaching procedures as samples to obtain the filter blank. All of the leached or digested samples were diluted with 0.5

doi:10.6342/NTU202302200

M HNO_3 solution accordingly, then were analyzed by a sector field high resolution ICPMS (Element XR, Thermo Fisher Scientific). The detailed information of the analytical method, blank, precision, accuracy was reported in our previous studies (Hsieh et al., 2022). The solubilities of two Fe leachs were calculated by dividing the leached concentrations to the total concentrations.

4.2.3 Quantification of Fe isotopic composition

.Fe isotopic composition of the total, dissolved, and labile Fe fractions were determined by using a multi-collector Inductively Couple Plasma Mass Spectrometer (MC-ICP-MS, Neptune Plus, Thermo Fisher Scientific) with an APEX-IR (Elemental Scientific) and X-type skimmer cone (Elemental Scientific). Samples were measured in high-resolution mode with Cr^{54} correction on Fe^{54} and Ni^{58} correction on Fe^{58}. The δ^{56}Fe samples were applied by the double-spike (Fe^{57} and Fe^{58} addition) technique, and the sample-to-spike ratio was 1:2 (Dauphas et al., 2017). The δ^{56}Fe data ($^{56}Fe/^{54}Fe$) ratios are reported in delta notation (‰) relative to the IRMM-014 Fe isotope reference material (Institute for Reference Materials and Measurements) and described below:

$$\delta^{56}\mathrm{Fe}\ (‰) = \left(\frac{(^{56}Fe\ /\ ^{54}Fe)_{sample}}{(^{56}Fe\ /\ ^{54}Fe)_{IRMM-014}} - 1\right) \times 1000$$

To minimize the Cr and Ni interferences, we have purified all samples by using the anion exchange resin (AG1-X8, Bio-Rad, 100-200 mesh). The samples with isobaric interferences from Cr and Ni in 1.4ml 7N HCl solution were loaded into perfluoroalkoxy alkanes (PFA, Savillex) microcolumns filled with AG1-X8 anion exchange resin (Bio-Rad, 100-200 mesh), then loaded three times of ultrapure 0.4ml 7N HCl to removed Ni and Cr interference. The Fe samples were absorbed on anion exchanged resin and eluted out by 0.7 N HCl eluent solution.

The eluted Fe samples were dried up with open caps then redissolved dried samples in 1 ml 0.5 M HNO_3 solution at 120°C (heater temperature) with closed caps for 1 h for further isotopic measurement.

4.3 Result

4.3.1 The seasonal variations of δ^{56}Fe in size-fractionated aerosols

Figure 4.2 exhibits the seasonal variations of δ^{56}Fe in the size-fractionated aerosol samples. We found that the total digestion value remained relatively consistent for the three larger aerosols, with values to be 0.10 to -0.08 ‰, 0.16 to 0.00 ‰, and 0.14 to -0.06 ‰ for size cut-offs 1.6, 3.1, and 7.3 mm, respectively. However, for the two smallest size aerosols, δ^{56}Fe sharply decreased with decreasing sizes, with values to be -0.45 to -3.35 and -0.06 to -1.16 ‰ for size cut-offs 0.57 and 1.0 mm, respectively (Table S4.1). In terms of the seasonality of δ^{56}Fe in total digestion treatment, the averaged value of two smallest size aerosols collected during NE seasons, which were -2.19±091 ‰ and -0.54±0.41 ‰ for size cut-offs 0.57 and 1.0 mm, respectively, were significantly lower than the value obtained in SW seasons, which were -0.66±0.29 ‰ and -0.15±0.04 ‰ (Table S4.1). The relatively low δ^{56}Fe (-1.8 ‰ in size cut-off 0.57 mm) in August 2020 was caused by a typhoon event and brought more anthropogenic aerosols from mainland China so we do not include the sample in the calculation (Fig.4.1).

In terms of dissolved and labile treatments, the varying pattern with the size is similar to total digestion treatment, with consistent values for the three large sizes and significantly lower values for the two small size aerosols. However, compared to total digestion, we found that the value observed in dissolved and labile fractions were significantly lower than the

doi:10.6342/NTU202302200

value of total digestion for size cut-offs 0.57 and 1.0 μm. The decreases of δ^{56}Fe for dissolved and labile were 0.96, 0.27, and 0.95, 0.31 for size cut-offs 0.57 and 1.0 μm, respectively (Table S4.1).

4.4 Discussion

4.4.1 Evidence for two end member mixing: from elemental ratios and δ^{56}Fe

Elemental ratios are useful to evaluate the relative contribution of anthropogenic and lithogenic aerosols. Using the same aerosol samples, Hsieh et al. (2022) observed strong linear correlations between the enrichment factors (EF) of some anthropogenic type elements (e.g., Pb, V, nss-S) and the solubilities of either dissolved or labile Fe in ECS aerosols, suggesting that the Fe solubilities were overall decided by the two end member mixing between lithogenic and anthropogenic aerosols. As different elements may have different sources in the same aerosol samples, the enrichment of a typical anthropogenic type element, such as Pb, does not guarantee that Fe in the same samples also originates from anthropogenic activities. The coupling of δ^{56}Fe and the elemental ratios may be useful to distinguish the major source(s) of AN-Fe. Here, we compare the elemental ratio of some typical anthropogenic type elements to Ti with δ^{56}Fe. In addition to Pb, V, nss-S, and Fe, we have added Cd and nss-K for the comparison, which are the other two representative elements for anthropogenic activities and biomass burning, respectively. Spanning over 3 orders of magnitudes in 5-size fractionated aerosols (3 to 3,700), the EF of Cd was highest among all of the elements measured (Hsieh et al., 2023). Assuming that there are simply two major end members (lithogenic and anthropogenic) for aerosol Fe, Cd to Ti ratios may thus serve as the most sensitive and reliable indicator to evaluate the assumption.

doi:10.6342/NTU202302200

Figure 4.3 exhibits the correlations between the Ti-normalized ratios of the 5 elements and Fe) and δ^{56}Fe in bulk aerosols. Almost all of the ratios exhibit negative linear correlations with δ^{56}Fe in the two finer size aerosol fractions. In terms of biomass burning representative element, potassium (K), its concentrations and enrichment factor in biomass burning aerosols are known to be one order of magnitude higher than the value observed in lithogenic particles. However, the study reported that Fe isotope composition in biomass burning aerosols was comparable to the value in lithogenic dust (Kurisu and Takahashi, 2019). Although we did observe high nss-K to Ti ratios, the δ^{56}Fe values were much lower than the value in lithogenic aerosols, indicating that biomass burning was unlikely to be a major fine aerosol Fe source in the ECS aerosol samples. Similarly, V/Ti ratio can be an indicator for fly ashes originating from heavy oil combustion. The V/Ti ratios in heavy fuel oil aerosol emission ranges from 120 to 1,000 mol/mol (Basha et al., 2020; Streibel et al., 2017). The V to Ti ratio observed in this study was only about 2 mol/mol and shows a relatively low correlation ($r^2 = 0.69$) with δ^{56}Fe, also indicating that heavy oil burning is unlikely to be the major source of fine aerosol Fe with relatively low δ^{56}Fe. We found that Cd and Pb ratios exhibited stronger linear correlation with δ^{56}Fe among the 6 elements, with correlation coefficients of 0.94 and 0.82, respectively. Both Cd and Pb have relatively low melting/boiling temperature, which are 321/767 and 327/1749 °C for Cd and Pb, respectively. The two metals, which originate from anthropogenic activities involving with high temperature combustion, such as coal and oil burning, metal smelting and refining, and waste incineration, would thus be vaporized, condensed, aggregated, and adsorbed on flying ashes so that Cd and Pb ashes are highly enriched in the flying ashes fine aerosols. These Cd/Ti and Pb/Ti ratios may be useful to quantify the contribution of AN-Fe in our region. Our two end members mixing assumption for aerosol Fe is thus strongly supported by the high correlation observed between decreasing δ^{56}Fe and increasing Cd (or Pb) to Ti ratios. The lowest δ^{56}Fe value observed in the smallest

doi:10.6342/NTU202302200

size (0.57 mm) aerosol of this study was -3.35 ‰. The value is comparable to the value reported in previous studies in which the lowest δ^{56}Fe value in bulk aerosol collected in a tunnel with heavy traffic or near the steel plant were -3.2 ‰ and -3.5 ‰, respectively (Kurisu et al., 2019; Kurisu et al., 2016a). The relatively low δ^{56}Fe values in the fine aerosols suggest that high temperature fossil fuel combustion is a major source of the fine aerosol Fe, most likely originating from coal burning in our samples (Fig. 4.3).

Since AN-Fe has a much higher solubility than lithogenic aerosol Fe, the fraction of dissolved and labile Fe in fine aerosol are supposed to be composed of the extremely high percentage of AN-Fe, in which the isotopic value shall be fairly close to the end member of anthropogenic Fe. Indeed, we found that the lowest values were -4.46 and -4.34 ‰ in the dissolved and labile Fe fractions, respectively (Fig. 4.2, Table S4.1). Assuming that the end member of δ^{56}Fe in AN-Fe is the lowest value observed in our studied region, which is -4.5 ‰. As the most positive δ^{56}Fe observed in the largest aerosol size is 0.16 ‰, which is within the value proposed in lithogenic aerosols (Beard et al., 2003; Conway et al., 2019; Mead et al., 2013; Waeles et al., 2007), we then assume the end member of lithogenic aerosols to be 0.2 ‰. Based on the correlation of δ^{56}Fe and Cd/Ti ratio, the estimated end member of Cd/Ti and Pb/Ti ratios are 0.050 and 1.03, respectively (Fig. 4.3).

4.4.2 δ^{56}Fe vs Fe solubility

We have compared δ^{56}Fe in size-fractionated aerosols by total digestion with the solubilities of dissolved and labile Fe (Fig. 4.4A-a,b). Overall, a significant linear correlation was observed between δ^{56}Fe and dissolved and labile Fe, with r^2 to be 0.81 and 0.76 (Fig. 4.4A), respectively, demonstrating that soluble Fe mainly originated from anthropogenic aerosols. However, the overall solubilities varied up to 4 orders of magnitude for all of the 5

doi:10.6342/NTU202302200

size samples, but the isotopic value only varied from 0.16 to -3.4‰. Considering the precision of Fe isotopic standard (NIST 3126a), which is about 0.05‰, the resolution of Fe isotopic analysis is insufficient to distinguish the contribution of anthropogenic aerosols in the three larger fractions (7.3, 3.1, and 1.6 mm), in which solubilities varied for 2 orders of magnitude (0.01 to 0.01-5.4 %) for dissolved Fe but δ^{56}Fe ranged from 0.16 to -0.08 ‰(Fig. 4.4A-a). Instead, the Cd/Ti ratios for the 3 larger size aerosols also varied up to two orders of magnitude, 0.00004-0.00362 (Hsieh et al., 2023) and Cd/Ti and Pb/Ti exhibited high correlation in three larger fractions (Fig. 4.3). Thus, we assume that Cd/Ti ratios (EF_{Cd}) are a useful and sensitive parameter to represent the contribution of anthropogenic aerosol (Fe) in relatively large aerosols. Based on two end member mixing assumption and the end member value of Cd/Ti ratios (0.050) observed in anthropogenic aerosol (Fig. 4.3) and (0.000012) in the lithogenic dust (Hu and Gao, 2008), the estimated δ^{56}Fe for the highest Cd/Ti sample in the 3 fractions would be -0.14 ‰, which is quite close to the value measured (-0.08‰). Assuming the end member of Fe solubility to be 80% (Fig. 4.4A-a), the estimated solubility for the sample is 5.8%, which is also relatively close to the value observed, 3.7%. Further studies are required to examine the value of Cd/Ti ratios as a proxy of the contribution of AN-Fe and Fe solubility.

The strong linear correlation between Cd/Ti ratios and low δ^{56}Fe for PM 1.0 strongly support that the PM 1.0 were decided by lithogenic and anthropogenic aerosols two end member mixing (Fig. 4.3, Fig. 4.4A). However, the correlation between solubility and δ^{56}Fe in the two finest fractions was relatively poor (Fig. 4.4A-c), with solubilities varying from 2.5 to 74% and δ^{56}Fe varying from -0.11 to -3.4‰. We argue that other physical and chemical conditions may be important on influencing the solubilities. For example, nss-S/Ti exhibit better correlations with DFe and LFe than δ^{56}Fe (Fig. 4.4B-a,b), suggesting that inorganic

doi:10.6342/NTU202302200

acid concentrations in aerosol samples is a critical factor controlling Fe solubility and δ^{56}Fe with different extent. Other factors, which may include the availability of organic acids, inorganic and organic ligands, the strength of solar radiation, and in-cloud processes.

4.4.3 Quantitative estimate for the contribution of AN-Fe: δ^{56}Fe vs Cd/Ti ratio

As mentioned in 4.1, using 0.2/-4.5 ‰ and 0.00001/0.05 as the two end members of δ^{56}Fe and Cd/Ti ratios in lithogenic aerosol Fe and AN-Fe, respectively, we may quantify the relative contribution of each member by two-component mixing model (Table S4.2,4.3). In terms of the two small fractions, we found that the contribution estimated of bulk AN-Fe by Cd/Ti ratio is comparable with data obtained by δ^{56}Fe. However, the difference of the value estimated by the two approaches significantly increase with increasing sizes. The ratio of the value estimated by the δ^{56}Fe approach divided by value Cd/Ti approach are 1.4, 1.7, 3.6, 7.6, and 12 with sizes (Table S4.2), respectively. The significant disagreement in the large fraction may be caused by the data range close or within detection limits, causing the overestimate of AN-Fe contribution in three larger aerosol sizes. Assuming that the contribution of AN-Fe in coarse fraction still follows two end member mixing, the relatively linear correlation between Cd/Ti and Pb/Ti ratios indicate that Cd/Ti shall be a more reliable parameter to estimate the contribution of bulk AN-Fe in coarse aerosols than δ^{56}Fe. In terms of dissolved and labile Fe, we can only use δ^{56}Fe to carry out the estimate since the value of Cd/Ti and Pb/Ti show extremely poor correlation with δ^{56}Fe.

Estimated by δ^{56}Fe two end member approach, the estimated mass contributions of AN-Fe in size cut-offs 0.57/1.0 mm would be 51/16% and 18/7.5% for the NE and SW monsoon seasons, respectively (Table S4.2). Since fine aerosol only accounted for 29% of the bulk aerosol mass in the ECS, the average AN-Fe mass only accounts for 7.0 and 4.7% in the

NE and SW monsoon seasons, respectively. Using the December sample as an example, AN-Fe contributed 10, 44, and 86% of Fe for total, labile, and dissolved masses, respectively (Table S4.2). Considering the deposition velocity of different sizes (Hsieh et al., 2022), the contribution of AN-Fe in the bulk aerosol flux. In terms of the NE season (December) were 3.9, 6.2, and 23% for total, labile, and dissolved, respectively (Table S4.2). Using the same two-end member approach as δ^{56}Fe, we may use Cd/Ti ratios to estimate the contribution of AN-Fe in bulk aerosol. The contribution of An-Fe was even smaller than the value estimated by the δ^{56}Fe approach (Table S4.2). In brief, this study demonstrates that lithogenic aerosol is still the major source of dissolvable aerosol Fe in the surface water of the ocean with high anthropogenic aerosol concentrations (e.g., ECS).

4.5 Conclusion

In this study, we observed that the lowest δ^{56}Fe value of bulk, dissolved, and labile Fe were -3.35, -4.46, and -4.34, respectively. We found that the ratio of Cd/Ti is a useful and sensitive parameter to estimate the contribution of bulk AN-Fe in coarse aerosols. When the δ^{56}Fe data is unavailable, the Cd or Pb to Ti ratios may serve as an alternative parameter to quantify the contribution of AN-Fe. The correlation between δ^{56}Fe and some metal to Ti ratios support that aerosols collected in the ECS were mainly mixed by lithogenic and anthropogenic Fe. Using 0.2/-4.5 ‰ and 0.00001/0.05 as the two end members of δ^{56}Fe and Cd/Ti ratios in lithogenic aerosol Fe and AN-Fe, respectively, we have quantified the relative contribution of each member by two-component mixing model (Table S4.3). Anthropogenic aerosols are the major source of dissolvable Fe concentrations in fine aerosols. However, in terms of deposition fluxes, lithogenic aerosols are still the dominant source of dissolved, labile, and bulk aerosol Fe in the ocean.

doi:10.6342/NTU202302200

4.6 References

Andreae, M.O., 1983. Soot carbon and excess fine potassium: long-range transport of combustion-derived aerosols. Science, 220(4602): 1148-51 DOI: 10.1126/science.220.4602.1148.

Baker, A.R. and Jickells, T.D., 2006. Mineral particle size as a control on aerosol iron solubility. Geophysical Research Letters, 33(17) DOI: 10.1029/2006gl026557.

Basha, S.I. et al., 2020. Characterization, Processing, and Application of Heavy Fuel Oil Ash, an Industrial Waste Material - A Review. Chem Rec, 20(12): 1568-1595 DOI: 10.1002/tcr.202000100.

Beard, B.L., Johnson, C.M., Von Damm, K.L. and Poulson, R.L., 2003. Iron isotope constraints on Fe cycling and mass balance in oxygenated Earth oceans. Geology, 31(7) DOI: 10.1130/0091-7613(2003)031<0629:Iicofc>2.0.Co;2.

Buck, C.S., Aguilar-Islas, A., Marsay, C., Kadko, D. and Landing, W.M., 2019. Trace element concentrations, elemental ratios, and enrichment factors observed in aerosol samples collected during the US GEOTRACES eastern Pacific Ocean transect (GP16). Chemical Geology, 511: 212-224 DOI: 10.1016/j.chemgeo.2019.01.002.

Buck, C.S., Landing, W.M., Resing, J.A. and Lebon, G.T., 2006. Aerosol iron and aluminum solubility in the northwest Pacific Ocean: Results from the 2002 IOC cruise. Geochemistry, Geophysics, Geosystems, 7(4) DOI: 10.1029/2005gc000977.

Conway, T.M. et al., 2019. Tracing and constraining anthropogenic aerosol iron fluxes to the North Atlantic Ocean using iron isotopes. Nat Commun, 10(1): 2628 DOI: 10.1038/s41467-019-10457-w.

Cutter, G. et al., 2017. Sampling and Sample-handling Protocols for GEOTRACES Cruises. 3 DOI: 10.25607/OBP-2.

Dauphas, N., John, S.G. and Rouxel, O., 2017. Iron Isotope Systematics. Reviews in Mineralogy and Geochemistry, 82(1): 415-510 DOI: 10.2138/rmg.2017.82.11.

Eggimann, D.W. and Betzer, P.R., 1976. Decomposition and Analysis of Refractory Oceanic

Suspended Materials. Analytical Chemistry, 48(6): 886-890 DOI: DOI 10.1021/ac60370a005.

Gong, Y., Xia, Y., Huang, F. and Yu, H., 2016. Average iron isotopic compositions of the upper continental crust: constrained by loess from the Chinese Loess Plateau. Acta Geochimica, 36(2): 125-131 DOI: 10.1007/s11631-016-0131-5.

Hsieh, C.-C., Chen, H.-Y. and Ho, T.-Y., 2022. The effect of aerosol size on Fe solubility and deposition flux: A case study in the East China Sea. Marine Chemistry, 241 DOI: 10.1016/j.marchem.2022.104106.

Hsieh, C.-C., You, C.-F. and Ho, T.-Y., 2023. The solubility and deposition flux of East Asian aerosol metals in the East China Sea: The effects of aeolian transport processes. Marine Chemistry DOI: 10.1016/j.marchem.2023.104268.

Hu, Z.C. and Gao, S., 2008. Upper crustal abundances of trace elements: A revision and update. Chemical Geology, 253(3-4): 205-221 DOI: 10.1016/j.chemgeo.2008.05.010.

Kurisu, M., Adachi, K., Sakata, K. and Takahashi, Y., 2019. Stable Isotope Ratios of Combustion Iron Produced by Evaporation in a Steel Plant. ACS Earth and Space Chemistry, 3(4): 588-598 DOI: 10.1021/acsearthspacechem.8b00171.

Kurisu, M. et al., 2016. Variation of Iron Isotope Ratios in Anthropogenic Materials Emitted through Combustion Processes. Chemistry Letters, 45(8): 970-972 DOI: 10.1246/cl.160451.

Kurisu, M. and Takahashi, Y., 2019. Testing Iron Stable Isotope Ratios as a Signature of Biomass Burning. Atmosphere, 10(2) DOI: 10.3390/atmos10020076.

Mead, C., Herckes, P., Majestic, B.J. and Anbar, A.D., 2013. Source apportionment of aerosol iron in the marine environment using iron isotope analysis. Geophysical Research Letters, 40(21): 5722-5727 DOI: 10.1002/2013gl057713.

Morton, P.L. et al., 2013. Methods for the sampling and analysis of marine aerosols: results from the 2008 GEOTRACES aerosol intercalibration experiment. Limnology and Oceanography: Methods, 11(2): 62-78 DOI: 10.4319/lom.2013.11.62.

Nriagu, J.O. and Pacyna, J.M., 1988. Quantitative assessment of worldwide contamination of air, water and soils by trace metals. Nature, 333(6169): 134-9 DOI: 10.1038/333134a0.

Perron, M.M.G. et al., 2020. Assessment of leaching protocols to determine the solubility of trace metals in aerosols. Talanta, 208: 120377 DOI: 10.1016/j.talanta.2019.120377.

Pinedo-Gonzalez, P. et al., 2020. Anthropogenic Asian aerosols provide Fe to the North Pacific Ocean. Proc Natl Acad Sci U S A, 117(45): 27862-27868 DOI: 10.1073/pnas.2010315117.

Sarthou, G. et al., 2003. Atmospheric iron deposition and sea-surface dissolved iron concentrations in the eastern Atlantic Ocean. Deep Sea Research Part I: Oceanographic Research Papers, 50(10-11): 1339-1352 DOI: 10.1016/s0967-0637(03)00126-2.

Sholkovitz, E.R., Sedwick, P.N. and Church, T.M., 2009. Influence of anthropogenic combustion emissions on the deposition of soluble aerosol iron to the ocean: Empirical estimates for island sites in the North Atlantic. Geochimica et Cosmochimica Acta, 73(14): 3981-4003 DOI: 10.1016/j.gca.2009.04.029.

Streibel, T. et al., 2017. Aerosol emissions of a ship diesel engine operated with diesel fuel or heavy fuel oil. Environ Sci Pollut Res Int, 24(12): 10976-10991 DOI: 10.1007/s11356-016-6724-z.

Waeles, M., Baker, A.R., Jickells, T. and Hoogewerff, J., 2007. Global dust teleconnections: aerosol iron solubility and stable isotope composition. Environmental Chemistry, 4(4) DOI: 10.1071/en07013.

4.7 Figures

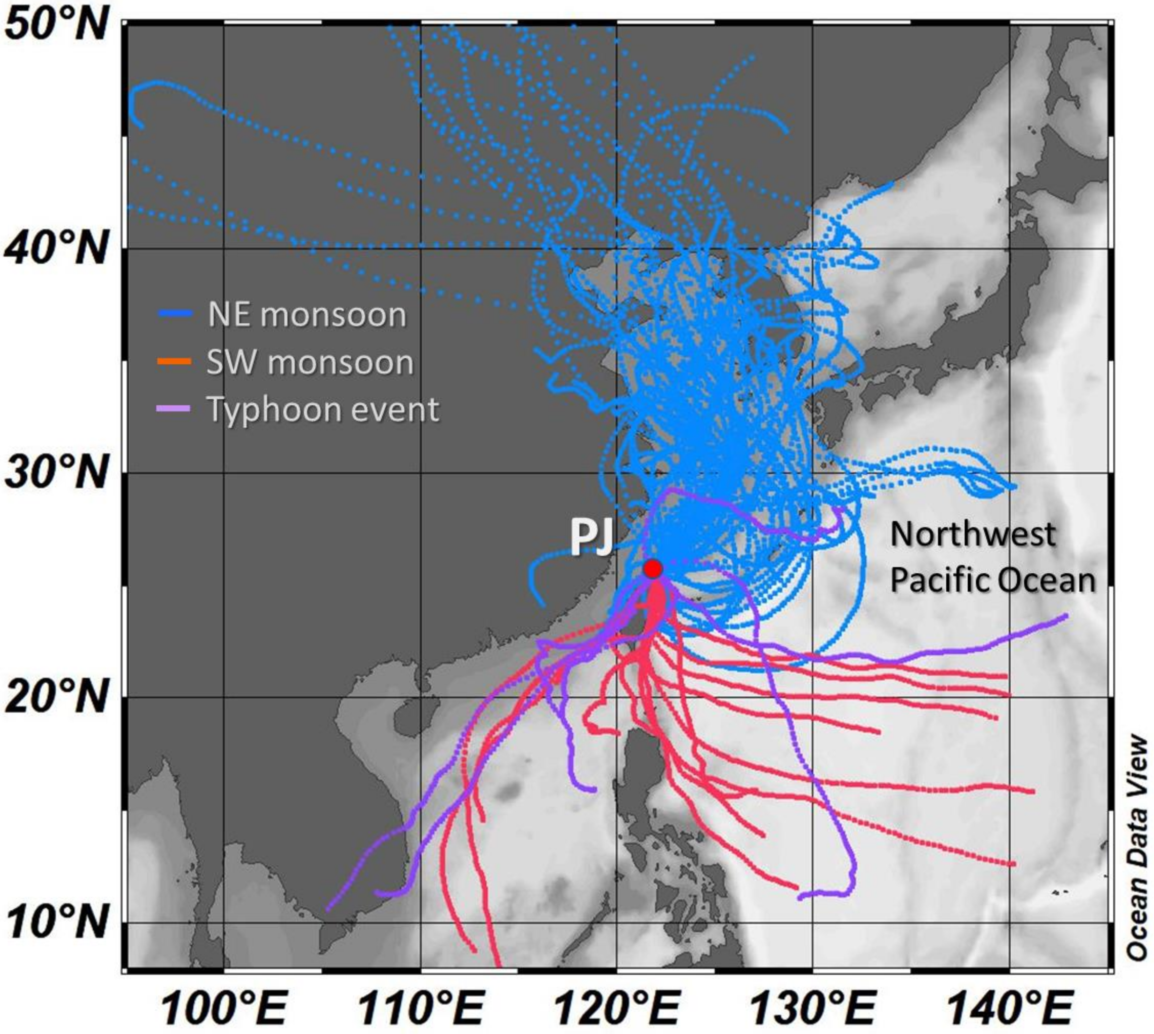

Figure 4.1. The location of the sampling station, Penjia islet (PJ), and Seven-day air mass backward trajectory. The red, blue, and purple lines stand for southwestern monsoon, northeastern monsoon, and typhoon events, respectively.

doi:10.6342/NTU202302200

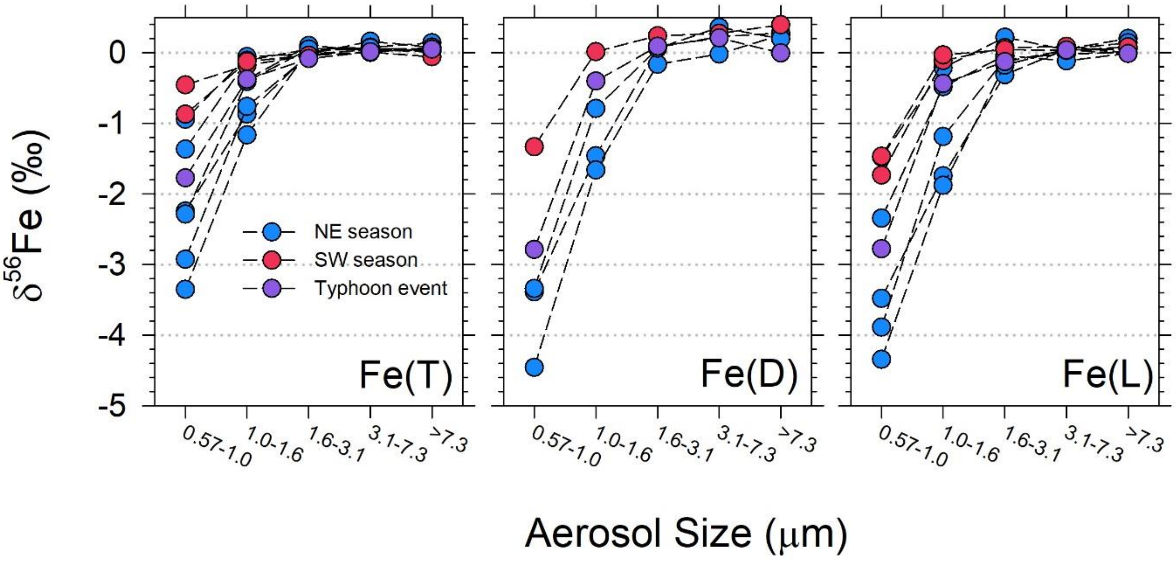

Figure 4.2. The Fe isotopic composition of dissolved, labile, and total protocols in the size-fractionated aerosols at Pengjia Islet. Circle symbols with red, blue, and purple filled circles stand for southwestern monsoon, northeastern monsoon, and typhoon event, respectively.

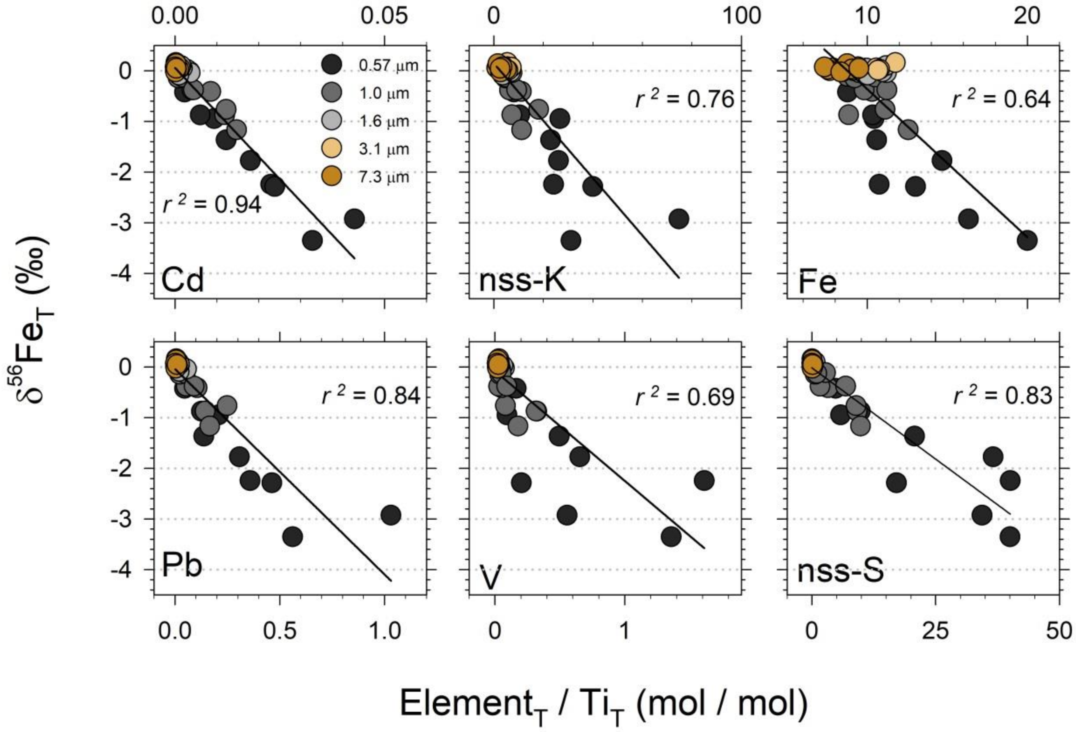

Figure 4.3. The correlation among δ^{56}Fe with metal to Ti ratios in the total treatment. The circle symbol colors are black for size cut-offs 0.57 μm, gray for 1.0 μm, beige for 3.1 μm, orange for 3.1μm, and brown for 7.3 μm, respectively.

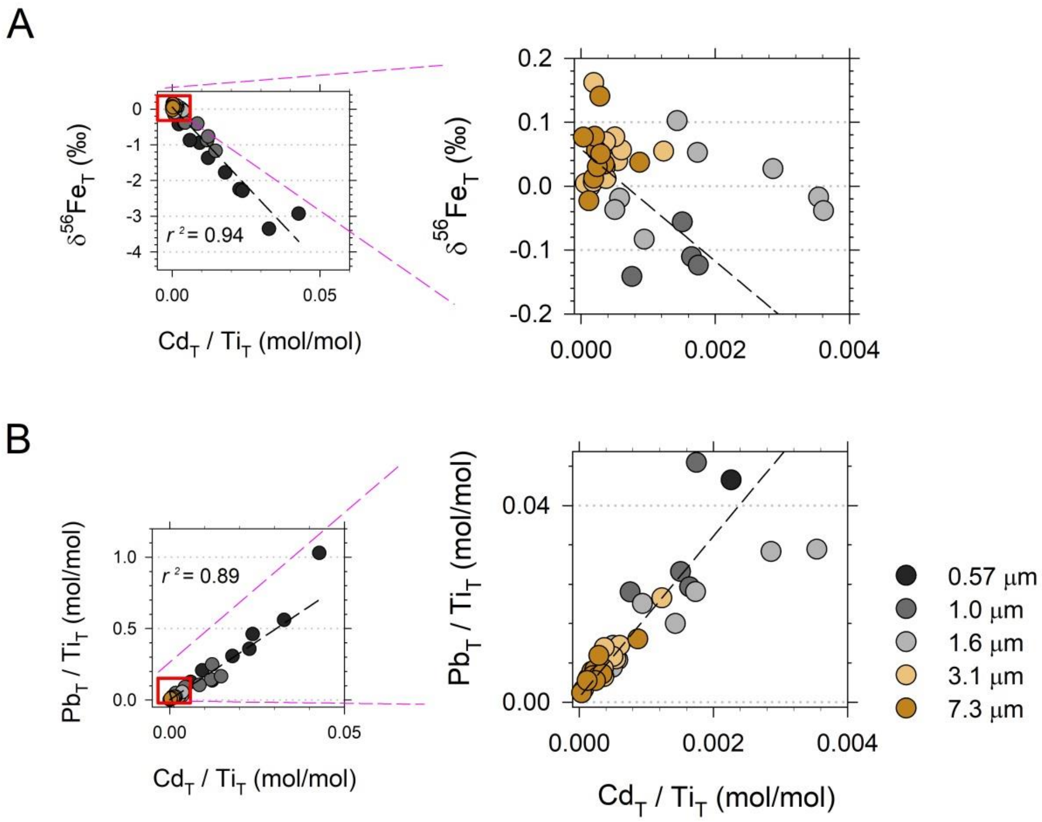

Figure 4.4. The correlation among Cd to Ti ratio with δ^{56}Fe and Pb to Ti ratios in the total treatment. The circle symbol colors are black for size cut-offs 0.57 μm, gray for 1.0 μm, beige for 3.1 μm, orange for 3.1μm, and brown for 7.3 μm, respectively.

doi:10.6342/NTU202302200

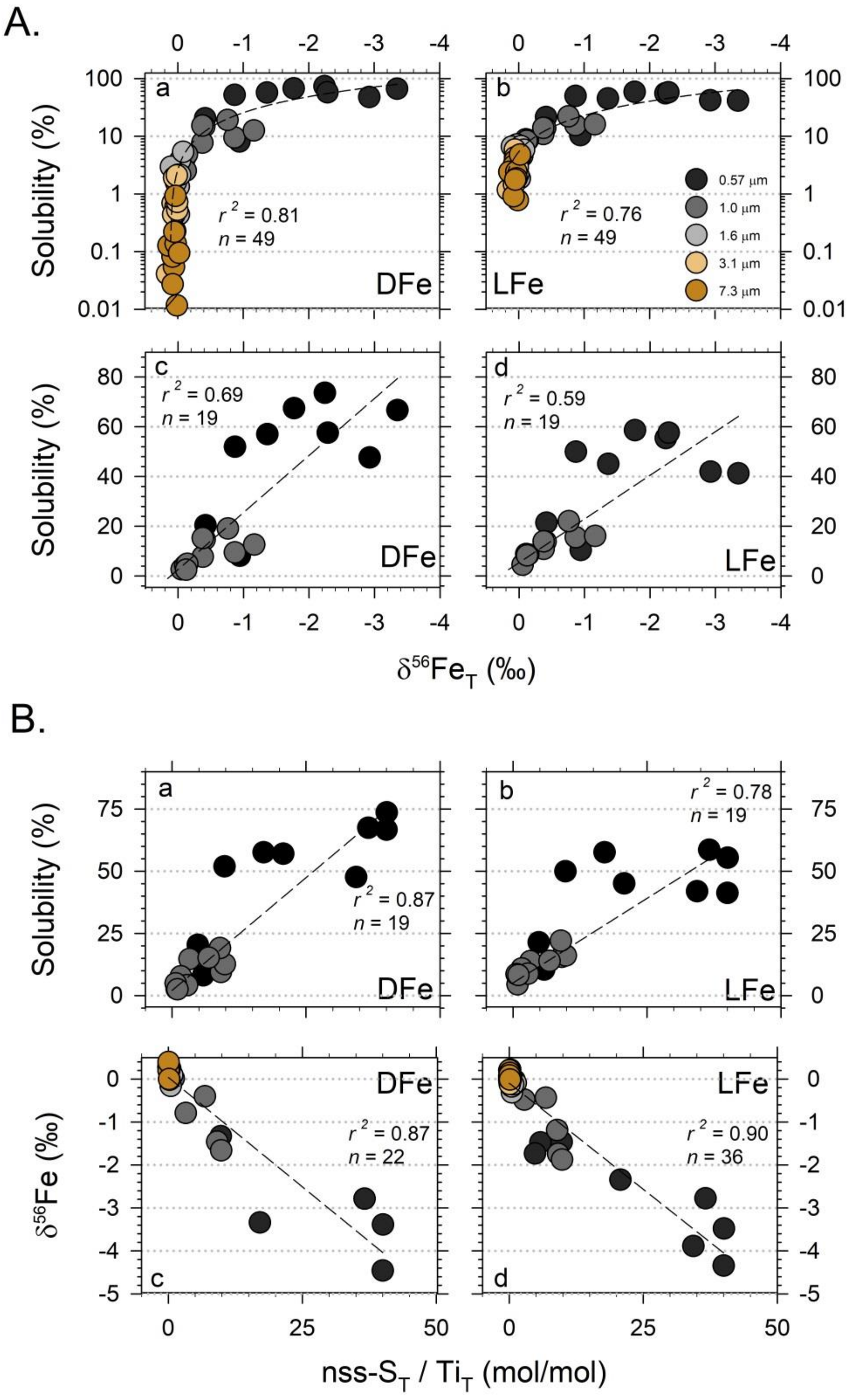

Figure 4.5. The correlation among δ^{56}Fe with solubilities and nss-S to Ti ratio of DFe and LFe. The circle symbol colors are black for size cut-offs 0.57 µm, gray for 1.0 µm, beige for 3.1 µm, orange for 3.1µm, and brown for 7.3 µm, respectively.

doi:10.6342/NTU202302200

4.8 Supplementary

Table S4.1. The information of the δ^{56}Fe of size-fractionated aerosols collected in this study.

Size cut-offs (μm)	Fraction	δ^{56}Fe (‰)									
		Sep	Dec	Jan	Feb	Mar	Apr	May	Jun	Jul	Aug
0.57	Total	-2.24	-3.35	-2.93	-0.94	-2.29	n.a.	-1.36	-0.45	-0.87	-1.77
	Dissolve	-3.39	-4.46	n.a.*	n.a.	-3.34	n.a.	n.a.	n.a.	-1.33	-2.79
	Labile	-3.48	-4.34	-3.89	-1.48	n.a.	n.a.	-2.34	-1.73	-1.47	-2.78
1.0	Total	-0.87	-1.16	-0.76	-0.06	-0.41	-0.38	-0.11	-0.18	-0.12	-0.38
	Dissolve	-1.46	-1.66	n.a.	n.a.	-0.79	n.a.	n.a.	n.a.	0.01	-0.40
	Labile	-1.74	-1.88	-1.19	-0.22	n.a.	n.a.	-0.48	-0.11	-0.03	-0.44
1.6	Total	-0.02	0.03	-0.04	-0.02	0.05	0.10	0.05	-0.04	-0.04	-0.08
	Dissolve	0.08	-0.16	n.a.	n.a.	0.06	n.a.	n.a.	n.a.	0.24	0.09
	Labile	-0.31	-0.18	-0.09	0.22	n.a.	n.a.	-0.04	0.07	0.04	-0.13
3.1	Total	0.04	0.06	0.05	0.16	0.08	0.03	0.07	0.00	0.01	0.01
	Dissolve	0.23	-0.02	n.a.	n.a.	0.36	n.a.	n.a.	n.a.	0.27	0.21
	Labile	0.05	0.05	-0.01	0.04	n.a.	n.a.	-0.12	0.09	0.03	0.04
7.3	Total	0.01	0.06	0.04	0.08	0.14	0.03	0.03	0.08	-0.06	0.05
	Dissolve	0.28	0.25	n.a.	n.a.	0.20	n.a.	n.a.	n.a.	0.40	0.00
	Labile	0.20	0.14	0.00	0.05	n.a.	n.a.	-0.01	0.00	0.08	-0.01

*n.a.: data are not available.

doi:10.6342/NTU202302200

Table S4.2. The information of the contribution of anthropogenic aerosol Fe among NE and SW monsoon seasons by δ^{56}Fe and Cd/Ti approaching.

Anthropogenic Fe estimate method		NE (12/2019)			SW (07/2020)		
		Total	Dissolved	Labile	Total	Dissolved	Labile
By δ^{56}Fe	Conc. (%)	9.6	86	41	5.6	25	12
	Flux (%)	3.2	34	2.8	5.2	3.4	2.9
By Cd/Ti	Conc. (%)	7.3	n.a.	n.a.	0.9	n.a.	n.a.
	Flux (%)	0.7	n.a.	n.a.	0.3	n.a.	n.a.

*n.a.: data are not available.

doi:10.6342/NTU202302200

Table S4.3. The anthropogenic Fe contribution for the samples of dissolved, buffer, and total treatments.

Size cut-offs (μm)	Fraction	Anthropogenic Fe contribution (%)									
		Sep	Dec	Jan	Feb	Mar	Apr	May	Jun	Jul	Aug
0.57	Total	52	76	67	24	53	n.a.	33	14	23	42
	Dissolve	77	99	n.a.*	n.a.	76	n.a.	n.a.	n.a.	35	65
	Labile	79	97	87	38	n.a.	n.a.	56	44	38	65
1.0	Total	23	29	20	5.4	13	12	6.6	8.0	6.9	12
	Dissolve	38	42	n.a.	n.a.	24	n.a.	n.a.	n.a.	7.9	16
	Labile	44	46	32	13	n.a.	n.a.	18	10	8.8	17
1.6	Total	4.6	3.7	5.1	4.7	3.1	2.1	3.2	5.0	5.0	6.0
	Dissolve	6.6	11	n.a.	n.a.	6.9	n.a.	n.a.	n.a.	3.2	6.3
	Labile	15	12	10	3.7	n.a.	n.a.	9.0	6.7	7.3	11
3.1	Total	3.4	3.1	3.1	0.8	2.6	3.6	2.8	4.2	4.1	4.0
	Dissolve	3.5	8.5	n.a.	n.a.	0.8	n.a.	n.a.	n.a.	2.6	0.0
	Labile	7.1	7.1	8.5	7.3	n.a.	n.a.	11	6.4	7.5	7.4
7.3	Total	4.0	3.1	3.5	2.6	1.3	3.5	3.6	2.6	5.5	3.2
	Dissolve	2.4	3.0	n.a.	n.a.	4.2	n.a.	n.a.	n.a.	0.1	8.2
	Labile	4.1	5.3	8.2	7.1	n.a.	n.a.	8.3	8.2	6.5	8.4
7.3	Total	4.0	3.1	3.5	2.6	1.3	3.5	3.6	2.6	5.5	3.2
	Dissolve	2.4	3.0	n.a.	n.a.	4.2	n.a.	n.a.	n.a.	0.1	8.2
	Labile	4.1	5.3	8.2	7.1	n.a.	n.a.	8.3	8.2	6.5	8.4
7.3	Total	4.0	3.1	3.5	2.6	1.3	3.5	3.6	2.6	5.5	3.2
	Dissolve	2.4	3.0	n.a.	n.a.	4.2	n.a.	n.a.	n.a.	0.1	8.2
	Labile	4.1	5.3	8.2	7.1	n.a.	n.a.	8.3	8.2	6.5	8.4

*n.a.: data are not available

Chapter 5

The concentration and isotopic feature of particulate Fe in the Subarctic Pacific Ocean: spatial distribution and sources

By
Chih-Chiang Hsieh[a,b], Wen-Hsuan Liao[b,c], Hajime Obata[d], Tung-Yuan Ho*[a,b]

[a] Institute of Oceanography, National Taiwan University, Taipei, Taiwan
[b] Research Center for Environmental Changes, Academia Sinica, Taipei, Taiwan
[c] Department of Earth Sciences, National Cheng Kung University, Tainan, Taiwan
[d] Atmosphere and Ocean Research Institute, The University of Tokyo, Kashiwa, Japan

doi:10.6342/NTU202302200

5.0 Abstract

Joining the GEOTRACES subarctic Pacific Ocean transect study (GP-02), we investigated the contribution of different Fe sources in the subarctic Pacific Ocean. We collected suspended particulate material in the water column to investigate the spatial distribution of particulate Fe concentrations and isotopic composition in the high-nutrient low-chlorophyll region. Previous studies reported that labile particulate iron (Fe) is a dominant fraction in total dissolved Fe (dissolved Fe plus labile particulate Fe) in the surface water of the subarctic Pacific Ocean. Thus, particulate iron (PFe) may be a critical Fe source while dissolved Fe is depleted. Some other recent studies reported that anthropogenic aerosol Fe may provide considerable soluble Fe into the Northwestern Pacific Ocean. However, anthropogenic Fe contribution estimates are highly challenging due to limited open ocean field data. In this study, we did not observe significant δ^{56}Fe features of the anthropogenic aerosol Fe in the surface particulate Fe samples. The δ^{56}Fe range of particulate Fe in the surface water (<100m) was -0.02 to 0.32 ‰, indicating that lithogenic particles are the major components in the particulate Fe. For the deep ocean, we observed slightly light δ^{56}Fe values (lower to -0.12 ‰) at stations close to the marginal sea, suggesting that resuspended sediments or pore water from continental shelves and slopes may be the major sources of PFe. In terms of biotic particulate Fe, the average δ^{56}Fe value is -0.24 ± 0.06 ‰, which also supports that anthropogenic aerosol Fe is not the major source of dissolvable Fe in the euphotic zone. In brief, our results indicate that lithogenic particles are the primary particulate Fe source throughout the water column in the subarctic Pacific Ocean.

5.1 Introduction

Iron (Fe) is a limiting factor for phytoplankton growth in large areas of the global ocean, particularly in high-nutrient low-chlorophyll (HNLC) regions (Martin et al., 1994; Martin and Fitzwater, 1988; Moore et al., 2013). Fe supply would thus regulate primary productivity and carbon and nutrient cycling in the HNLC regions. The subarctic Pacific Ocean is one of the HNLC regions, and Fe fertilization experiments have shown that Fe availability limits phytoplankton biomass in both the western and eastern subarctic Pacific Ocean ((Boyd et al., 2004; Tsuda et al., 2003).

Additional to aeolian input, it has also been reported that the continental margin and shelves of marginal seas provide large amounts of dissolved and particulate sedimentary Fe which is transported by intermediate water circulations (Lam and Bishop, 2008; Nishioka et al., 2007). The marginal seas may include the Okhotsk Sea, Bering Sea, and the eastern side of the subarctic Pacific Ocean. Moreover, riverine discharge, hydrothermal input, and sea ice melting may potentially be important external Fe sources in the water column of the subarctic Pacific Ocean. Although atmospheric dust deposition has been considered to be the primary dissolvable Fe source in the euphotic zone of the subarctic Pacific Ocean, no direct evidence has been shown to demonstrate the importance of aerosol deposition on Fe supply in the surface water.

Most of the previous studies on Fe cycling in the ocean have focused on dissolved form. However, dissolved Fe concentrations are fairly low and stable in the subarctic Pacific Ocean, generally ranging from 0.05 to 0.1 nM throughout the surface water of the open ocean region (Nishioka et al., 2020; Wong et al., 2022). On the other hand, the concentrations of particulate Fe are relatively high (a few nM), which may serve as an important source for Fe cycling in the region. Zheng and Sohrin (2019) reported that labile particulate Fe dominates the total dissolved Fe (dissolved Fe and labile particulate Fe) in the North Pacific Ocean, and labile particulate Fe concentration accounts for 0.544 ± 0.005 nmol kg^{-1}. The major sources of particulate Fe in marine water column include lithogenic and anthropogenic aerosols, sediment resuspension and transport from continental shelf and slope, and the formation of Fe oxyhydroxides from reducing sediments or hydrothermal vents. However, quantifying the Fe source contributions in a large oceanic region is highly challenging due to sampling limitation and the complicated physical and biogeochemical cycling processes involved in the water

doi:10.6342/NTU202302200

column.

Fe isotopic composition may be a powerful parameter to distinguish the relative contribution of various Fe sources in the ocean. It has been reported that Fe from different sources possess specific isotopic features. A top-down source of atmospheric deposition, the natural aerosol dust and loess have relatively positive characteristics, with average δ^{56}Fe value to be +0.1 ± 0.1 ‰ (Beard et al., 2003; Conway et al., 2019; Mead et al., 2013; Waeles et al., 2007). In addition to lithogenic aerosols, recent studies argued that anthropogenic aerosols originating from East Asia, which possess high dissolvable Fe, may be an important Fe source in the surface water of the subarctic Pacific Ocean (Ito et al., 2021; Kurisu et al., 2016; Pinedo-Gonzalez et al., 2020; Ho et al. 2018). δ^{56}Fe of anthropogenic aerosols is significantly distinct from natural dust, fractionated by high temperature combustion processes, with the value ranging from -3.9 to -4.7 ‰ (Kurisu et al., 2019; Hsieh et al., 2023 this thesis). In the deep ocean, the δ^{56}Fe range of hydrothermal fluids is -0.69 to -0.12 ‰ (Fitzsimmons and Conway, 2023). The precipitated Fe oxyhydroxides during vent fluids transport are isotopically heavy compared to the initial isotopic ratio (Fitzsimmons and Conway, 2023). The δ^{56}Fe of reductive dissolved Fe in pore water is relatively light, ranging from -0.3 to -3.6 ‰ (Conway and John, 2014; Fitzsimmons and Conway, 2023; Fitzsimmons et al., 2016). However, the δ^{56}Fe of dissolved Fe in oxygenated sediment pore water is relatively heavy, +0.2±0.2 ‰ (Homoky et al., 2011; Radic et al., 2011).

In 2017, we had the opportunity to join the GEOTRACES GP-02 subarctic Pacific Ocean transect study (Led by Prof. Hajime Obata from the University of Tokyo). The oceanic region serves as an ideal study area to investigate the Fe sources and contribution in the of HNLC region. In this study, we collected suspended particulate material in the water column to investigate the spatial distribution of particulate Fe concentration and isotopic composition in the subarctic Pacific as part of the international GEOTRACES project. As Figure 5.1 shows, the west-east sampling stations match with the elevated AOD belt, where aerosols are transported from East Asia (Fig. 5.1). Through the spatial variation patterns of SPM, we may investigate the importance of resuspended sediments and pore water from the lateral transport of adjacent marginal seas on Fe supply. Applying elemental and isotopic ratios to examine their spatial distribution and features, we would investigate the quantitative contribution of aerosol deposition and other potential Fe sources in the oceanic region. In brief, this study shall provide valuable data to understand and evaluate Fe sources and cycling in the water column of the subarctic Pacific Ocean.

5.2 Method

5.2.1 Sampling sites and method

Suspended particulate matter (SPM) samples were collected in the subarctic Pacific Ocean (CL1 to CL21) and separated into two transects: a west-east 47°N transect and a north-south 145°W transect (GEOTRACES GP02 line; Figure 5.1) during the GEOTRACES Japan cruise KH-17-3 (R/V Hakuho Maru) between July and August 2017. Seawater samples were collected by acid-cleaned Niskin-X bottles and then transferred to a positive pressure bubble clean space filled with filtered air.

We were allowed to collect size-fractionated SPM samples without any delay of seawater sampling for other parameter, hereafter abbreviated as not-delayed samples. The sampling stations were 2, 4, 5, 7, 9, 17, 19, 21 along 47°N transect and stations 14, 15, 16 along the 145 °W transect. For some other mega stations, we collected bulk SPM with leftover seawater after other seawater sampling with high priority, hereafter abbreviated as delayed sampling samples. The sampling stations were 1, 3, 6, 8, 10, 20 from the west to the east and 13, 12, 11, and 18 from the north to the east. The size-fractionated SPM samples by using trace metal clean filtration apparatus equipped with pore size sequence 150, 60, and 10 μm mesh changeable Nitex nets, which was used to gently separate and collect different sizes of suspended article samples by gravity filtration (Ho et al., 2007; Wen et al., 2018). The size-fractionated SPM samples were filtered with 36 L seawater, then filtered approximately 5–10 L of seawater with less than 10 μm particles seawater through with 0.2 μm hydrophilic polyethersulfone membrane filter (PES, Acropak 200, Pall Industries) to obtain the size fraction ranging from 0.2 to 10 μm. Regarding the size fractions of 10–60, 60–150, and > 150 μm samples, we applied the 10-μm pore size Polycarbonate membranes (Millipore) to collect particles. The size fraction 0.2-10 mm accounted for more than 90% of bulk particulate Fe, here we reported the concentrations and δ^{56}Fe value of this fraction with more than 90% of mass. In terms of bulk SPM, we filtered approximately 5–10 L of seawater through with 0.2 μm PES membrane filter to have bulk SPM.

5.2.2 Quantification of Fe concentration and isotopic composition

doi:10.6342/NTU202302200

All the SPM samples were digested by freshly prepared mixed solution with 50% of ultra-high purity grade nitric acid (HNO_3) and 10% of hydrofluoric acid (HF), then heated overnight at 120°C (heater temperature). The digested solutions were dried up with open caps, then dissolved dried samples in 10 ml 0.5 M HNO_3 solution at 120°C (heater temperature) with closed caps for 1 h. Before further concentration quantification, we removed insoluble particles through a 13 mm pre-acid washed 0.2 μm hydrophilic PTFE syringe filter (Advantec). For cleaning storage and digestion vials, we followed the suggested procedures in the GEOTRACES Cookbook (Cutter et al., 2017). All of the laboratory procedures were carried out in a positively pressured class 5 cleanroom by wearing powder-free polyvinyl chloride (PVC) gloves while handling samples.

The details of Fe isotopic analysis has been described in Chapter 4.2.3..

5.3 Result

5.3.1 Particulate Fe concentration

Figure 5.2A and Figure 5.2B exhibit the particulate Fe (PFe) concentration distribution in the subarctic North Pacific Ocean along the 47°N and 145°W transects. Due to the PFe concentration of the time delay sampling being significantly less than cat net (Not delayed) sampling, it is thus we do not include the data in the contour figure. Along the 47°N transect, the highest concentrations of PFe were near the continental shelf or slope in the marginal sea or bottom ocean. In the east of the subarctic Pacific Ocean, the PFe plume can reach station CL17, and concentration can be up to 2.4 nM in the surface water and 2.8 nM in the intermediate water. In terms of the west of the subarctic Pacific Ocean, the feature of the particulate Fe plume is insignificant. In the surface water (10m), the concentration slightly decreases from the west to the east, and the value decreases from 1.1 to 0.59 nM. In the remote ocean region (CL4, CL5, CL7, and CL9), the most PFe concentration is less than 1000 pmol L^{-1} through the water column, and the average PFe concentration is 0.65 ± 0.28 nM.

In terms of 145°W transect, we also observed the highest PFe concentration near the continental shelf and slope in CL14, and the concentration decreased toward the south. Station CL14 has the highest PFe concentration, ranging from 6570 to 115986 pmol L-1 through the whole water column. The particulate Fe plume can also extend to the CL17 from the surface to the deep water.

doi:10.6342/NTU202302200

5.3.2 δ^{56}Fe distribution in SPM

Figure 5.2C and Figure 5.2D exhibit the δ^{56}Fe distribution of particulate Fe in the subarctic North Pacific Ocean along the 47°N and 145°W transects. Along the 47°N transect, the δ^{56}Fe of PFe in the water depth of 10 m all observed positive values, ranging from 0.04 to 0.32 ‰. Near Okhotsk Sea stations (2, 4, and 5), the deep water samples observed slightly negative values in intermediate and upper depth water (700-3500m) with a minimum value of -0.11 ‰. At the eastern side of stations 19 and 21 (near the marginal sea), the vertical profiles also followed similar patterns with CL2, and the minimum value was -0.12 ‰. In the west-to-east transect’ s central stations (CL17), we observed that δ^{56}Fe values were comparable with lithogenic values throughout the water column, ranging from 0.03 to 0.13 ‰.

In terms of the 145°W transect, the δ^{56}Fe of PFe in the water depth of 10 m also observed positive values or close to 0 ‰. The marginal sea stations CL14 and CL15 also observed the δ^{56}Fe with negative values in the intermediate or upper deep water, and then the value increased toward the south. In terms of the bottom depth of PFe for all stations, the δ^{56}Fe values were mostly greater than 0, except for CL21 and CL14.

5.4 Discussion

5.4.1 Biotic vs abiotic particles: delayed vs not-delayed filtration data

The guideline of suspended particle sampling by GEOTRACES Cookbook, Section 9.5 Filtration time and particle settling artifacts, points out a long recognized problem for the bias of suspended particle sampling due to particulate sedimentation in water sampling bottles prior to filtration (Bishop and Edmond, 1976; Gardner, 1977). The biases can be a factor of two or more. The cookbook recommends gentle mixing of sampling bottles right before filtration. The unique opportunity we had to carry out delayed and not-delayed sampling at the mega and non-mega stations of GP-02 transect actually allow us to examine the patterns of the elemental and isotopic composition between the two different sampling approaches and the possibility to separate highly suspended particles from total SPM. We found that both PFe concentration and δ^{56}Fe exhibited distinct values in the top 1,000 m between the two sampling methods (Fig. 5.4). However, particulate phosphorus (PP) exhibited an opposite pattern, with comparable composition in the top 400 m but a significantly different value in the deeper water (Fig. 5.4). To quantitatively present the difference between the two sampling approaches, we compared the PFe ratio by the averages of all of the ratios from the value of two adjacent sampling stations as the follows, CL3/CL4, CL5/CL6, CL7/CL8, and CL9/CL10. The averaged ratios in the top 100 m ranged from 9.1 (10 m) to 3.2 (100 m), then kept decreasing with depth to the bottom depth, where the ratios were close to 1. The vertical patterns of the composition indicate that up to 90% or even more of the total suspended particles were removed by using the delayed sampling approach in the upper water, particularly in the top 100 m. Related studies show that the concentrations of relatively large and dense suspended lithogenic particles decrease with depth, which may be attributed to the effect of high turbulence in the surface water. In terms of δ^{56}Fe values, similar vertical patterns are observed, with the highest difference in the surface water (0.43 ‰) then decreasing with depths. However, the averaged PP concentration ratios are comparable between the two sample methods in the surface water, with ratios varying from 0.8 to 1.2 in the top 100 m and gradually increasing with depth from 1.4 to 3.3. Since the major PP in the euphotic zone of the open ocean (Bishop, 1999) mainly originate from biotic particles, mainly phytoplankton and zooplankton, PP measured in the surface water highly likely represents the P in plankton.

To validate the contribution of the PP for plankton intracellular quota, Figure 5.5 further compared Al/P and Fe/P ratios in the surface water (<200 m) of this study and other open ocean studies. Al content in marine suspended particles have been traditionally used as a criterion to examine the influence of lithogenic material (Bruland et al., 1991; Ho et al., 2003; Martin and Knauer, 1973), witnessed by the strong linear correlation observed in the surface water of the global ocean and relatively scattered pattern for low Al/P and Fe/P ratio data (Fig. 5.5A). Our data showed that PFe samples collected by Catnet were comparable to the Fe/P and Al/P range collected in the North Atlantic Ocean, where the dust input from the Saharan desert is high. In terms of the reasonable range of P-normalized Fe quota in plankton, based on laboratory culture studies and early field studies, two papers reported 7.5±0.5 and 5.1±1.6 mmol/mol to P (Ho, 2006; Ho et al., 2003). Compiling more recent field data, Liao et al. (2017) reported that the quota ranged from 2 to 7 mmol/mol to P. We thus use 7.5 as the upper limit of the Fe in biotic particles for this study. Figure 5.4B shows that Fe/P ratios in delayed samples were significantly lower than not-delayed samples, with many ratios lower than 10 (mmol mol^{-1} P). These low Fe/P ratio within the green shaded Fe/P ratio indicate that most of

doi:10.6342/NTU202302200

Fe measured in the delayed samples originated from biotic particles. The data obtained from the not-delayed sampling represent the bulk PFe sample, mainly originated from lithogenic dust, and some of the low Fe/P delayed sampling data may represent plankton particles. Our results indicate that delayed sampling for SPM may become a useful approach to collect and separate biotic from abiotic particles in the surface water of the ocean.

5.4.2 The patterns of the spatial distribution of PFe, δ^{56}Fe, and DFe: tracing sources

Figure 5.2 shows that PFe concentrations tend to have elevated concentrations near the marginal seas or the sediments in the open ocean so that the spatial concentration gradients were horizontal or bottom up instead of top down. Overall, the concentrations in the water column were relatively low between stations CL5 and CL9. To evaluate the impact of aerosols on the elemental and isotopic composition of PFe in the surface water, we examine the composition gradient from the most western to the most eastern stations in the surface water (Fig. 5.2). While the DFe is depleted (<0.1 nM) in the top 100 m, the PFe concentrations remain relatively high in the surface water, ranging from 0.33 to 3.9 nM. The PFe to DFe ratios were 15, 8.8, 8.5, 17, 4.2, 16, 21, and 19 for stations 2, 4, 5, 7, 9, 17, 19, and 21, respectively, indicating the PFe could play critical role supplying bioavailable Fe for marine phytoplankton growth in the surface water. The spatial gradient of PFe concentrations from the western to eastern stations along with the elevated AOD zone was insignificant in the surface water (Fig. 5.5), with the averaged PFe to be 0.97±0.10, 0.73±0.35, 0.68±0.28, 0.55±0.14, and 0.54±0.0.30 nM in the top 100 m for stations 2, 4, 5, 7, and 9, respectively (Fig. 5.6), and the PFe concentrations increased from CL17 to CL 21, which were 1.1±1.1, 1.1±1.1, and 1.8±1.8 for stations 17, 19, and 21, respectively. In terms of the spatial distribution of δ^{56}Fe in the surface water, the averaged values were 0.06, 0.06, 0.14, 0.21, 0.19, 0.11, 0.09, and -0.02 ‰ for stations CL2 to CL21, which is comparable to the value in lithogenic particles. We also found that the ratios of Fe/P were significantly higher than the intracellular Fe/P quota reported, and Fe/Al ratios were relatively close to the crustal ratio, strongly indicating that the supply of lithogenic particles were high in the surface water.

In the surface water, we observed δ^{56}Fe ranged from -0.13 to -0.53 ‰, with an average δ^{56}Fe to be -0.34, -029, -0.24, -0.19, -0.24, and -0.39 for stations 1, 3, 6, 8, 10, and 20, respectively without showing significant spatial trend along the 47°N transect. These values are comparable to the result during a subtropical phytoplankton bloom (Ellwood et al., 2015).

doi:10.6342/NTU202302200

To further reduce the influence of lithogenic SPM on plankton particles, we have chosen the samples with low Fe/P and low Al/P value from the delayed samples (Fig. 5.5). We found that samples with Fe/P ratios smaller than 7.5 samples were all from the depths shallower than 50 m. Using Al SPM concentration (< 350 pM) as a threshold to exclude samples with high lithogenic SPM, the Fe/P ratios and the corresponding δ^{56}Fe values in the 8 samples with lowest Al concentrations were 2.7, 3.0, 2.0, 2.1, 2.4, 2.4, 1.6, and 1.6; and -0.28, -0.33, -0.19, -0.28, -0.13, -0.25, -0.21, and -0.27 ‰, respectively. The average value is -0.24±0.006 ‰. Assuming that -0.24 ‰ represents intracellular δ^{56}Fe value in plankton and anthropogenic and lithogenic material as the two major sources of bioavailable Fe, the estimated contribution of anthropogenic aerosol Fe (-3.9 to -4.7 ‰) would be less than 10 %. Considering the fractionation of phytoplankton uptake (-0.5 to -1‰, Fitzsimmons and Conway, 2022), the contribution of anthropogenic Fe (-3.9 to -4.7 ‰) would be further reduced. The estimated δ^{56}Fe value of DFe pool utilized by phytoplankton would be greater than 0 ‰. Thus, both An-Fe (-3.9 to -4.7 ‰) and continental shelf reductive dissolution Fe (-0.3 to -3.6‰) are unlikely to be the major source of the intracellular Fe. Instead, lithogenic material, either from lithogenic dust or sedimentary lithogenic material transported laterally, would be most likely to be the major source of biogenic SPM. Further studies with higher spatial sampling resolution from north to south around 160°E to 160°W is useful to evaluate the impacts of horizontal transport of lithogenic material from the adjacent marginal seas.

In the deep ocean, SPM Fe did not seem to match with the zone of DFe plume, located from 400 to 2000 m of the Western Subarctic Gyre (Fig. 5.2, Fig. 5.6). The distribution pattern of PFe concentrations was not similar to DMn either (Fig. 5.6). However, the distribution pattern of δ^{56}Fe in PFe is closely associated with elevated DFe zone, showing relatively lower δ^{56}Fe values (-0.12%) at the high DFe with higher external Fe region (Fig. 5.7).

In North-South transect, the concentration gradient clearly shows that the Alaska continental slope is the major source of PFe throughout the whole water column. The PFe from the slope can be transported southward in the surface and deep water down to 1,500 km (Fig. 5.2B). δ^{56}Fe values near the CL15 station were relatively low throughout the water column, where DFe concentrations were high. We suspect that the hydrothermal vent is the major source of the elevated SPM Fe.

doi:10.6342/NTU202302200

5.5 References

Beard, B.L., Johnson, C.M., Von Damm, K.L. and Poulson, R.L., 2003. Iron isotope constraints on Fe cycling and mass balance in oxygenated Earth oceans. Geology, 31(7) DOI: 10.1130/0091-7613(2003)031<0629:Iicofc>2.0.Co;2.

Bishop, J.K.B., 1999. Transmissometer measurement of POC. Deep Sea Research Part I: Oceanographic Research Papers, 46(2): 353-369 DOI: 10.1016/s0967-0637(98)00069-7.

Bishop, J.K.B. and Edmond, J.M., 1976. A new large volume filtration system for the sampling of oceanic particulate matter. J. Marine Res., 34: 181-198

Boyd, P.W. et al., 2004. The decline and fate of an iron-induced subarctic phytoplankton bloom. Nature, 428(6982): 549-53 DOI: 10.1038/nature02437.

Bruland, K.W., Donat, J.R. and Hutchins, D.A., 1991. Interactive influences of bioactive trace metals on biological production in oceanic waters. Limnology and Oceanography, 36(8): 1555-1577 DOI: 10.4319/lo.1991.36.8.1555.

Conway, T.M. et al., 2019. Tracing and constraining anthropogenic aerosol iron fluxes to the North Atlantic Ocean using iron isotopes. Nat Commun, 10(1): 2628 DOI: 10.1038/s41467-019-10457-w.

Conway, T.M. and John, S.G., 2014. Quantification of dissolved iron sources to the North Atlantic Ocean. Nature, 511(7508): 212-5 DOI: 10.1038/nature13482.

Cutter, G. et al., 2017. Sampling and Sample-handling Protocols for GEOTRACES Cruises. 3 DOI: 10.25607/OBP-2.

Ellwood, M.J. et al., 2015. Iron stable isotopes track pelagic iron cycling during a subtropical phytoplankton bloom. Proc Natl Acad Sci U S A, 112(1): E15-20 DOI: 10.1073/pnas.1421576112.

Fitzsimmons, J.N. and Conway, T.M., 2023. Novel Insights into Marine Iron Biogeochemistry from Iron Isotopes. Ann Rev Mar Sci, 15: 383-406 DOI: 10.1146/annurev-marine-032822-103431.

Fitzsimmons, J.N. et al., 2016. Dissolved iron and iron isotopes in the southeastern Pacific Ocean. Global Biogeochemical Cycles, 30(10): 1372-1395 DOI: 10.1002/2015gb005357.

Gardner, W.D., 1977. Incomplete extraction of rapidly settling particles from water samplers1. Limnology and Oceanography, 22(4): 764-768 DOI: 10.4319/lo.1977.22.4.0764.

Ho, T.-Y., Wen, L.-S., You, C.-F. and Lee, D.-C., 2007. The trace metal composition of size-fractionated plankton in the South China Sea: Biotic versus abiotic sources. Limnology and Oceanography, 52(5): 1776-1788 DOI: 10.4319/lo.2007.52.5.1776.

Ho, T.Y., 2006. The trace metal composition of marine microalgae in cultures and natural assemblages. 271-299

doi:10.6342/NTU202302200

Ho, T.Y. et al., 2003. The elemental composition of some marine phytoplankton. Journal of Phycology, 39(6): 1145-1159 DOI: DOI 10.1111/j.0022-3646.2003.03-090.x.

Homoky, W.B. et al., 2011. Iron and manganese diagenesis in deep sea volcanogenic sediments and the origins of pore water colloids. Geochimica et Cosmochimica Acta, 75(17): 5032-5048 DOI: 10.1016/j.gca.2011.06.019.

Ito, A., Ye, Y., Baldo, C. and Shi, Z., 2021. Ocean fertilization by pyrogenic aerosol iron. npj Climate and Atmospheric Science, 4(1) DOI: 10.1038/s41612-021-00185-8.

Kurisu, M., Adachi, K., Sakata, K. and Takahashi, Y., 2019. Stable Isotope Ratios of Combustion Iron Produced by Evaporation in a Steel Plant. ACS Earth and Space Chemistry, 3(4): 588-598 DOI: 10.1021/acsearthspacechem.8b00171.

Kurisu, M., Takahashi, Y., Iizuka, T. and Uematsu, M., 2016. Very low isotope ratio of iron in fine aerosols related to its contribution to the surface ocean. Journal of Geophysical Research: Atmospheres, 121(18): 11,119-11,136 DOI: 10.1002/2016jd024957.

Lam, P.J. and Bishop, J.K.B., 2008. The continental margin is a key source of iron to the HNLC North Pacific Ocean. Geophysical Research Letters, 35(7): n/a-n/a DOI: 10.1029/2008gl033294.

Liao, W.-H., Yang, S.-C. and Ho, T.-Y., 2017. Trace metal composition of size-fractionated plankton in the Western Philippine Sea: The impact of anthropogenic aerosol deposition. Limnology and Oceanography, 62(5): 2243-2259 DOI: 10.1002/lno.10564.

Martin, J.H. et al., 1994. Testing the iron hypothesis in ecosystems of the equatorial Pacific Ocean. Nature, 371(6493): 123-129 DOI: 10.1038/371123a0.

Martin, J.H. and Fitzwater, S.E., 1988. Iron deficiency limits phytoplankton growth in the north-east Pacific subarctic. Nature, 331(6154): 341-343 DOI: 10.1038/331341a0.

Martin, J.H. and Knauer, G.A., 1973. The elemental composition of plankton. Geochimica et Cosmochimica Acta, 37(7): 1639-1653 DOI: 10.1016/0016-7037(73)90154-3.

Mead, C., Herckes, P., Majestic, B.J. and Anbar, A.D., 2013. Source apportionment of aerosol iron in the marine environment using iron isotope analysis. Geophysical Research Letters, 40(21): 5722-5727 DOI: 10.1002/2013gl057713.

Moore, C.M. et al., 2013. Processes and patterns of oceanic nutrient limitation. Nature Geoscience, 6(9): 701-710 DOI: 10.1038/ngeo1765.

Nishioka, J. et al., 2020. Subpolar marginal seas fuel the North Pacific through the intermediate water at the termination of the global ocean circulation. Proc Natl Acad Sci U S A, 117(23): 12665-12673 DOI: 10.1073/pnas.2000658117.

Nishioka, J. et al., 2007. Iron supply to the western subarctic Pacific: Importance of iron export from the Sea of Okhotsk. Journal of Geophysical Research, 112(C10) DOI: 10.1029/2006jc004055.

Pinedo-Gonzalez, P. et al., 2020. Anthropogenic Asian aerosols provide Fe to the North

Pacific Ocean. Proc Natl Acad Sci U S A, 117(45): 27862-27868 DOI: 10.1073/pnas.2010315117.

Radic, A., Lacan, F. and Murray, J.W., 2011. Iron isotopes in the seawater of the equatorial Pacific Ocean: New constraints for the oceanic iron cycle. Earth and Planetary Science Letters, 306(1-2): 1-10 DOI: 10.1016/j.epsl.2011.03.015.

Tsuda, A. et al., 2003. A mesoscale iron enrichment in the western subarctic Pacific induces a large centric diatom bloom. Science, 300(5621): 958-61 DOI: 10.1126/science.1082000.

Waeles, M., Baker, A.R., Jickells, T. and Hoogewerff, J., 2007. Global dust teleconnections: aerosol iron solubility and stable isotope composition. Environmental Chemistry, 4(4) DOI: 10.1071/en07013.

Wen, L.S., Lee, C.P., Lee, W.H. and Chuang, A., 2018. An Ultra-clean Multilayer Apparatus for Collecting Size Fractionated Marine Plankton and Suspended Particles. J Vis Exp(134) DOI: 10.3791/56811.

Wong, K.H., Nishioka, J., Kim, T. and Obata, H., 2022. Long-Range Lateral Transport of Dissolved Manganese and Iron in the Subarctic Pacific. Journal of Geophysical Research: Oceans, 127(2) DOI: 10.1029/2021jc017652.

Zheng, L. and Sohrin, Y., 2019. Major lithogenic contributions to the distribution and budget of iron in the North Pacific Ocean. Sci Rep, 9(1): 11652 DOI: 10.1038/s41598-019-48035-1.

doi:10.6342/NTU202302200

5.6 Figures

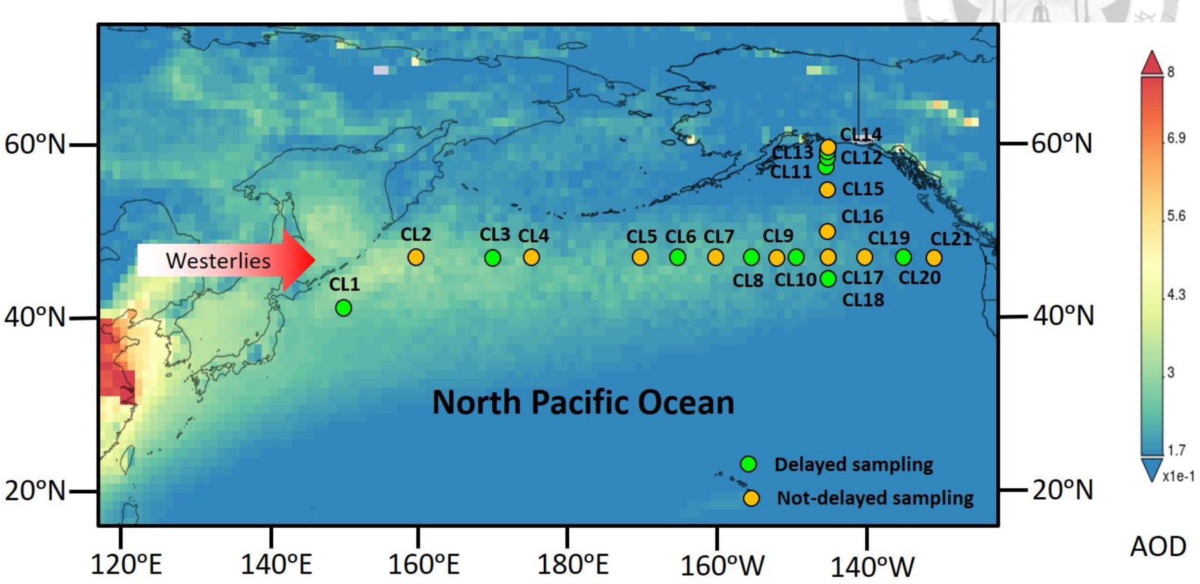

Figure 5.1. The particulate Fe concentration distribution in the 47°N transect along the Subarctic North Pacific Ocean and the annual averaged aerosol optical depths from 2002 to 2022 (background color). The aerosol optical depth data was obtained by NASA Giovanni software (https://giovanni.gsfc.nasa.gov/giovanni/).

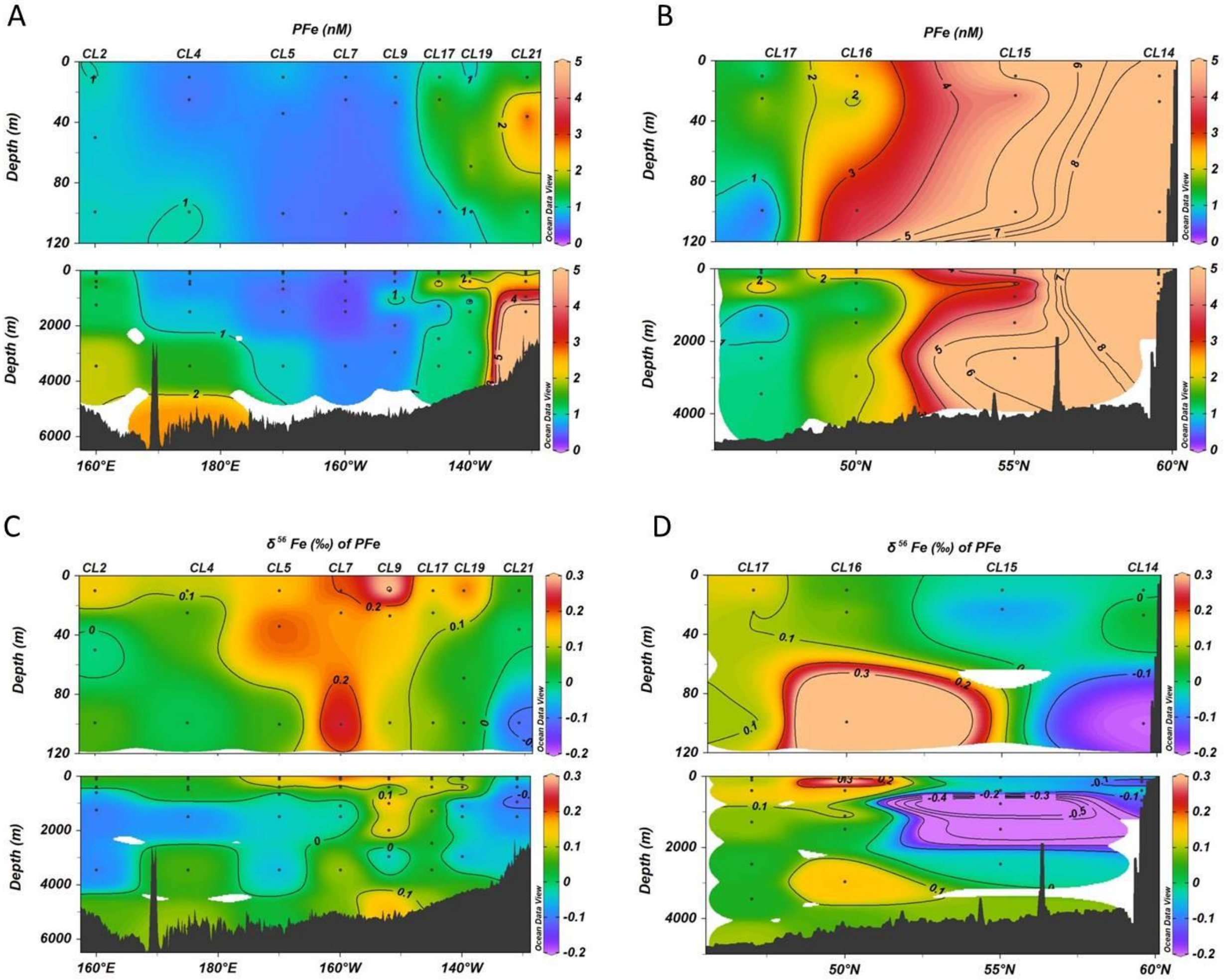

Figure 5.2. The particulate Fe concentration and δ^{56}Fe distribution along the 47°N and 145°W transects in the Subarctic North Pacific Ocean.

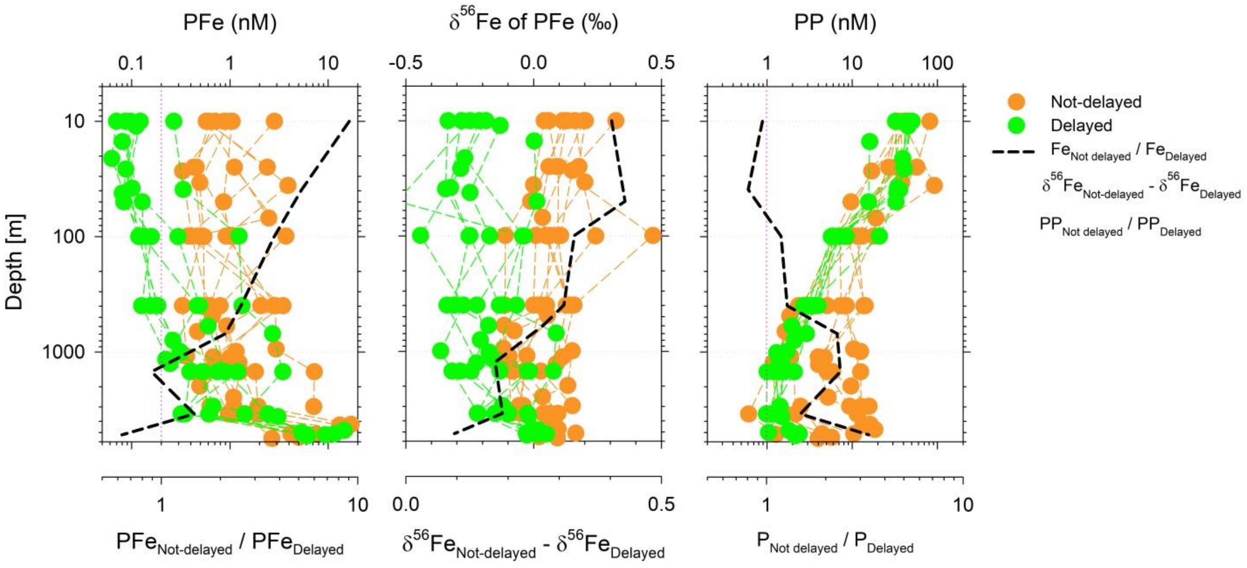

Figure 5.3. The elemental and isotopic composition of particulate Fe (PFe) and phosphorus (PP) in the water column of all sampling stations. The not-delayed and delayed sampling stations are shown as orange and green symbols, respectively. The black dashed lines stand for the ratios of the data from adjacent stations.

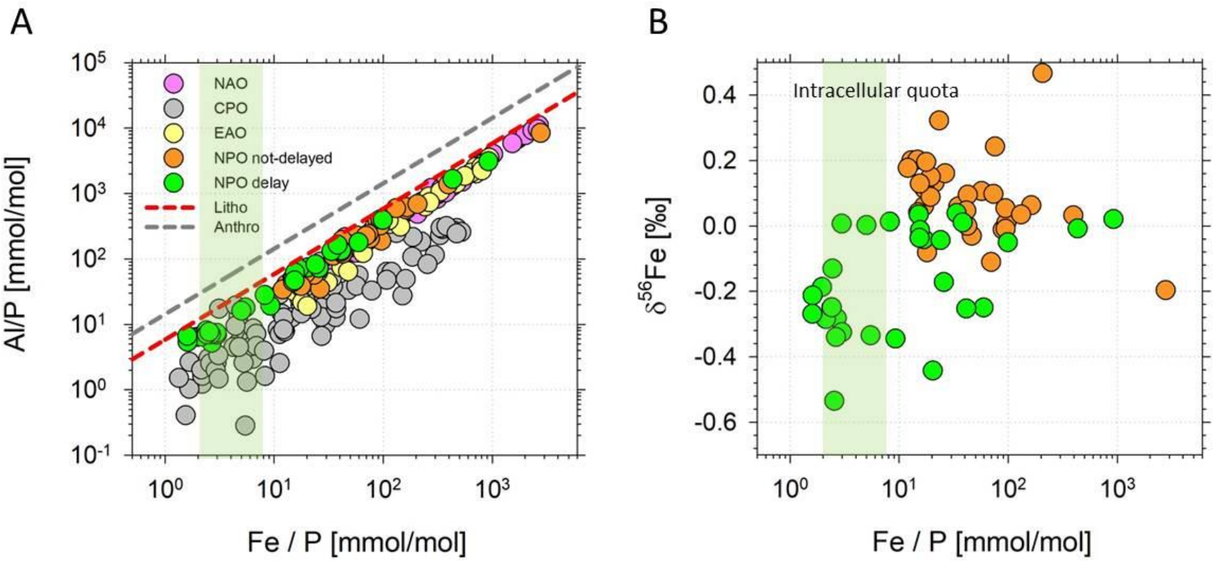

Figure 5.4. Comparision of Al/P, Fe/P, and δ^{56}Fe. The purple, gray, yellow, orange, and green circles stand for samples collected in the North Atlantic Ocean, Central Pacific Ocean, and East Atlantic Ocean, not-delayed (this study), and delayed (this study), respectively. The red and gray dashed line stand for the ratio of lithogenic and anthropogenic aerosols.

doi:10.6342/NTU202302200

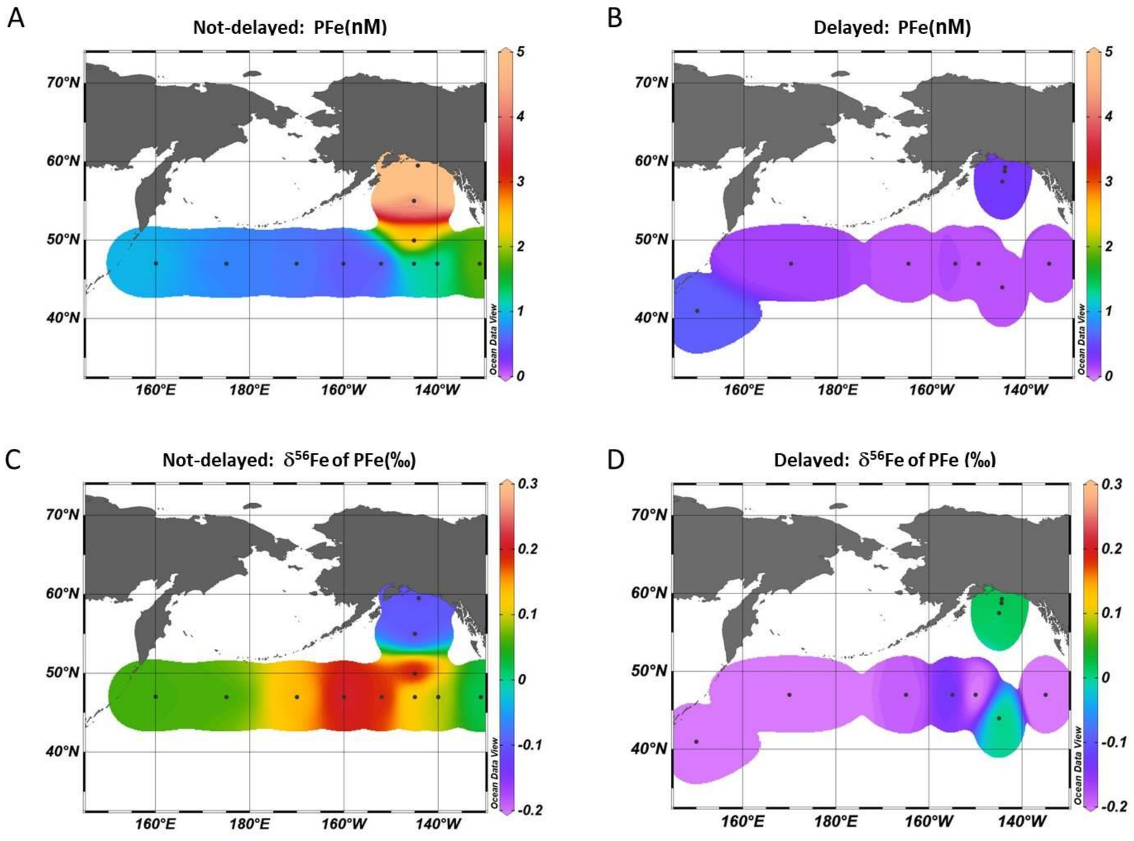

Figure 5.5. The average particulate Fe concentration and δ^{56}Fe distribution in the surface water (<100m) of the Subarctic North Pacific Ocean.

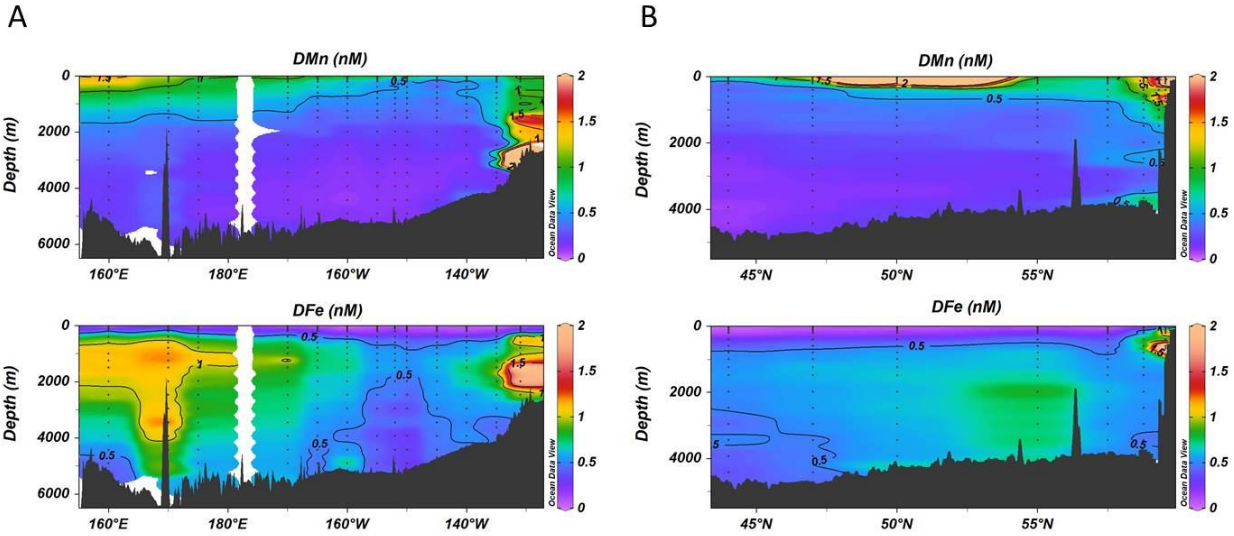

Fig. 5.6. The dissolved Fe (DF) and Mn (DM) concentration along the 47°N and 145°W transects in the Subarctic North Pacific Ocean.

doi:10.6342/NTU202302200

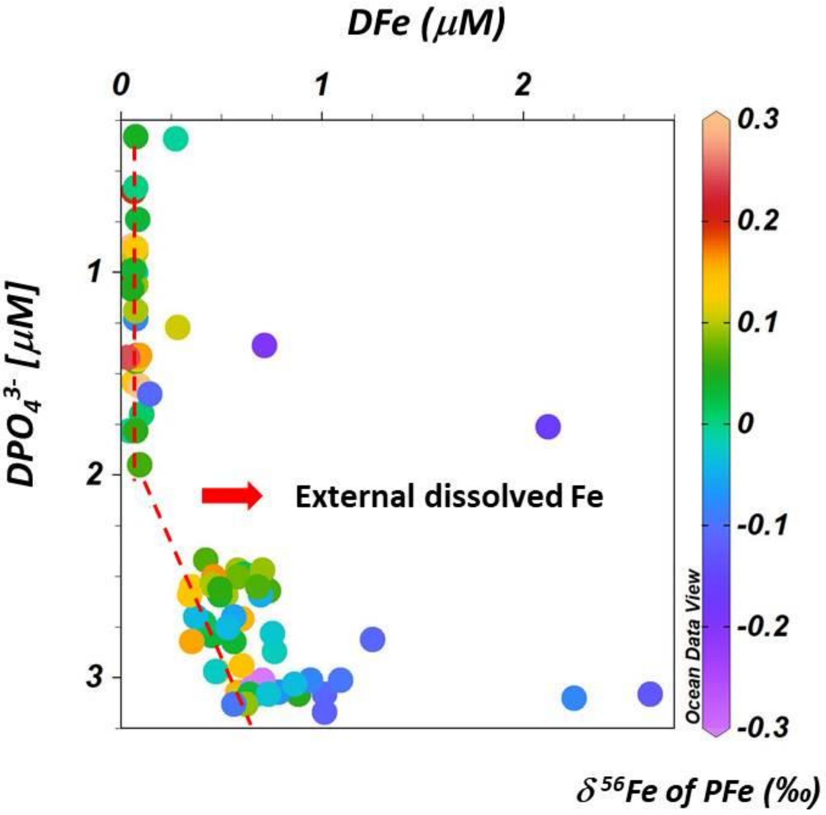

Fig. 5.7. The δ^{56}Fe in PFe compared with the depth of dissolved phosphate (DPO_4^{3-}) and dissolved Fe (DFe).

doi:10.6342/NTU202302200

Chapter 6

Conclusion

By
Chih-Chiang Hsieh[a,b]

[a] Institute of Oceanography, National Taiwan University, Taipei, Taiwan
[b] Research Center for Environmental Changes, Academia Sinica, Taipei, Taiwan

doi:10.6342/NTU202302200

6.0 Conclusion

This study shows that solubilities obtained by different leaching treatments are highly varied for lithogenic type metals in coarse aerosols. The averaged deposition velocities of aerosols among different leaching protocols thus varied significantly among different elements, ranging from a few folds to one order of magnitude, which are 0.04-0.43, 0.08-0.49, 0.20-0.63, and 0.19-0.80 cm s^{-1} for ultrapure water, buffer, Berger, and total leaching treatments, respectively. While only applying total fraction deposition velocity, aerosol metal fluxes calculated would be largely overestimated, especially for lithogenic type elements (e.g., Al, Fe, Ti). In terms of the impacts of transport processes on the solubility, we found that the impacts of transport processes on aerosol metal solubility and deposition velocities are element-specific, with elevated enhancement for lithogenic type elements. Two-size aerosol sampling provides a much more reliable flux estimate for aerosol metal deposition than total suspended particle sampling. We may use two-size deposition velocities to obtain more accurate estimates for aerosol metal fluxes without knowing the metal mass fraction in size-fractionated aerosols. In terms of solubility applied to global model flux estimates, we think that ultrapure water leach underestimates the aerosol solubility of V, Al, Fe, and Ti in the surface water of the ECS. The buffer and Berger leaches are more realistic to represent the metal solubility of the lithogenic type elements in the ocean.

In terms of Fe isotopic composition in aerosols collected in the ECS, the lowest δ^{56}Fe value of bulk, dissolved, and labile Fe we observed were -3.35, -4.46, and -4.34, respectively, indicating that the δ^{56}Fe endmember of anthropogenic Fe (high temperature combustion) may be as low as -4.46 ‰. According to the δ^{56}Fe correlated with most of the metal to Ti ratios, the aerosols collected in the ECS were mainly mixed by lithogenic and anthropogenic Fe, and anthropogenic Fe is mainly from high temperature combustion aerosols. The lithogenic and anthropogenic aerosol mixing decided the δ^{56}Fe variations of aerosol Fe. Although anthropogenic aerosol Fe contributes more than 50% of dissolved Fe concentration during NE monsoon seasons, the lithogenic aerosol Fe is the dominant Fe source for bulk, dissolved, or labile Fe fluxes into the ECS which has high anthropogenic aerosol input region. The δ^{56}Fe features of biotic particulate Fe (-0.24±0.06 ‰) or bulk particulate Fe (+0.12±0.08 ‰) data in the top 50 m water also supported that anthropogenic aerosol Fe is not the major Fe source in the Northwestern Pacific Ocean.

For the practice of global aerosol models for Fe flux estimate in the ocean, we suggest

doi:10.6342/NTU202302200

that Fe solubility chosen in the models should exclude dissolved Fe data obtained from ultrapure water leach and Fe solubilities obtained from Buffer or Berger leaches should be applied. The Fe solubilities of buffer and Berger leaches in size-fractionated aerosols should be determined in other major oceanic regions so that the deposition velocities calculated from size-fractionated data would be accurate and representative to estimate the fluxes of dissolvable Fe fluxes in the global ocean.

doi:10.6342/NTU202302200